

---

# Development of Hydrogen Sensors Based on Polymeric and Ceramic Proton Conductors

**Dissertation**

zur Erlangung des akademischen Grades  
Doktor der Ingenieurwissenschaften  
(Dr.-Ing.)  
der Technischen Fakultät  
der Christian-Albrechts-Universität zu Kiel

**Mariappan Sakthivel**



Kiel  
2006

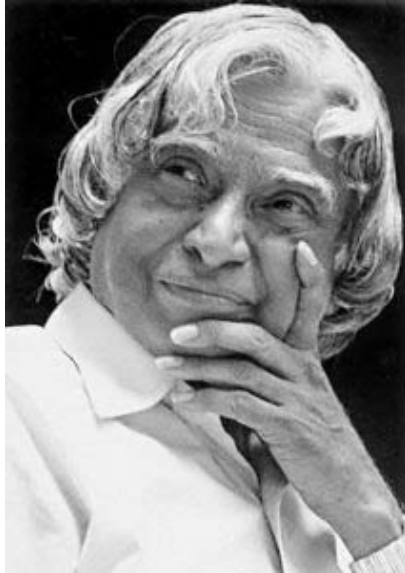
---

---

1. Gutachter: Prof. Dr. W. Weppner  
2. Gutachter PD. Dr. G. Popkirov  
Datum der mündlichen Prüfung 15 December 2006

---

Dedicated to



**Dr. A.P.J. ABDUL KALAM**  
President of India

*“To succeed in your mission, you must have single-minded devotion to your goal”*

*“Great dreams of great dreamers are always transcended”*



---

## Acknowledgements

I am deeply indebted to my professor Dr. Werner Weppner for all of his guidance, continued enthusiasm, patience as my research evolved considerably. I am highly impressed by his knowledge and approach to solve problems. In spite of his busy schedule, he made himself always available whenever I barged into his office. I really enjoyed with him in the lab for long hours of experiments. I appreciated his confidence in me and in the way I managed this work as well as the possibility he gave me to present my results at international conferences all over the world. I have found working with Professor Weppner tremendously rewarding and truly feel like I have learned from the best!

I would also like to express my sincere gratitude to emeritus professor Dr. Robert A. Huggins for his advice and encouragement throughout my research as well as to complete my thesis. Also I would like to thank him for showing special interest on my family life.

I also wish to thank Dr. Venkataraman Thangadurai for immense pleasure working with him and I have benefited greatly from his advice. I appreciate his approaches on far advance experimental planning. His stimulating discussions, words of encouragement, gave me a driving force to complete this work.

I wish to thank Dr. Wing Fong Chu for ordering materials for quick delivery, sharing his valuable experience on experimental aspects and helping to understand script conventions during the preparation of journal manuscripts.

I would like to thank Dr. Rainer Adelung and Mr. Sebastian Wille for their excellent support in operating the AFM measurements. I am also thankful to Dr. Vladimir Zaporotchenko and Mr. C.V. Kiran for their assistance with XPS investigation.

I am grateful for the assistance, and advice I received from Dr. Christian Dietz for chemical handling and particle size analysis. I also express my gratitude to Dr. R. Murugan for his advice and assistance made it possible for me to complete the thermal and vibrational studies for this work.

I specially thank Ms. Gislinde Schroeder for her secretarial assistance and support in German translation for bureaucratic formalities. I also thank her for untiring listen to my family problems and for her continuous moral support.

I would like to thank Mr. Thomas Metzging for his expertise in solving many of the technical problems during experiments.

I extend many thanks to the library, computer administration, and workshop teams for being always helpful.

I would also like to acknowledge the help and support that I received from the present and former members of the sensors and solid state ionics group, especially my colleagues, Dr. Julian Schwenzel, Dr. Evangelos Tsagarakis, Mr. Gregor Holstermann, Mr. Qingping Fang, Mr. Tesfaye Shiferaw, Mr. Christian Knittlmayer, Mr. Yongming Zhu, and Miss. Janine Dahmke for creating a friendly environment with more pleasant and fun during my Ph.D work.

I would also like to thank my beloved friends in India, Germany and all around the world. They were always supporting me and encouraging me with their best wishes. My special thanks to Mr. N. Ravishankar as a good friend, was always willing to help and give his best suggestions. It would have been a lonely life in Kiel without him. Also I would like to thank Miss. J. Deepa for her patience while reading my thesis.

My highest appreciation is addressed to my family and to my sister Miss. M. Mekala who constantly listened carefully to all of my problems, who shared my sorrow, and who motivated me everyday through e-mail.

Finally, I would like to thank my wife Ms. S. Priya for all her constant support, and patience during the last stages of the Ph.D and reading my thesis. She was always there cheering me up and stood by me through the good times and bad.

---

# Contents

<b>1. Introduction</b>	
1.1 Hydrogen economy and safety.....	1
1.2 Application areas of hydrogen sensors.....	3
1.3 Types of hydrogen sensors .....	5
1.4 Motivation .....	7
1.5 Structure of the thesis .....	9
<b>2. Principles and characteristics of electrochemical sensors</b>	
2.1 Electrochemical solid-state hydrogen sensor .....	11
2.2 General mechanism of electrochemical gas reactions .....	12
2.2.1 Theory of the limiting current: steady-state current .....	13
2.2.2 Short circuit amperometric method .....	14
2.3 Characteristics of amperometric sensors .....	15
2.4 State of the art on amperometric H <sub>2</sub> sensor .....	17
2.4.1 Other methods .....	18
<b>3. Theoretical and Fundamental aspects on materials and methods</b>	
3.1 Gas diffusion layer .....	23
3.1.1 Advantage of using gas diffusion layer .....	23
3.2 Choice of electrode materials .....	24
3.2.1 Electrode preparation methods .....	25
3.2.2 Paste/ Slurry route .....	26
3.2.3 Electroless wet route .....	27
3.3 Role of Catalyst / Gas solid interaction .....	27
3.3.1 Physisorption and chemisorption .....	28
3.3.2 The Platinum-Hydrogen system .....	28
3.3.2.1 Langmuirian model in an inert atmosphere .....	29
3.3.2.2 Langmuirian model in the presence of air .....	30
3.4 Choice of electrolyte materials .....	31
3.4.1 Solid Polymer electrolyte membrane (PEM) .....	31
3.4.2 Solid oxide perovskite type electrolyte .....	35
3.4.2.1 Ideal perovskite .....	35
3.4.2.2 Layered perovskite .....	35
3.4.2.3 Dion-Jacobson phase .....	37
3.4.3 Ionexchangeability of layered perovskites .....	37
3.5 Kinetic consideration on electrode/electrolyte interfaces .....	39
3.5.1 Metal-Polymer interface .....	39

---

<b>4. Experimental aspects</b>	
4.1 Electrode preparations	47
4.1.1 Thick layer electrode	47
4.1.1.1 Catalyst synthesis using formaldehyde as reducing agent	47
4.1.1.2 Catalyst synthesis using hydrazine as reducing agent	47
4.1.1.3 Catalyst synthesis using alkali borohydrides as reducing agent	48
4.1.2 Slurry paste brush method	48
4.1.2.1 Synthesized catalyst electrode	48
4.1.2.2 Commercial catalyst electrode	49
4.2 Preparation of the membrane electrode assembly (MEA)	49
4.2.1 Preparation of MEA using Nafion film	49
4.2.2 Preparation of MEA using Nafion solution	51
4.3 Thin layer electrode	52
4.3.1 Sputter deposition	52
4.3.2 Electroless deposition	53
4.3.2.1 Electrode deposition by T-T method	54
4.3.2.2 Electrode deposition by I-R method	55
4.3.2.3 Electrode deposition by M-I-R method	55
4.4. Electrolyte preparations	56
4.4.1 Polymer Electrolyte	56
4.4.1.1 Solid polymer membrane (SPE) pre-treatment	56
4.4.2 Ceramic Electrolyte	57
4.4.2.1 Solid state sintering	57
4.4.3 Protonation of layered perovskites	58
4.4.4 Ion exchange reaction (IER)	59
4.4.4.1 IER of niobate	59
4.4.4.2 IER of tantalate	59
4.4.5 Preparation of solid electrolyte circular pellet discs	60
4.5 Gas sensor measurement setups	60
4.5.1 Gas detection test-bench setup	60
4.5.2 Design of sensing device	61
4.5.3 Gas Measurement in air and inert atmospheres	63
4.6 Characterization of materials	64
4.6.1 X-Ray Diffractometer (XRD)	64
4.6.2 X-ray Photoelectron Spectroscopy (XPS)	65
4.6.3 Fourier Transform Infrared (FTIR) spectrometer	65
4.6.4 Thermo Gravimetric Analysis (TGA)	65
4.6.5 Optical microscope	66
4.6.6 Scanning Electron microscope (SEM) and EDAX	66
4.6.7 Atomic force microscope (AFM)	67
4.6.8 AC Impedance analyser	68
4.6.9 Cyclic Voltammetry (CV)	69



## 5. Results

5.1 Polymer based hydrogen sensors.....	71
5.1.1 Structure and morphology characterization of Pt electrodes .....	71
5.1.1.1 Reducing agent: NaBH <sub>4</sub> .....	71
5.1.1.2 Reducing agent: KBH <sub>4</sub> .....	74
5.1.1.3 Comparison of: NaBH <sub>4</sub> and KBH <sub>4</sub> .....	74
5.1.2 XPS spectral studies of Pt Nafion .....	76
5.1.3 Optical micrographs of chemically reduced electrodes .....	76
5.1.3.1 Reducing agent: hydrazine .....	77
5.1.3.2 Reducing agents: NaBH <sub>4</sub> and KBH <sub>4</sub> .....	77
5.1.4 SEM of chemically reduced electrodes .....	81
5.1.4.1 Reducing agent: NaBH <sub>4</sub> .....	81
5.1.4.2 Reducing agent: KBH <sub>4</sub> .....	81
5.1.4.3 The effect of deposition temperature .....	83
5.1.5 The elemental analysis of chemically reduced electrode byEDX	84
5.1.6 Atomic force micrograph of chemically reduced electrodes .....	85
5.1.7 Electrical conductivity of Pt Nafion MEA's .....	85
5.1.8 Estimation of electroactive surface area .....	88
5.1.9 Sensing characteristics of solid polymer based systems .....	88
5.1.9.1 Response based on the type of electrode materials .....	88
5.1.9.2 Response in dependence of the electrode deposition method: Sputtered electrode .....	90
5.1.9.3 Response in dependence of the electrode deposition: Gas diffusion electrode (GDE) .....	90
5.1.9.4 Response in dependence of the electrode deposition method: Chemically reduced electrode .....	92
5.1.9.5 Response based on current collector: Gas diffusion layer (GDL) .....	92
5.1.9.6 Response in dependence of the current collector: Carbon woven fibre: High H <sub>2</sub> gas concentration response (NaBH <sub>4</sub> ) .....	98
5.1.9.7 Response in dependence of the current collector: Carbon woven fibre: Low H <sub>2</sub> gas concentration response (KBH <sub>4</sub> )	98
5.2 Ceramic based hydrogen sensors: Niobates .....	105
5.2.1 XRD structure characterization of niobates .....	105
5.2.2 SEM observation on niobates .....	108
5.2.3 AFM studies on niobate .....	109
5.2.4 TGA of anhydrous niobate .....	109
5.2.5 FTIR spectra of niobates .....	111
5.2.6 Electrical conductivity of niobates .....	111
5.2.7 Sensing characteristic of solid oxide ceramic/perovskite based system (niobates) .....	111
5.3 Ceramic based hydrogen sensors: Tantalates .....	114
5.3.1 XRD structure characterization of tantalates .....	114

---

5.3.2 SEM observation on tantalates .....	118
5.3.3 AFM studies on tantalate .....	118
5.3.4 TGA of anhydrous tantalates .....	118
5.3.5 FTIR spectra of tantalates .....	119
5.3.6 Electrical conductivity of tantalates .....	119
5.3.7 Sensing characteristic of solid oxide ceramic/perovskite based system (tantalates) .....	122
<b>6. Discussion</b>	
6.1 Discussion on polymer based hydrogen sensors .....	125
6.2 Discussion on ceramic based hydrogen sensors: Niobates .....	133
6.3 Discussion on ceramic based hydrogen sensors: Tantalates .....	135
<b>7. Practical application: Measurement of Hydrogen in Biomass fuel generator</b>	
6.1 Bio mass fuel production .....	139
6.2 Sensing Element (SE) .....	139
6.3 Approach 1: Diffusion hole amperometric type .....	139
6.4 Approach 2: Diffusion control by Pd sheet .....	142
6.5 Approach 3: Entrapment of cross sensitive gas .....	145
<b>8. Summary and outlook</b> .....	149
<b>Partial publications</b> .....	153

---

# List of Symbols

$a_A$	Activity of species A
A	Area
$A_r$	Temperature constant
c	Gas concentration
$c_1$	Rate constant of the reaction
$c_{e^-}$	Concentration of electrons
$c_{H^+}$	Concentration of protons
$c_i$	Interface rate constant, concentration of species i
$c_s$	Bulk rate constant
$C_{H^+}$	Bulk proton concentrations
$C_l$	Capacitance at left
$C_r$	Capacitance at right
$C_{H^+}^s$	Surface proton concentrations
d	Crystallite diameter
$d_1$	Rate constant of the reaction
$d_i$	Interface rate constant
$d_s$	Bulk rate constant
D	diffusivity
$D_{H_2}$	Diffusion coefficient of hydrogen
$D_i$	Diffusivity of species i
$D_{H^+}$	Diffusion coefficient of proton
$D_{H^+}^E$	en masse diffusion coefficient
$D_{H^+}^W$	Diffusion coefficient of hydronium ion
$D_{H^+}^M$	Diffusion coefficient of polymer matrix M
$D_{H^+}^G$	Grotthuss diffusion coefficient
$\Delta E_a$	Heat of adsorption
F	Faraday's constant
$\Delta G$	Gibbs energy of formation
$h^\bullet$	Holes
$H_a$	Atomic adsorption
$H_b$	Atomic hydrogen in bulk
$H_i$	Atomic hydrogen at the interface
$H_i^\bullet$	Interstitial proton

$H_K^\bullet$	Proton at a vacant K
$\Delta H^\circ$	Change in enthalpy
$i$	Electrical current
$j_E$	Electrical field flux density
$j_{H_2}$	Flux density of hydrogen
$i_{lim}$	Limiting current
$i_0$	Exchange current density
$K$	Standard rate constant, Scherrer's constant
$L$	Diffusional channel length, Debey's length
$M_0$	Molecular weight
$n$	Number of electrons
$N_A$	Avogadro's number
$N_i$	Number of adsorption sites of species $i$
$N_s$	Number of adsorption sites on surface
$OH_O^\bullet$	Protonic defects
$O_o^x$	Lattice oxygen
$P_{H_2}$	Partial pressure of hydrogen
$P_{O_2}$	Partial pressure of oxygen
$q$	Elementary charge
$r$	Partial molar volume
$R$	Gas constant
$R_b$	Bulk charge transfer
$R_{ct}$	Interface charge transfer
$\Delta S^\circ$	Change in entropy
$t$	Time
$T$	Absolute temperature
$V_o^{**}$	Oxide ion vacancies
$V$	Linear velocity of gas flow
$W$	Warburg diffusion
$x$	Distance coordinate
$x_w$	Water mole fraction
$z_i$	Charge number of species $i$
$\alpha$	Transfer coefficient
$\beta$	Charge transfer coefficient, Integral breadth of the X-ray peak
$\beta_1$	Actual line broadening
$\delta_c$	Total conductivity

$\varepsilon_i$	Rate constant
$\eta$	Overvoltage of the electrode reaction
$\eta_{e^-}$	Electrochemical potential of electrons
$\eta_{H^+}$	Electrochemical potential of protons
$\varphi$	Electrostatic potential
$\lambda$	X-ray wavelength
$\lambda_i$	Water sorbtion
$\mu_{e^-}$	Chemical potential of electrons
$\mu_{H^+}$	Chemical potential of protons
$\sigma$	Electrical conductivity
$\sigma_{H^+}^S$	Surface proton conductivity
$\sigma_{H^+}^G$	Grotthuss proton conductivity
$\sigma_{H^+}^E$	en masse proton conductivity
$\sigma_{H^+}^\alpha$	Nernst-Einstein proton conductivity
$\sigma_p$	Total proton conductivity
$\tau$	Tortuosity factor, Response time
$\Phi_0$	Flux of gas molecules
$\Theta_i$	Interface coverage
$\Theta_s$	Surface coverage



---

## Abbreviations

AC	Alternating current
AFM	Atomic force microscope
CVD	Chemical vapour deposition
D-J	Dion-Jacobson
ECSA	Electroactive surface area
EDX	Energy-dispersive X-ray microanalysis
FET	Field effect transistor
FTIR	Fourier transform infrared spectroscopy
FWHM	Full width at half maximum
GC	Gas chromatography
GDE	Gas diffusion electrode
GDL	Gas diffusion layer
GIXRD	Grazing incidence X-ray diffraction
HOR	Hydrogen oxidation reaction
HTHA	High temperature hydrogen attack
IC	Internal combustion
IEC	Ion exchange capacity
I-R	Impregnation-reduction
JCPDS	Joint committee on powder diffraction standards
LEL	Lower explosive limit
MEA	Membrane electrode assembly
M-I-R	Multistep-impregnation-reduction
MOS	Metal oxide semiconductor
PEM	Polymer electrolyte membrane/ Proton exchangeable membrane
ppm	Parts per millions
PPy	Polypyrrole
PTFE	Polytetrafluoroethylene
PVA	Poly vinyl alcohol
QCM	Quartz microbalance
RH	Relative humidity
R-P	Ruddlesden-Popper
SAW	Surface acoustic wave
SE	Sensing element

SEM	Scanning electron microscope
SPE	Solid polymer electrolyte
TGA	Thermo gravimetric analysis
TPB	Triple phase boundary
T-T	Takenata-Torikai
XPS	X-ray photoelectron spectroscopy



---

# Chapter 1

## Introduction

### *1.1 Hydrogen economy and safety*

Global energy consumption is expected to increase dramatically in the next decades, driven by rising standards of living and a growing population worldwide. The hydrogen economy offers a compelling vision of an energy future for the world that is at once abundant, clean, flexible, and secure. We can envision the hydrogen economy as a linked network of chemical processes that *produces* hydrogen through fossil fuel reforming, biomass conversion, and electrolytic, biophotolytic, or thermochemical splitting of water; *stores* hydrogen chemically or physically; and *converts* the stored hydrogen to electrical energy and heat at the point of use. This vision of an energy stream, originating in the sun, flowing through hydrogen as a carrier to perform electrical work, and producing water as its only by-product, effectively addresses the major energy challenges of the 21<sup>st</sup> century. The biological world began developing its own hydrogen economy three billion years ago, using hydrogen, carbon, and oxygen to establish the cycle of photosynthesis and respiration that defines life on earth. The human-engineered hydrogen economy can take similar advantage of hydrogen and its chemical and physical interactions with materials to flexibly link a variety of energy sources to a multitude of energy uses.

Unlike oil, gas and coal, hydrogen does not exist in large quantities in nature in an immediately useful form [1]. However, hydrogen is estimated to make up more than 90% of all the atoms or three quarters of the mass of the universe [2]. This element is found in the stars, and plays an important part in powering the universe through both the proton-proton reaction and carbon-nitrogen cycle [3]. For example, hydrogen is a primary component of Jupiter and many other giant gas planets. At some depth in the planet's interior, the pressure is so high that solid molecular hydrogen is converted to solid metallic hydrogen. On earth, in 1973, a group of Russian experimenters have produced metallic hydrogen at a pressure of 2.8 Mbar. Some predictions are that metallic hydrogen is metastable [4] others have predicted it would be a superconductor at room temperature [5].

Hydrogen can be produced from a number of different chemical compounds containing hydrogen. At present, nearly 90% of the hydrogen produced in the world is derived from natural gas via a steam reforming process. This breakdown of the natural gas is accomplished by exposing the natural gas steam to Ni catalyst at high temperature of 700–1100 °C at a pressure of 3–25 bar [6]. The second phase of steam

reforming consists of generating additional H<sub>2</sub> and CO<sub>2</sub> by utilizing the CO created in the first phase. The simplest and cleanest way to produce hydrogen is by electrolysis of water. The actual electrolytic step of splitting water molecules with electricity is very efficient (80 to 90 %). However, when electricity generation is accounted for, the overall thermal efficiency drops to 25 to 45 %. Electrolysis currently produces 4 % of the world's hydrogen. It takes about 142 MJ to produce 1 kg of hydrogen. But it is also present in organic matter such as living plants, petroleum, coal etc. It is present as free element in the atmosphere, but only to the extent of less than 1 ppm by volume.

Safety is a prime requirement for the success of the hydrogen economy. Hydrogen can leak through tiny orifices 2.8 times faster than methane and 3.3 times faster than air because of its small molecular size [7]. Like most other fuels, hydrogen is flammable, and potentially hazardous if handled incorrectly. It is no more hazardous than other fuels, but has different properties which end users have to be aware in order to store, transport and use it safely. Hydrogen storage in open space is less risk than the storage of petrol, since hydrogen is very light and any leak would dissipate rapidly to air, reducing the risk of fire or explosion. But in a confined space, hydrogen could lead to fire or explosion if mixed with air. Any fire started would burn out quickly as the hydrogen is dissipated. Hydrogen burns with little radiation of heat, so nothing would burn unless it is immediately next to the flame. But, hydrogen gas stored in pressurized, containers would lead to cause explosion. Although hydrogen has a higher auto-ignition temperature than methane or gasoline, its low ignition energy characteristic makes it more readily ignitable than either of the hydrocarbon fuels. The hot air jet ignition temperature is highest for methane and lowest for hydrogen. The lower and upper explosive ranges are given in Figure 1.1.

Hydrogen is largely invisible to human senses, such as sight and smell. Sensors that selectively reveal the presence of hydrogen are needed to provide early warning of leaks before the flammability threshold is reached. Beyond human safety, such sensors would be useful for monitoring, optimizing, and controlling the technical operation of the hydrogen economy, such as fuel cell operation, the charge/discharge cycle of hydrogen storage devices, and hydrogen production by the water splitting or hydrocarbon reforming routes.

An obvious precaution against fire is the prevention of leaks in the hydrogen infrastructure through careful construction, sensing, and maintenance. Hydrogen presents special difficulties, however, because of its tendency to embrittle metallic container materials like stainless steel and its welded joints. Embrittlement arises

from hydrogen's ability to diffuse through metals readily, perhaps using grain boundaries as easy flow channels, and weakening internal metal-metal bonds by combining locally with host atoms. The embrittlement of metal occurs slowly and damages the hydrogen storage container catastrophically. Sensitive, selective sensors for detecting hydrogen would warn against the danger of fire or explosion in sheltered or enclosed areas.

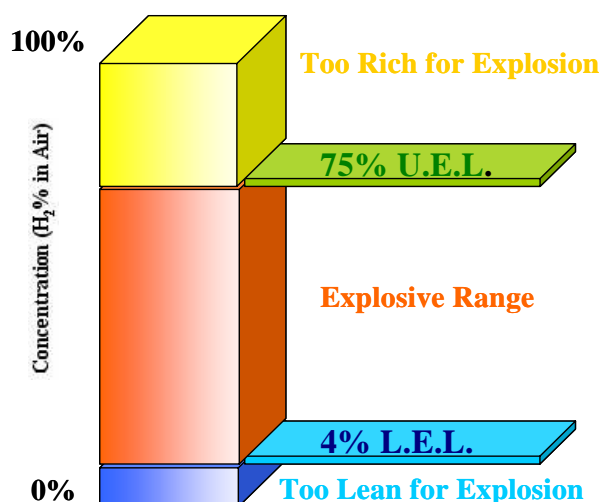


Figure 1.1: Schematic diagram of hydrogen gas explosion ranges in air

### 1.2 Application areas of hydrogen sensors

In the natural gas community, odorants are used so that any gas escape can be detected through smell. This is possible because mercaptan odorants, used in natural gas, track well with natural gas. The addition of mercaptan odorants is not a reasonable solution for hydrogen. It reacts chemically with hydrogen and could affect the sensing elements such as the catalytic electrode or polymer membrane electrolyte that cannot tolerate high levels of impurities. In many applications, the hydrogen concentration has to be known, even at ultra low concentrations of less than parts per million in air (ppm) [8]. There are several areas that are of interest for leak detecting and measuring hydrogen concentrations. A multitude of industries uses H<sub>2</sub> either as part of their process or as a fuel. Some of the major industries are:

*Chemical processing industries* are interested in measuring hydrogen concentrations to avoid catastrophic failures in the chemical plants. Although gas chromatography and mass spectrometry techniques are widely used for H<sub>2</sub> detection,

these methods require bulky, expensive equipment. In addition to safety concerns, accurate and real-time estimation of H<sub>2</sub> in the process is of great economic value for these industries. APCI (Air Products & Chemicals Inc) estimates that it can save € 95,000/annum/refinery by estimating the H<sub>2</sub> content accurately in the exhaust in real time [9].

In *Metallurgical industry*, hydrogen damage or high temperature hydrogen attack (HTHA) is produced in steel from the seepage of hydrogen that reacts with metal carbides to form methane gas. This reaction decarburizes the steel, produces micro cracks, and lowers the toughness of steel without necessarily a loss of thickness [10]. During molten aluminium processing, the most important dissolved gas is hydrogen, which is produced when aluminium reacts with moisture to form aluminium oxide and hydrogen [11]. The solubility of hydrogen in the liquid aluminium is much higher than that in solid aluminium, so dissolved hydrogen can lead to porosity during solidification.

In *Aerospace industry* are cryotechnic ones which use liquid hydrogen as combustible fuel in rocket engines. Due to its extremely low temperature, liquid hydrogen induces a contraction of the materials in contact, which combined with its very low viscosity leads to potential leakages. The most endangered parts of the engine are the connection flanges on the transfer lines, which have to support cycles of large thermal amplitude. Furthermore, the use of a thermal protection of the engine provides a closed area, which increases the potentiality of an explosive atmosphere. For all these reasons, even a small component leakage represents an unacceptable hazardous condition during loading operations, flights or after an abort launching. Detection of hydrogen leak and measurement of gas concentrations are essential quantities before any disaster to occur in aircrafts which allows to save billions of euros in the aerospace industry.

In *Medical diagnosis*, hydrogen is one of the gases produced in the intestinal lumen [12] by the bacterial breakdown of carbohydrates. Their bacteria are usually only present within the colon and as most carbohydrates are absorbed in the small intestine, formation of a small amount of hydrogen is healthy. However when there is malabsorption of any sugar, the colonic production of hydrogen increases and after diffusion to the bloodstream it appears in the expired air. Premature children exude hydrogen from their skin when they develop a devastating illness known as neonatal necrotizing enterocolitis, which is called a "hellish bacterial infection" of the intestines. This affects 5 to 10 % of all infants born prematurely getting this disease, and they die or end messed up because their digestive tract has to become surgically

removed. Recovery from the illness costs € 50 million in hospital expenses, so medical scientists are intensively looking for the best hydrogen sensors to catch the infection as soon as possible, before it has already done severe damage. In addition, application of hydrogen sensors as leak detectors are needed also in several areas in the medical diagnosis such as testing medical implants, medical consumables, medical instrumentation and medical packaging including the ability to locate leaks in balloon catheters, collection bags, blood bags and nourishment bags. A major attraction of hydrogen is the application in *Fuel Cells*. Hydrogen powered fuel cells are based on three large markets: automotive fuel cells, stationary or residential fuel cells and portable fuel cells. All fuel cells require two types of sensors, the first to monitor the quality of the hydrogen feed gas and the second, more important sensor system for leak detection. The higher efficiency of fuel cells (currently 60 % compared to 22 % for gasoline or 45 % for diesel IC engines) would dramatically improve the efficiency of future energy use. Coupling fuel cells to electrical motors, which are more than 90 % efficient, converts the chemical energy of hydrogen to mechanical work without heat as an intermediary. This attractive new approach for energy conversion could replace many traditional heat engines.

### 1.3 Types of hydrogen sensors

The major advantages of all solid-state hydrogen gas sensors are their simplicity in function, small size and low cost. The simplicity in function is in sharp contrast to some of the more classical analysis techniques, such as Gas Chromatography (GC), ion mobility spectroscopy and mass spectroscopy. The cost is low because the size of the solid sample used is small by the use of batch, planar fabrication technologies in fabricating the sensing device. The hydrogen sensors reviewed in this section are categorized into five general groups: (1) thermal sensors; (2) conductometric sensors (measurement of conductivity); (3) mass sensors; (4) optical sensors; and (5) electrochemical sensors. The categorization of these sensors is based primarily on the physical principles and operating mechanisms of the sensors are summarized below.

*Catalytic combustion bead sensors* - Combustible gas mixtures will not burn until they reach an ignition temperature. However, in the presence of certain chemical media, the gas will start to burn or ignite at lower temperatures. The catalytic bead sensor is comprised of a passive and active element, both made from an embedded coiled platinum wire in a porous ceramic. One bead is passivated, so that it will not react when it comes into contact with hydrogen gas molecules. The advantage is that the unit is very small and portable. The disadvantage is that unit is not amenable for

long-term in-situ operation. The catalytic bead sensor requires elevated temperatures for operation.

*Metal-oxide semiconductor sensors (MOS)* - The working principle of this type of sensor is that the resistance of the metal oxide semiconductor changes when it is exposed to the target gas because the target gas reacts with the metal oxide surface and changes its electronic properties. Two typical designs with tubular and planar structures are common in MOS field. Planar designs are especially promising in the design of a microsensor, a mass production approach, or a sensor array device. Many metal oxides have been investigated for hydrogen gas sensing, however, the most widely used is SnO<sub>2</sub> or doped SnO<sub>2</sub> for the active layer. New materials such as the rare earth oxides or gallium oxide are being used as the active sensor elements. Recent reviews [13,14] include many examples of this type of gas sensors.

*Chemiresistor sensors* - Chemiresistors are among the simplest sensor structures. When exposed to hydrogen, it adsorbs and dissociates on a thin strip of Pd metal [15,16], and occupies the octahedral interstitial sites in the Pd lattice. The occupied interstitial sites in the lattice act as additional scattering centres for electron transport through the metal. The resulting increased scattering of electrons increases the resistivity of the film. The change in resistivity is proportional to the hydrogen content in the metal lattice, which is proportional to the square root of the partial pressure of hydrogen gas (Sievert's law) [17]. These sensors can theoretically detect hydrogen from around 0.5 to 100 vol %. However, Pd undergoes a phase change (from hydrogen deficient to hydrogen rich phase) for concentrations of hydrogen in excess of ~10% at room temperature and atmospheric pressure. This change is accompanied by an increase in the lattice volume causing mechanical instability in the metal film.

*Field effect transistor (FET)* - hydrogen gas detection devices are consisting of a field effect transistor with a gate metallization exposed to the surrounding atmosphere. Hydrogen gas dissociates or decomposes on the surface; the protons diffuse to the metal/insulator interface and influence the charge in the semiconductor, thereby changing the drain source current. Common gate metallization are Pd or Pt. The operation temperature is limited to about 200°C on silicon FETs, to about 300°C on FETs with special barrier layer and to about 600°C for silicon carbide FETs [18].

*Surface acoustic wave sensors (SAW)* - the principle of operation of SAW sensors based on the transmission of a periodic deformation across the surface of a piezoelectric material, typically quartz. Changes in frequency of the transmitted wave are monitored as a function of the gas concentration. This kind of surface wave has a

higher frequency of about 100–500 MHz so that the sensitivity of this sensor is higher than for the quartz microbalance (QCM) sensor. Disadvantage of this method is the commonly short device lifetime.

*Optical fiber sensors* - Basically, when a thin palladium film is exposed to hydrogen it is converted to a palladium hydride film whose optical properties are different from those of a hydrogen-free Pd film. The hydration of palladium causes both the real and imaginary parts of the palladium refractive index to change. This in turn causes attenuation changes of the evanescent waves. The advantages are low power input, they can detect various chemicals at very low concentrations. The disadvantages are limited light transmission through the optical fiber over long distances, the concentration range sensitivity are limited and sensors that use chemically sensitive coatings may degrade with time.

*Electrochemical sensors* – is the direct conversion of chemical energy of the reaction involving species from the galvanic cell and the gaseous species under detection, into electrical energy. Or vice versa, by the application of electrical energy to a galvanic cell forcing the chemical reaction to occur. The electrochemical sensors classification type and their theoretical backgrounds are described in chapter 2.

The above techniques require in general complicated manufacturing processes in comparison to the electrochemical sensors and are limited to a number of detectable gases. In contrast, electrochemical techniques can be applied in a variety of extreme experimental conditions thus advantageous for a wide range of applications. Furthermore, electrochemical gas sensors provide directly electrical quantities, which may be easily measured.

#### 1.4 Motivation

The energy technology for future economy ultimately utilizes hydrogen in a gaseous form. For instance, fuel cells generally use platinum catalysts to break down the diatomic hydrogen gas into monoatomic hydrogen ions. It is a well known problem with the poisoning of platinum catalysts by other chemical species, therefore the hydrogen gas stream has to be kept as pure as possible to avoid degradation of the catalyst. All hydrogen based energy technologies require two types of sensors, the first monitors the quality and quantity of the hydrogen feed gas, and the second more important sensor system, for leak detection.

Hydrogen leak-detection sensors must detect over the general level of ambient conditions and in a variety of environments. For example, a sensor must be able to discriminate between ambient low-level sources of hydrogen and those which will be

generated by a hydrogen leak. A successful hydrogen leak-detection will depend on the following factors: no false alarms; integrated autonomous device shutoff or venting system; and reliable sensing, calibration and self-testing. Leak detection can be accomplished by two types of sensors: one to detect the leak and second alarm sensor with a set point at 50 % of LEL. The need for leak detection is especially important where there is a large volume of hydrogen consumed e.g. in residential/stationary applications, where the fuel gas circulates in an enclosed volume. Explosive limit sensor types are needed to operate continuously. For such alarm sensors, the detection range is 0.05 to 4 % H<sub>2</sub> in air, with response time of few seconds to tens of seconds.

Some precautions are required, however, for the safe use of hydrogen. Hydrogen has a large diffusion coefficient (0.61 cm<sup>2</sup>/s in air, while methane has a value of 0.15 cm<sup>2</sup>/s) and wide combustion range (4–75%) and small ignition energy (0.02 mJ in air, methane's value is 0.3 mJ). H<sub>2</sub> sensor is likely needed to develop in places where electrical power is not available at reasonable cost and so the initial energy source will be highly variable. Thus, H<sub>2</sub> sensors are then required to monitor the H<sub>2</sub> content in the gas as well as the pressure. H<sub>2</sub> concentrations can range from 4 to 99.9 %, depending on power generating device design. Commercially available high-temperature gas sensors consume relatively large power for device heating. The other type, an electrochemical gas sensor consumes very little power, but liquid electrolyte within the cell has to be replaced from time to time for the reliable operation. Thus, development of a new electrochemical hydrogen sensor that consumes negligible electrical energy with negligible maintenance and operable at ambient temperature, humidity, and pressure is highly desirable.

All sensors on the market suffer from slower response times (30–80 s). The size and operating temperature of the sensor is an important issue in cost reduction. The potential market to fulfil the future needs are estimated to be the number of sensors required for an automotive application is usually 6 to 10 sensors on the vehicle and possibly up to 10 sensors monitoring a stationary operation [19]. Thus, in order to fulfil the demands, a simple, fast and low cost hydrogen sensor device is necessary.

An effective electrode is one that correctly balances the transport processes required for a successful operation of any electrochemical cell. The large amount of platinum in PEM fuel cells is one of the reasons why fuel cells were excluded from commercialization. Thus, the development of the electrocatalytic active method was targeted and more specifically, on reducing the amount of platinum loading in the



electrodes. This continues to be a driving force for future research on catalytic active electrodes.

Solid polymer electrolyte (Nafion) and layered perovskite ceramic oxides (D-J phase) are known to show high protonic conduction at low temperatures in hydrogen atmospheres. This interaction seduces the development of hydrogen sensor for leak detection and concentration measurements. In the present work, i report the sensing characteristics of an amperometric (large extent to short circuit method) hydrogen sensor that is operated at and slightly above ambient temperature.

### *1.5 Structure of the thesis*

Chapter 2 contains the principles of the electrochemical sensors and its general characteristic for hydrogen detection. The scientific information reported in the literature in the area of amperometric hydrogen sensor is presented.

Chapter 3 the theoretical and fundamental aspects on solid-state electrochemical cell components as electrode and electrolyte materials suitable for hydrogen detection are presented. The structure and ionic conduction mechanism of both polymer and ceramic electrolyte materials and its preparation methods are reviewed. Thermodynamic equilibrium potential distribution models at the electrode/electrolyte interface are discussed as well.

Chapter 4 comprise the experimental conditions and parameters applied to prepare thin and thick film electrodes with three different deposition methods. The polymer and ceramic electrolyte protonation treatments and the preparation conditions are presented.

Chapter 5 presents the results of this work in two sections. The electrode and electrolyte of both polymer and ceramic based sensors performances and physical and chemical characterisation results are presented.

Chapter 6 contains a detailed discussion on both polymer and ceramic based sensor materials and the proton conduction mechanism in hydrogen sensing.

Chapter 7 finally, the optimised performance of sensing elements are engineered for a real time practical application to measure the hydrogen content in the biomass reactor. The prevention methods of CO<sub>2</sub> poisoning in noble electrode with three types of approach are described.

Chapter 8 contains summary and outlook of the most important results and accomplishments of this work.

### **References to chapter 1**

- [1] J. Ogden, *Physics Today* **55**, 69 (2002)
- [2] X. Shi, *Astrophys J.* **446**, 637 (1995)
- [3] C. Rolfs and W.S. Rodney, *Nuclear Physics A* **250**[2], 295 (1975)
- [4] E.G. Brovman and Y.M. Kagan, *Dyn. Prop. Solids* **1**, 191-300 (1974)
- [5] W.J. Nellis, *Philos. Mag. B* **79**[4], 655-661 (1999)
- [6] L. Wang, K. Murata and M. Inaba, *Appl. Catal. A*, **257**, 43-47 (2004)
- [7] J. Larminie and A. Dicks, “Fuel Cell Systems Explained”, Chichester, UK: John Wiley and Sons, pp. 280 (2003)
- [8] S.W. Myung, S. Huh, L. Kim, Y. Kim, M. Kim, Y. Kim, W. Kim and B. Kim, *J. Chromato. A* **791**, 367 (1997)
- [9] R.T. McGrath and M.W. Horn, “Solid State Hydrogen Sensors”, Technical Report, Penn State University (1999)
- [10] A.S. Birring, M. Riethmuller and K. Kawano, Ultrasonic Techniques for Detection of High Temperature Hydrogen Attack, Materials Evaluation (2005)
- [11] S. Shivkumar, L. Wang and D. Apelian, *JOM* **43**, 26 (1991)
- [12] M.D. Levitt, *J. Med.* **281**, 122 (1969)
- [13] W. Gopel and K. D. Schierbaum, *Sens. Actuators B* **26-27**, 1 (1995)
- [14] Y. Shimizu and M. Egashira, *MRS Bull.* **124**, 18 (1999)
- [15] D.P Smith, “Hydrogen in Metals”, The University of Chicago Press (1948)
- [16] F.A. Lewis, “Palladium Hydrogen System” Academic Press, London, New York (1967)
- [17] D. Lederman, Y. Wang, E.H. Morales, R.J. Matelon, G.B. Cabrera, U.G. Volkmann and A.L. Cabrera, *Appl. Phys. Lett.* **85**[4], 615 (2004)
- [18] P. Tobias, P. Martensson, A. Baranazhi, P Salomonsson and Lunström I, *Sens. Actuators B* **47**, 125-30 (1998)
- [19] A. Peter Jardine, “Hydrogen Sensors for Hydrogen Fuel Cell Applications”, DCH Technology Inc. technical Paper (2001)

---

## Chapter 2

### Principles and characteristics of electrochemical sensors

The chemically sensitive solid-state hydrogen sensor devices are based on the electrical response of the solid to its chemical environment. The term “solid-state” will be used quite broadly here to sensing component of materials not only catalytic metals and oxide materials but also different types of proton conducting polymeric electrolyte membranes.

#### 2.1 Electrochemical solid-state hydrogen sensor

Amperometry is an electroanalytical technique that is widely used to identify and quantify electro-active species in liquid and gas phases. For liquid phase analytes, the electrodes are immersed in a common solution which includes the analytes. In contrast, application of amperometry to gas-phase analytes involves unique interfacial transport processes and these processes frequently control the response of amperometric gas sensors. The characteristic of amperometric gas sensors is the measurement of the current in the electrochemical cell between working/sensing and counter/auxiliary electrodes at a certain potential [1]. This device is distinguished

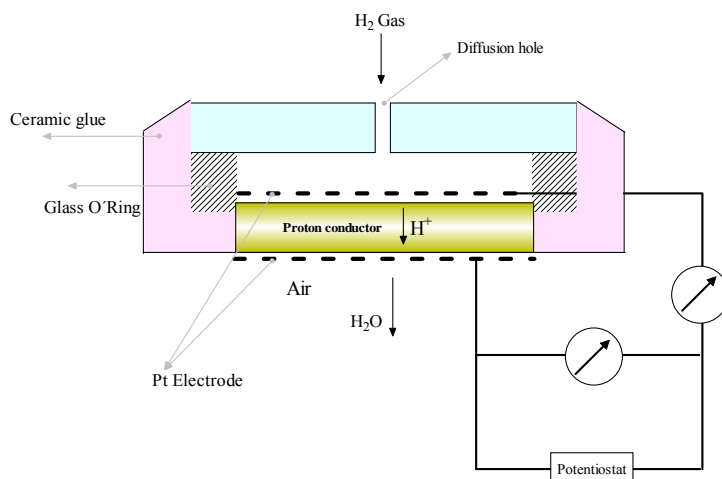


Figure 2.1: A schematic diagram of the principle of a limiting current hydrogen sensor with diffusion hole aperture.

from potentiometric sensors in which the potential at near zero current flow is the measured signal or conductometric sensors in which changes in impedance are the measured signal. In amperometric sensors a current is produced when exposed to a gas/vapour containing an electroactive compound because the analyte reacts within

the electrochemical cell either producing or consuming electrons, i.e., the analyte is electro-oxidized or electro-reduced at the solid electrode. This process can be accelerated by an electrocatalyst, such as Pt electrode or sacrificial electrode process as that occurs with Ag/AgCl or Pb/PbO<sub>2</sub> electrodes wherein the electrode material is consumed. By choice of a suitable geometry for gas exposure and electrolyte confinement and pre-empt materials for electrodes, as well as the electrochemical method, the sensor can be made quite sensitive for a particular analyte and quite insensitive to other gases. The most exciting characteristic features of amperometric sensors are the unique combination of low cost components, small size, and low power consumption. Thus, this sensor is most amenable to the design of a portable analysis system for a wide variety of chemicals. The Clark electrode for oxygen determination is one of the earliest successful amperometric gas sensors [2]. A detailed description of various types of Clark electrodes and their applications can be found elsewhere [3].

Figure 2.1 shows a schematic diagram of an amperometric gas sensor system. In general, the sensor consists of six major parts; filter, membrane/capillary, working or sensing electrode, electrolyte, counter electrode, and reference electrode. Each part of the sensor influences the overall performance and analytical characteristics of the sensor. Choosing appropriate materials for sensor construction and selecting an efficient sensor geometry is critical to sensor operation. The details of these parts in sensor design can have a profound influence on the accuracy, precision, response time, sensitivity, background noise current, stability, lifetime, and selectivity of the device.

## *2.2 General mechanism of electrochemical gas reactions*

The response of an amperometric gas sensor is described by the following seven steps,

- i. *Introduction of the gas phase compound to the sensor through the filter.* This involves a simple pneumatic system to physically transport gas to the sensor exposure chamber. Transport may occur either through diffusion or with mechanical pumping. The filter may act to enhance the selectivity of the sensor system by removing unwanted electroactive contaminants and protect the sensing electrode from dust.
- ii. *Transfer of the reactant from the gas chamber to the porous barrier in front of the working electrode and diffusion to the electrode/electrolyte interface.* A solid

membrane barrier in front of working electrode will mean that permeation process is required for the gas to reach the electrolyte. Laminar flow characteristics dominate in gas chambers of typical geometries. The transfer across the barrier or capillary is usually characterized by Fick's diffusion. It also provides structural support to the electrode assembly and the sensing electrode may be physically attached to the inner wall of the porous surface.

- iii. *Adsorption onto the electrode surface.* Prior to electrochemical reaction, the gas must adsorb onto the sensing electrode. If this process is very fast, the electrode surface sites become saturated at high gas partial pressures, and no further gas can be adsorbed until the adsorbed species is chemically changed.
- iv. *Diffusion of the analyte to the electrode/electrolyte interface.* The rate of mass transfer at the electrolyte/electrode interface and the diffusion of the gas in the electrolyte dramatically alter the sensor's sensitivity and response time to a specific analyte.
- v. *Electrochemical reaction.* The fundamental process for the electrochemical reaction is the transfer of electrons from species to the sensing electrode surface. Electron transfer reactions are usually very rapid and are not the rate-limiting step.
- vi. *Desorption of the products.* The working electrode surface will become saturated if the electrochemical reaction products do not desorb from the electrode surface.

### 2.2.1 Theory of the limiting current: steady-state current

Amperometric sensors often refer as a sensor works in the "limiting current region" in which the magnitude of the sensor signal is practically independent of the electrode potential. The sensor is based on the reaction of the gaseous species with the electroactive component under the condition of limited access of the gas by a kinetic barrier [4,5]. Theoretically limiting current region can be achieved in any case with the rate-limiting step prior to electron transfer. There are several possibilities for realization of diffusion limited current; the rate of electrode reaction may be limited by the rate of diffusion through a capillary which is placed somewhere between the gas stream and the catalyst layer of the electrode. The limiting current,  $i_{lim}$ , is accordingly

$$i_{lim} = \frac{nFA}{RTL} D_{H_2} P_{H_2} \quad (2.1)$$

where  $n$  is the number of electrons involved in the electrochemical reaction per molecule of the diffusing species,  $F$  is the Faraday constant,  $A$  is the effective area of the barrier,  $R$  is the general gas constant,  $T$  temperature,  $L$  length of the diffusion

channel,  $D_{\text{H}_2}$  diffusion coefficient of hydrogen, and  $P_{\text{H}_2}$  partial pressure of hydrogen. A typical geometry is shown with a hole type porous diffusion barrier in figure 2.1. Diffusion along the aperture surface is considered to be negligible [6]. Diffusion inside hole depends on the relative values of the hole diameter and the mean free path of the hydrogen molecules between two gas collisions.

If the rates of diffusion processes are much faster than the rate of reaction at the electrode surface, then the current is controlled by the rate of the electrode kinetics [7]. In this case an expression for the current is,

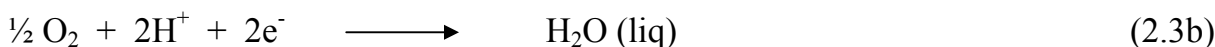
$$i = nFAK[P]^n[Q]^m \exp(\alpha nF/RT\eta) \quad (2.2)$$

where K represents the standard rate constant, n and m represent the order of the reaction for concentration of reactants P and Q respectively,  $\alpha$  and  $\eta$  are the transfer coefficient and overvoltage of the electrode reaction.

### 2.2.2 Short circuit amperometric method

A potentiometric sensor generates a voltage i.e generation of emf between two electrodes. If those electrodes are shorted by means of external load resistance, two types of response can be observed: either the cell is stable enough to sustain a steady-state current, or its electrodes are highly polarizable and the induced current falls to zero at a variable rate. The latter type of the response measurement of a current has been attractive in some cases. When hydrogen gas is analyzed in this manner and air is used as a reference, as in fuel cells, this type of device is frequently called “fuel cell” sensor or “short circuit amperometric” sensor.

In general, electrochemical redox processes take place at the electrodes, i.e., oxidation at the anode side and reduction at the cathode side [8],



Under short-circuit condition, reaction (2.3a) occurs at the sensing electrode, whereas reaction (2.3b) occurs at the counter electrode. Simultaneously, the protons move toward the counter electrode through the proton conducting electrolyte. This process results in a flow of an equivalent number of electrons as an external electrical current. The anodic oxidation reaction of hydrogen is limited by the diffusion process through the sensing electrode. The amount of protons produced is proportional to the hydrogen concentration in the gas phase, which can be derived from Faraday’s law,

which relates the number  $J_{H_2}$  of hydrogen molecules being transferred per second to the pumping current  $I$ ,

$$J_{H_2} = \frac{I}{2q} \quad (2.4)$$

where  $q$  is the elementary charge.

The flux of hydrogen diffusing through the aperture of an amperometric sensor is given by Fick's first law

$$J_{H_2} = AD_{H_2} \frac{\partial P_{H_2}}{\partial x} \quad (2.5)$$

where  $A$  is the area of the diffusion barrier,  $D_{H_2}$  the diffusion coefficient of  $H_2$  in the gas phase,  $P_{H_2}$  the hydrogen concentration and  $x$  the thickness of the barrier. Thus, eqns. (2.4) and (2.5) can be rearranged to give the electrical current

$$I = 2qAD_{H_2} \frac{\partial P_{H_2}}{\partial x} \quad (2.6)$$

The equation shows that the measurable current is directly proportional to the partial pressure of hydrogen. Figure 2.2 shows a typical voltage-current output characteristic of diffusion type amperometric sensor. Besides technical features which make a current measurement more convenient than a voltage measurement, the main advantage of this operating mode is its higher selectivity. Spurious electrode reactions which would interfere in potentiometric mode become negligible in short circuit mode, because of their very low reaction rate (high polarizable).

### 2.3 Characteristics of amperometric sensors

The amperometric sensor requires only small amount of power, this makes it ideal for portable and fixed site analyzer applications. The five characteristics of amperometric gas sensor technology are

- i. *The lower detection limit* – the lower detection limit for a particular gaseous compound is related to several factors including mass transport of the compound within the detection system, electrocatalytic activity, Faradaic equivalents per mole transferred during reaction, analyte solubility and mobility in the electrolyte, the physical geometry of the sensor, and the method of operation. It is the optimization of these parameters which leads to the maximum signal to noise ratio for a given analytical system.
- ii. *Sensitivity* is typically not limited by the Faradaic or electrocatalytic signal. Clearly, a current of 1 nA can be easily measured with existing electronic equipment. However, the background current and fluctuations thereof cause

the sensor to have a detection limit in the low ppm range.

- iii. *Stability* – the stability of an amperometric gas sensor relates to its ability to retain its original response characteristics over long time intervals and under changing environmental conditions. Stability is generally divided into short-term and long-term fluctuations.
- iv. *The response time*- In safety application, the speed of response is important and it can be controlled to a large extent in amperometric sensors. The response time of a potentiostatically controlled amperometric sensor is highly dependent upon the impedance between the reference electrode and the working electrode. The relationship between the impedance and an electroanalytical response has been described [9]. It is also possible that the response time of a sensor is limited by the mass transport of analyte to the reaction, especially when a very thick membrane is used in front of the cell.
- v. *The specificity or selectivity*- Typically, ppm levels are easily analyzed by an amperometric gas sensor. Interferences can be generally kept to an acceptable level either by selecting the proper electrocatalytic conditions or by using a selective adsorbent in the instrument inlet to remove undesirable electrochemically active contamination. The selectivity of amperometric gas sensor can be improved by careful consideration of thermodynamic and kinetic reaction parameters.

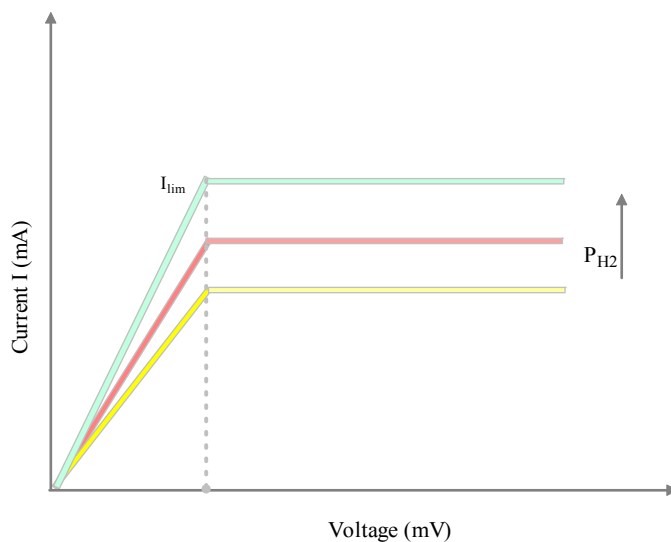


Figure 2.2: A typical voltage-current output characteristic of a diffusion limited amperometric sensor.



#### 2.4 State of the art on amperometric $H_2$ sensor

A number of commercial instruments are under development to determine quantitatively the concentration of hydrogen in several environments. In general Pt or Pd are used as active metals at the detector electrode [10,11]. Miremadi et al. [12] built a sensor selective to  $H_2$  and inert to CO,  $CH_4$ , propane and alcohols, using films of carbon prepared by an exfoliation technique. This sensor shows a response time of around 40 s for hydrogen concentrations between 3 and 300 ppm at 110 °C.

In the early 80's Miura et al. [13,14] developed a simple hydrogen sensor working at room temperature. It was the first report that short circuit amperometric principles were introduced in the hydrogen sensor field. Later, the same group reported at room temperature  $H_2$  sensor based on thick film of antimonite acid and PVA mixture by spin coating method. Liu et al. [15] investigated Pt/C/ Nafion composite electrode for hydrogen gas sensor by a hot pressed method with Pt loading of 3.0 mg/ $cm^2$  for a higher ppm detection range between 1260–5250 ppm. Another report [16] of the same group a modified Pt surface with polypyrrole (PPy) coated by chemical vapour deposition to improve the anti-ageing ability. The results indicate that the sensitivity of Ppy modified electrodes decreases markedly, from 0.0720 to 0.00313 mA/ $cm^2$  ppm. A similar type of Nafion based solid state sensor by Hwang et al. [17] describe oxygen detection in maximum of 0.5–5 % range. Ramesh et al. [18] utilized Pd as anode and a Pt as cathodes in PVA/ $H_3PO_4$  system to detect hydrogen injected to the measuring chambers in the 10–40 ppm range. The application of this sensor was extent to monitor corrosion control on carbon steels [19]. The effect of relative humidity on the Nafion 117 based  $H_2$  sensor between 33–95% RH was investigated by Samec et al. [20]. The results were compared between potentiometric and amperometric methods with fast response of three times higher than the former method.

Bera et al. [21] synthesized Pd nanoparticle arrays using templates (based on an Al film on a polycarbonate substrate) by assisted electrodeposition and propose this materials for a high sensitivity hydrogen detector system at room temperature. In amperometric sensors that use GDEs prepared with Pt/C, the conditions to determine low  $H_2$  concentrations are favoured due to the high surface area of the electrodes contributing to the determination of the currents. The detection interval with these materials is usually 0–10 % of  $H_2$ . Other metals, such as Pd [22], show high electrocatalytic activity for the hydrogen oxidation reaction (HOR). Contrary to the case of Pt and Pd, the HOR on Au surfaces [23] shows a very low activity. The use of GDE to build  $H_2$  sensors was described by La Conti et al. [24] in 1971 showing that a

fuel cell may be used as a detector if the configuration is appropriate. At that time the Pt load in GDEs, expressed in mass of Pt per unit of geometric area, was very high (5 mg Pt cm<sup>-2</sup>), but today the quantities used are lower than 0.4 mg Pt cm<sup>-2</sup>. Using solid polymer electrolyte/gas diffusion electrode based amperometry sensor number of design and detection range limit of various electroactive gases are listed in Table 2.1.

#### *2.4.1 Other methods*

Tabib-Azar et al. [25] report optical based hydrogen sensor using a Pd recovery onto the optical fibre core. When H<sub>2</sub> is adsorbed on Pd, the real and imaginary components of the refraction index change affecting the elasto-optic effect inside of the fibre. This system detects concentrations between 0.06 and 2% in the environment with a response time of around 20–30 seconds. Works which use the semiconductor properties of oxides such as TiO<sub>2</sub> doped with Pd [26], SnO<sub>2</sub> + Bi<sub>2</sub>O<sub>3</sub> doped with Pd [27], ZnO doped with Al [28] and V<sub>2</sub>O<sub>5</sub>-ZrO<sub>2</sub> [28] have been reported for applications in H<sub>2</sub> sensors, but these systems are not very sensitive. Chaudhary et al. [29] describe a sensor that uses PdO with RuO<sub>2</sub> on SnO<sub>2</sub> in which the distribution of Ru and Pd species favours the formation of defects on the surface and this contributes to the better selectivity and sensitivity of the system. The results show a system with linear response in a concentration range between 100 and 1000 ppm. Other H<sub>2</sub> sensors use different materials. Varghese et al. [30] used Ti nanotubes to detect H<sub>2</sub> with a good sensitivity in the temperature range 180–400 °C. This sensor showed the possibility of monitoring concentrations between 100 ppm and 4 % of H<sub>2</sub> in air. McCullen et al. [31], built a hydrogen sensor using a metal/AlN/Si(111) structure which behaves similarly to a metal-insulator-semiconductor-type capacitor. The AlN layer was deposited by plasma source molecular-beam epitaxy. The device uses alternating gates of Pd and Al and an Al black contact. The Pd gate structures were reported to be sensitive to hydrogen, down to the ppm range in the surrounding flow, while the Al gate structures showed no response to hydrogen.

This work describes the construction of a H<sub>2</sub> sensor using Pt on solid proton conductor (polymer/ceramic), prepared by the chemically reduced catalyst methodology as a detection electrode.

Table 2.1. Amperometric sensors for electroactive gases and their detection limit

Analyte	Type	Arrangement	Detection limit (ppm)	Upper limit (ppm)	Ref.
H <sub>2</sub>	SPE*	Pt/Nafion/0.1M H <sub>2</sub> SO <sub>4</sub>	n/a	5000	[32]
	GDE#	Teflon-bonded /5M H <sub>2</sub> SO <sub>4</sub>	n/a	40000	[33]
CH <sub>4</sub>	SPE	Pt/Nafion/10M H <sub>2</sub> SO <sub>4</sub>	1300	80%	[34]
	GDE	Teflon-bonded Pt/2M NaClO <sub>4</sub> in $\gamma$ -butyrolactone	60000	100%	[35,36]
C <sub>2</sub> H <sub>5</sub> O	SPE	Au/Nafion/1M NaOH	0.002	0.5	[37]
H	SPE	Au/Nafion/1M NaOH	1	476	[38]
	SPE	Pt/Nafion/1M H <sub>2</sub> SO <sub>4</sub>	n/a	10000	[39]
CO	SPE	Pt/Nafion/1M H <sub>2</sub> SO <sub>4</sub>	1.7	33000	[40]
	GDE	Teflon-bonded Pt/Nafion/H <sub>2</sub> O	n/a	10400	[41]
CO <sub>2</sub>	SPE	Pt/NASICON-	n/a	5%	[42]
	GDE	Na <sub>2</sub> CO <sub>3</sub> /BaCO <sub>3</sub>	<5%	50%	[43]
	GDE	Gore Tex/Pt/0.5M H <sub>2</sub> SO <sub>4</sub>	4000	100%	[44]
	Clark	Teflon/Pt/DMSO Teflon/Au/DMSO	n/a	15	[45]
O <sub>2</sub>	SPE	Pt/Nafion/1M H <sub>2</sub> SO <sub>4</sub>	n/a	5%	[46]
	GDE	Silicon-sieve/Pt/Nafion/H <sup>+</sup>	n/a	80%	[47]
	Clark	Teflon/Au/DMSO	n/a	90%	[48]
NO <sub>2</sub>	SPE	Au.Pt/Nafion/10M H <sub>2</sub> SO <sub>4</sub>	0.004,	1	[34]
	SPE	Au/NASICON-NaNO <sub>2</sub>	0.017	1	[49]
	SPE	C.Au/a-ZrPO <sub>4</sub> /TiHx	0.01	20	[50]
	SPE	Au/PVC/TBAHFP	0.01,0.1	5	[51]
	SPE	C/PVC/TBAHFP	0.075	2.2	[52]
	SPE	Au/Nafion/0.5M H <sub>2</sub> SO <sub>4</sub>	0.08	100	[53,54]
	SPE	Au/Nafion/1M HClO <sub>4</sub>	n/a	7	[55]
SO <sub>2</sub>	SPE	Au/Nafion,ADP/1M NaOH	0.0005	0.1	[56]
	SPE	Au/Nafion/0.5M H <sub>2</sub> SO <sub>4</sub>	0.0025	0.1	[34]
	SPE	Pt/Nafion/1M HClO <sub>4</sub>	0.18	4500	[57]
	GDE	TeFlon/Au/5M H <sub>2</sub> SO <sub>4</sub> in	0.5	200	[58]
	GDE		n/a	50	[59]

\* SPE- Solid Polymer Electrolyte; # GDE-Gas Diffusion Electrode

## References to chapter 2

- [1] W. Weppner, *Sens. Actuators* **12**[2], 107-19 (1987)
- [2] S.C. Chang, J.R. Stetter and C.S. Cha, *Talanta*, **40**, 461-477 (1993)
- [3] Y.H. Lee and G.T. Taso, *Adv. Biochem. Engineering.* **13**, 2-10 (1979)
- [4] J. Liu and W. Weppner, *Sens. Actuators B* **6**[1-3], 270-273 (1992)
- [5] J. Liu and W. Weppner, Ger. Offen. DE 4112302 A1 19921022 15 pp. (1992)
- [6] H. Dietz, *Solid State Ionics* **6**, 175-183 (1982)
- [7] J.R. Stetter, S. Zaromb and D. O’Gorman, *J. Electroanal. Chem.* **148**, 279-287 (1983)
- [8] N. Miura, H. Kato, N. Yamazoe and T. Seiyama, Proceedings of the American Chemical Society, pp. 203–214 (1986)
- [9] P.T Kissinger and W.R. Heineman, eds. *Laboratory Techniques in electroanalytical chemistry*, Marcel Dekker, New York, (1984)
- [10] B.K. Miremedi and K. Colbow, *Sens. Actuators B* **46**, 30-34 (1998)
- [11] G.S.V. Coles, G. Williams and B. Smith, *J. Phys. D. Appl. Phys.* **24**, 633-641 (1991)
- [12] B. K. Miremedi, S.R. Morrison, *Mater. Res. Bull.* **25**, 1139-1153 (1990)
- [13] N. Miura, H. Kaneko and N. Yamazoe, *J. electrochem. Soc.* **134**, 1875-1876 (1987)
- [14] N. Miura, H. Kato, Y. Ozawa and N. Yamazoe and T. Seiyama, *Chemistry Letters*, **11**, 1905-1908 (1984)
- [15] Y.C. Liu, B.J. Hwang and I.J. Tzeng, *J. electrochem. Soc* **149**, H173-H178 (2002)
- [16] Y.C. Liu, B.J. Hwang and Y.L. Chen, *Electroanalysis*, **14**, 556 – 558 (2002)
- [17] B.J. Hwang, Y.C. Liu and W.C. Hsu, *J. New Mater. Electrochem. Syst*, **2**[1], 33-38 (1999)
- [18] C. Ramesh, G. Velayutham, N. Murugesan, V. Ganesan, K.S. Dhathathreyan and G. Periaswami, *J. Solid State Chem.* **7**[8], 511-516 (2003)
- [19] C. Ramesh, N. Murugesan, A.A.M. Prince, S. Velmurugan, S.V. Narasimhan and V. Ganesan, *Corros. Sci.* **43**[10], 1865-1875 (2001)
- [20] Z. Samec, F. Opekar and G. Crijns, *Electroanalysis* **7**[11], 1054-1058 (1995)

- [21] D. Bera, S.C. Kuiry, S. Patil, S. Seal, *Appl. Phys. Lett.* **82**, 3089-3091 (2003)
- [22] P. Stonehart, *Phys. Chem.* **94**, 913-921 (1990)
- [23] D.T. Sawyer and E.T. Seo, *J. Electroanal. Chem.* **5**, 23-34 (1963)
- [24] A.B. La Conti and H.J.R. Maget, *J. Electrochem. Soc.* **118**, 506-510 (1971)
- [25] M. Tabib-Azar, B. Sutapun, R. Petrick and A. Kazemi, *Sens. Actuators B* **56**, 158-163 (1999)
- [26] N. Yamamoto, S. Tonomura, S. Matsuoka and M. Tsubumura, *Surf. Sci.* **92**, 400-406 (1980)
- [27] G.S.V. Coles, G. Williams and B. Smith, *J. Phys. D. Appl. Phys.* **24**, 633-641(1991)
- [28] A.R. Raju and C.N.R. Rao, *Sens. Actuators B* **3-4**, 305-310 (1991)
- [29] V.A. Chaudhary, I.S. Mulla and K. Vijayamohanan, *Sens. Actuators B* **50**, 45-51 (1998)
- [30] O.K. Varguese, D. Gong, M. Paulose, K.G. Ong and C.A. Grimes, *Sens. Actuators B* **93** 338-344 (2003)
- [31] E.F. McCullen, H.E. Prakasam, W. Mo, R. Naik, K.Y.S. Ng, L. Rimai and G.W. Auner, *J. Appl. Phys* **93**, 5757-5762 (2003)
- [32] F. Opekar, J. Langmaier and Z. Samec, *J. Electroanal. Chem.* **379**, 301-306 (1994)
- [33] V. Nikolova, I. Nikolov, P. Andreev, V. Najdenov, and T. Vitanov, *J. Appl. Electrochem.* **30**, 705-710 (2000)
- [34] P. Jacquinet, B. Müller, B. Wehrli, and P.C. Hauser, *Anal. Chim. Acta* **432**, 53-61 (2001)
- [35] T. Otagawa, S. Zaromb, and J.R. Stetter, *Sens. Actuators* **8**, 65-72 (1985)
- [36] T. Otagawa, S. Zaromb, and J.R. Stetter, *J. Electrochem. Soc.* **132**, 2951-2957 (1985)
- [37] P. Jacquinet, A.W.E. Hodgson, B. Müller, B. Wehrli, and P.C. Hauser, *Analyst.* **124**, 871-876 (1999)
- [38] G. Schiavon, N. Comisso, R. Toniolo, and G. Bontempelli, *Electroanalysis* **8**, 544-548 (1996)
- [39] P. Millet, A. Michas, and R. Durand, *J. Appl. Electrochem.* **26**, 933-937 (1996)
- [40] K.K. Xing, and C.C. Liu, *Electroanalysis* **3**, 111-118 (1991)
- [41] H. Yan, and C.C. Liu, *Sens. Actuators B* **17**, 165-168 (1994)
- [42] Y. Yang, and C.C. Liu, *Sens. Actuators B* **62**, 30-34 (2000)

- [43] A. Küver, W. Vielstich, and D. Kitzelman, *J. Electroanal. Chem.* **353**, 255-263 (1993)
- [44] Z.B. Zhou, Q. Wu, and C.C. Liu, *Sens. Actuators B* **21**, 101-108 (1994)
- [45] C.E.W. Hahn, H. McPeak and A.M. Bond, *J. Electroanal. Chem.* **393**, 69-74 (1995)
- [46] B.J. Hwang, Y.C. Liu and W.C. Hsu, *J. Solid State Electronchem.* **2**, 378-385 (1998)
- [47] M.J. Tierney and H.O.L. Kim, *Anal. Chem.* **65**, 3435-3439 (1993)
- [48] D.J. Gavaghan, J.S. Rollett and C.E.W. Hahn, *J. Electroanal. Chem.* **348**, 15-27 (1993)
- [49] H. McPeak and C.E.W. Hahn, *J. Electroanal. Chem.* **427**, 179-188 (1997)
- [50] G. Alberti, F. Cherubini and R. Palombari, *Sens. Actuators B* **37**, 131-134 (1996)
- [51] J. Langmaier, F. Opekar and Z. Samec, *Sens. Actuators B* **41**, 1-6 (1997)
- [52] P. Hrnčifova, F. Opekar and K. Stulik, *Sens. Actuators B* **69**, 199-204 (2000)
- [53] J.S. Do and R.Y. Shieh, *Sens. Actuators B* **37**, 19-26 (1996)
- [54] J.S. Do and W.B. Chang, *Sens. Actuators B* **72**, 101-107 (2001)
- [55] F. Opekar, *Electroanalysis* **4**, 133-137 (1992)
- [56] A.W.E. Hodgson, P. Jacquinet and P.C. Hauser, *Anal. Chem.* **71**, 2831-2837 (1999)
- [57] G. Schiavon, G. Zotti, R. Tonilo and G. Bontempelli, *Analyst* **116**, 797-802 (1991)
- [58] B. Chachuski, *Analyst* **123**, 1141-1144 (1998)
- [59] S.C. Chan and J.R. Stetter, *Electroanalysis* **2**, 359-364 (1990)

---

## Chapter 3

### Theoretical and Fundamental aspects on materials and methods

An amperometric sensor consists of the three major components, such as diffusion barrier, active catalyst, and proton conductor. The following section deals with mass transfer, catalyst selection, methods of preparations, gas-solid interactions, conduction mechanism, structural arrangements on the components, and thermodynamic equilibrium quantity distributions at electro-electrolyte interface.

#### *3.1 Gas diffusion layer*

Gas diffusion layers (GDL) used in amperometric gas sensor systems are usually of semihydrophobic type. Gas diffusion layer is the electrical conductor that transports electrons to and from the catalyst layer. The gas diffusion layer also assists the water management by allowing an appropriate amount of water be held at the electrolyte for hydration. There is a large number of research conducted on producing composite gas diffusion layers with graded porosity and various wettability by Teflon impregnation, as well as the optimization of carbon and binder loading in the gas diffusion layer [1]. These layers are composed of Teflon emulsion with high surface area noble metal catalyst powder deposited on a metal grid or on the surface of a totally hydrophobic porous Teflon coated carbon sheet/cloth. The resulting GDL consists of highly interlocked matrices of gas pores, electrolyte channels, electronically conducting paths and electrocatalytic surfaces as show in figure 3.1. It is porous enough to effect efficient gas permeation, has sufficient catalyst to be a good electronic conductor.

##### *3.1.1 Advantage of using gas diffusion layer*

When the catalytic layer of a gas diffusion layer (GDL) is placed somewhere between the capillary and the electrolyte, potentially independent limiting currents may appear if the kinetics of the electrochemical reaction is much faster than the rate of mass transfer through the diffusion barrier. Such a diffusion barrier can make amperometric sensors more stable. If the reaction is fast over a range of potentials, no potential control is required in the gas sensor. When the electrode reaction is slow, the potential of the sensing electrode must be precisely controlled to avoid drift in the sensor current. The gas diffusion electrode often consumes a significant portion of the gaseous reactant, the magnitude of the sensor signal will vary with the flow rate of the gas. Sedlak and Blurton [2] studied the limiting current in a three-electrode

amperometric gas sensor by measuring the flow rate dependence of the sensor signal. They reported an empirical analysis that included consideration of both mass transfer and electrochemical processes occurring in the gas sensor. The overall mass transfer equation for the electrochemical reaction in the sensor follows the relationship

$$\frac{dc}{dt} = -V \left( \frac{dc}{dx} \right) - k \int \frac{\partial c}{\partial t} dt \quad (3.1)$$

where  $c$  denotes the concentration of reactant,  $V$  represents the linear velocity of the gas flow, and  $k$  is the overall rate constant for transfer of reactant to the catalytic electrode. The first term on the right hand side of equation (3.1) refers to the conventional transport of the gaseous analyte and the second term refers to mass transfer of gaseous reactant through the electrode and diffusion barrier structure.

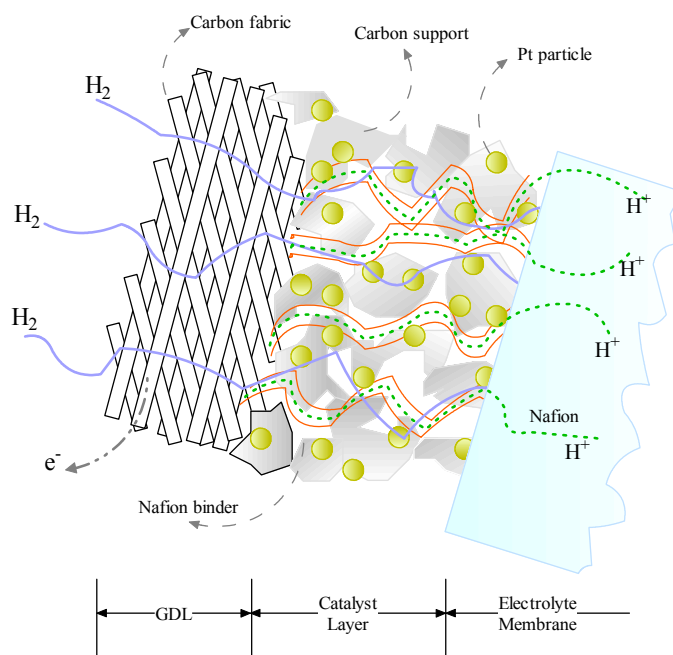


Figure 3.1: A schematic diagram of transport of hydrogen, proton, and electrons in the GDE electrode.

### 3.2 Choice of electrode materials

Electrocatalysis may be defined as the acceleration of an electrode reaction by a substance which is not consumed in the overall reaction. The substance is generally the catalytically active electrode surface. At a given electrode-electrolyte potential difference, specifically the properties of the electrode surface affect the overall reaction rates. The reaction in which several charge transfer steps must occur, the chemical processes are usually the ones which are kinetically slow and therefore rate determining. According to the Butler-Volmer equation, the low exchange current



density,  $i_o$  must be compensated by a high overvoltage.

The Butler-Volmer equation for  $|\eta_{\pm}| > nF / RT$  is :

$$i_{\pm} = i_o \left( \frac{a_{A_{\pm}}^a}{a_{A_{\pm}}^b} \right)^{\alpha_{\pm}} \exp(\pm \beta_{\diamond} (nF / RT) \eta_{\pm}) \quad (3.2)$$

where,

$a$  is the activity of the species A

$\alpha$  is the transfer factor

$i_{\pm}$  is current density as a measure of the reaction speed

$i_o$  is exchange current density as a measure of inhibition of the electrochemical reaction.

$\beta_{>}$ ,  $\beta_{<}$  is the anodic or cathodic charge transfer coefficients as a measure of the acceleration of the reaction

$\eta_{+}$ ,  $\eta_{-}$  is the anodic or cathodic overvoltage.

The chemical steps of an electrochemical reaction can be catalyzed by suitable heterogeneous catalysts. The group of heterogeneous catalysts are represented by Pt and other Pt metals or alloys, together with metals of the 8<sup>th</sup> group of the periodic system like, Fe, Co and Ni in finely divided form. They catalyse the electrochemical reaction by splitting of the hydrogen molecule into H atoms (and also the reverse reaction, combining H atoms to H<sub>2</sub> molecules) which is then followed by ionisation. The capability to catalyze these reaction can be correlated with the values for the adsorption enthalpy of hydrogen in Pt metal which has an optimum value of approx. 230 kJ/mol [3].

For cost saving reasons, active carbon materials have these catalysts deposited on their large surface areas [4]. Platinum noble metal is of best choice for electrode because of the high activity and stability in acid based solid electrolyte membrane.

### 3.2.1 Electrode preparation methods

Two widely employed catalyst designs are the metal paste and thin film coating as electrode. In general, electrode designs are differentiated by the structure and fabrication of the catalyst layer. The porous gas diffusion electrode in electrochemical cells ensures that reactants effectively diffuse and redox process occurs at the catalyst layer.

The catalyst layer is in direct contact with the electrolyte and the gas diffusion layer. It is also referred to as the electrocatalytic active surface. The catalytic electrode is either applied to the electrolyte or to the gas diffusion layer. In either case, the objective is to place the catalyst particles within close proximity of the membrane. There are several methods that have been developed and used in

electrochemical industry. In general, methods can be classified according to their preparation conditions. The most common methods and its performances are thin film deposition under vacuum environment, mechanical spray/brush method, thick film screen print, electro and electroless depositions.

Common vacuum deposition methods include chemical vapour deposition (CVD), physical or thermal deposition, ion beam assisted, pulsed laser beam deposition and sputtering. CVD is known for providing denser layer than the alternative evaporation methods [5]. Sputtering provides a method of depositing a thin catalyst layer onto either the electrolyte or the gas diffusion layer that delivers high performance combined with a low Pt loading. The success of the sputtering method on reducing catalyst loading depends heavily on the reduction in the size of particles e.g. 5 nm sputtered platinum film amounts of 1 mg /cm<sup>2</sup> [6]. The electrochemical cell performance of a sputter catalyst layer was less by several orders of magnitude compared to conventional Pt/C electrode and also it depends on the thickness of the sputtered catalyst layer [7]. The long exposure of H<sub>2</sub> causes the metallic Pt become more brittle due to formation of metalhydride at high temperatures. At the same time adhesion between electrode and electrolyte become poor and thin film peels off from the electrolyte surface due to the metalhydride brittleness. The reasonably suitable methods to prepare electrodes for such an electrochemical study are paste spray/brush and electroless deposition. Those methods are based on macroscopic and externally applied potential which can be easily controlled by mechanical arrangements. Moreover those techniques needs less number of instruments and are feasible for mass productions.

### *3.2.2 Paste/ Slurry route*

In this method, the catalyst particles are bound by a hydrophobic Teflon structure commonly deposited with the diffusion layer. This method is commonly used to reduce the platinum loading by a factor of 10, i.e., 4 to 0.4 mg/cm<sup>2</sup> [8]. In order to provide ionic transport to the catalyst site, the Teflon solutions are typically attached with electrolyte by brushing or spraying. However, platinum utilization in Teflon bound catalyst layers remains approximately 20% [9]. Nevertheless, researchers have continued to work on developing new strategies for electrolyte attachment [10]. A DLR research group in Germany [11] has developed a dry layer preparation method for fabricating catalyst layer bound by either Teflon or Nafion. The platinum loading in the electrode fabricated is reported to be as low as 0.08 mg/cm<sup>2</sup> with good cell performance. Paganin et al. [12] documented the results of a fuel cell with a thin film catalyst layer by brush the catalyst slurry onto the gas diffusion layer rather than the

membrane. This group was able to achieve good performance with Pt and Nafion loading of 0.4 and 1.1 mg/cm<sup>2</sup>, respectively, using 20 wt.% Pt/C catalyst particles. In 1993 Wilson [13] described the thin film of catalyst layer for PEM fuel cell with catalyst loading less than 0.35 mg/cm<sup>2</sup>. The binding material in the catalyst layer is composed of the same materials as the electrolyte membrane. Even though Teflon features effective binding qualities and imparts beneficial hydrophobicity in the gas diffusion layers, there is no particular benefit to its presence in the catalyst layer [14].

The advantage of these methods is that the catalyst metal is deposited directly onto the membrane or gas diffusion layer and no intermediate support is necessary.

### 3.2.3 Electroless wet route

An efficient way of depositing noble metals onto the membrane appears to be achievable by chemical reduction because of low investment and production cost. Japanese workers have proposed an electroless method for the deposition of noble metals on each face of the solid polymer membrane under wet conditions based on the diffusion through the membrane of a reducing agent which reacts with an anionic salt of the metal to be plated [15]. Platinum and palladium electrodes are interfaced with Nafion in this way, by the reduction of H<sub>2</sub>PtCl<sub>6</sub>, Pt(NH<sub>3</sub>)<sub>4</sub>Cl<sub>2</sub> or Pd(NH<sub>3</sub>)<sub>4</sub>Cl<sub>2</sub> with alkaline solutions of H<sub>3</sub>PO<sub>2</sub> or N<sub>2</sub>H<sub>4</sub>, the mechanism of the formation of the metal layer has been studied in detail [16] and its microstructural, and electrochemical properties are characterized intensively [17]. This method can be divided into two types, the Takenata-Torikai (T-T) method [18] and the impregnation-reduction (I-R) method [17]. The latter technique has been applied in the present investigation to obtain mechanically stable electrodes with good interfacial contact. The most important drawbacks of this technique which limit its application for large surface area production on polymer is due to the swelling nature of membranes.

### 3.3 Role of Catalyst / Gas solid interaction

Catalytic effects play an important role in the field of hydrogen gas detection. Solid-state gas sensors are directly related to the phenomenon of catalysis. Catalytic processes not only control the rate at which a chemical reaction approaches equilibrium but also affect sensitivity and selectivity. The ideal catalyst is one which increases the rate of the gas-surface interaction without itself becoming permanently affected by the reaction. Thus, the response time will be fast and the process will be reversible. In 1986, Gentry and Jones [19] have given five factors which affect the catalytic reaction

- (i). Transport of gases to the solid surface
- (ii). Adsorption of the gases on the solid surface
- (iii). Reaction between the adsorbed species and or with the solid surface
- (iv). Desorption of surface species and the products of surface reactions
- (v). Transport of the gaseous reactants and products away from the surface

### *3.3.1 Physisorption and chemisorption*

In general gas adsorption on surfaces occurs in two types,

*Physisorption*: weak attraction followed by gas adsorption due to van der Waals forces; physisorption is characterized by a low heat of adsorption.

*Chemisorption*: when the gas interacts with solid surfaces, the formation of chemical bond occurs through an exchange of electrons with the surface; the heat of chemisorption is higher than that of physisorption and it is 26 kcal/mol for hydrogen on a Pt surface. In sensor technology mostly metals and semiconductor metal oxides [20] are used as a catalytic materials. In metals, the electrons involved in chemisorption are the free electrons of the incomplete *d*-band. On other hand side, the noble metals (Pt, Pd, Rh, Ir) are the most active catalysts [21], they possess a partially filled *d*-band.

### *3.3.2 The Platinum-Hydrogen system*

The absorption of hydrogen by Pd during electrolysis was observed in 1868 by Thomas Graham [22] and for selectivity to hydrogen absorption, Pd has been employed as a filter for hydrogen purification and has also been used to provide hydrogen selectivity for various hydrogen detectors. The great similarity between Pd and Pt allows a reasonable comparison to be made between the results of Thomas Graham and the hypothesis put forth by Lundström in 1981 [24]. In order to discuss a hydrogen sensor response as a function of concentration, it is necessary to recall the surface-gas interaction in the hydrogen-platinum system. Gas-surface interactions are important as charge transfer mechanisms at the gas-solid interface on an atomic scale. In the hydrogen-platinum system the flux of the surface impinging molecules,  $\Phi_0$  of a gas is proportional to the partial pressure of the hydrogen,  $P_{H_2}$ , the gas molecular weight  $M_0$  and the absolute temperature  $T$ , assuming low enough concentrations and no interference from other ambient gases. According to the kinetic theory of gases,

the flux of gas molecules is given [23]

$$\Phi_o = \frac{N_A P_{H_2}}{(2\pi M_o RT)^{1/2}} \approx 3 \times 10^{22} \frac{P_{H_2}}{(M_o T)^{1/2}} \quad (3.3)$$

where  $N_A$  is the Avogadro's number and  $R$  is the gas constant.

The atomic hydrogen pressure in a medium is given as a function of molecular pressure in the gas phase in order to interpret with the known parameter i.e  $P_{H_2}$ .

### 3.3.2.1 Langmurian model in an inert atmosphere

In the case of an inert atmosphere, the only reaction [24] taking place on the Pt metal surface is



This reaction represents the dissociation of hydrogen on the Pt catalyst;  $H_a$  is the adsorbed hydrogen atom,  $c_1$  and  $d_1$  are the rate constants of the reaction. After the absorption of hydrogen into and diffusion through the Pt bulk particle, another reaction takes place:



where  $c_s$ ,  $c_i$ ,  $d_s$  and  $d_i$  are rate constants;  $H_b$  and  $H_i$  are the atomic hydrogen in the Pt bulk electrode and at the electrode/electrolyte interface. Assuming that the number of hydrogen adsorption sites per unit area on the Pt surface is  $N_s$  and that on the Pt-proton conductor interface is  $N_i$ , one can write:

$$\frac{n_i}{N_i - n_i} = \frac{d_i}{c_i} \left( \frac{n_b}{N_b - n_b} \right) = \frac{c_s d_i}{d_s c_i} \left( \frac{n_s}{N_s - n_s} \right) \quad (3.6)$$

where  $N_b$  is the number of absorption sites in the bulk Pt particle;  $n_i$ ,  $n_b$ , and  $n_s$  are the concentrations of the adsorbed hydrogen atoms on the Pt-proton conductor interface, bulk Pt and surface, respectively.

At equilibrium the forward and backward rates are equal, so that

$$c_1 [H_2] = d_1 [H_a]^2 \quad (3.7)$$

from Eqs. (3.4) (3.6) and (3.7) follows

$$\frac{n_i}{N_i - n_i} = \left[ \frac{c_1}{d_1} P_{H_2} \right]^{1/2} \quad (3.8)$$

The coverage of hydrogen at the surface,  $\Theta_s = n_s/N_s$ , and at the Pt-proton conductor interface,  $\Theta_i = n_i/N_i$ . By combining the Eqs. (3.6) and (3.8) and by taking

into account the definition of the coverage on can write:

$$\frac{\Theta_i}{1-\Theta_i} = A_H \frac{\Theta_s}{1-\Theta_s} = K [P_{H_2}]^{1/2} \quad (3.9)$$

where  $A_H = c_s d_i / d_s c_i$  and  $K$  is a constant [ $K = (c_i / d_i)^{1/2}$ ] [24] that depends mainly on the difference in adsorption energies at the surface and interface, respectively;  $K$  is given by the relation [23]

$$K(T) = 2.5 \times 10^{-5} \left[ \frac{A_r}{T M_o} \right]^{1/2} \exp\left(-\frac{\Delta E_a}{2RT}\right) \quad (3.10)$$

where  $A_r$  is a temperature constant and  $\Delta E_a$  is the heat of adsorption per molecule i.e per two atoms. The value of  $\Delta E_a$  is approximately 1eV. Finally, the coverage of hydrogen,  $\Theta_i$ , can be written as a function of the hydrogen partial pressure,

$$\Theta_i = \frac{K(T) [P_{H_2}]^{1/2}}{1 + K(T) [P_{H_2}]^{1/2}} \quad (3.11)$$

Equation (3.11) is valid only in the case where the platinum catalyst surface is clean and exposed to hydrogen. A different approach must be derived for the catalyst exposed in the presence of air.

### 3.3.2.2 Langmuirian model in the presence of air

The ambient oxygen plays an important role on the catalyst surface exposed to air before hydrogen gas introduced into the detector chamber. Preadsorbed  $O_2$  on the Pt surface reacts with the introduced  $H_2$  gas and forms  $H_2O$ , which leaves the Pt surface via evaporation and also it enhances the catalytic activities. The possible mechanism on the Pt surface: dissociation-recombination of oxygen and hydrogen:



and water formation:



According to Lundström et al, one can write:

$$\frac{\Theta_i}{1-\Theta_i} \propto \left[ \frac{P_{H_2}}{P_{O_2}} \right]^{1/2} \quad (3.15)$$

However, according to Lundström the details of the water production on the noble metal surface are still not known.

### 3.4 Choice of electrolyte materials

#### 3.4.1 Solid Polymer electrolyte membrane (PEM)

The evolution of membranes for electrochemical device applications started as early as 1959 by GE with the testing of phenolic membranes, prepared by polymerization of phenol-sulfonic acid with formaldehyde. These membranes had low mechanical strength and a short lifetime of 300–1000 h [25]. Membrane materials used in electrochemical industry generally fall into different membrane systems, which can be classified as

- (i). Perfluorinated ionomers,
- (ii). Partially fluorinated polymers,
- (iii). Non-fluorinated membranes with aromatic backbone,
- (iv). Non-fluorinated hydrocarbons,
- (v). Acid-base blends

In 1970s, Du Pont developed a perfluorosulfonic acid called “Nafion<sup>®</sup>” that not only showed a two-fold increase in the specific conductivity of the membrane but also extended the lifetime by four orders of magnitude ( $10^4$ – $10^5$  h). The sulfonic acid groups are chemically bound to the perfluorocarbon backbone as illustrated in figure 3.2. This soon became a standard for solid polymer electrolyte membrane in

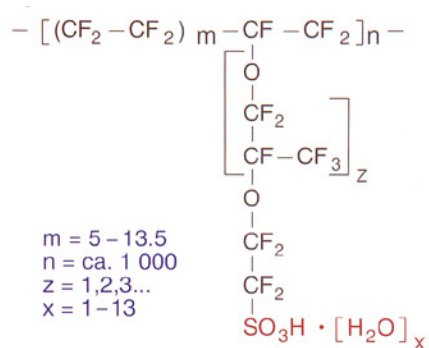


Figure 3.2: Chemical structure of Nafion.

electrochemical studies and remains so till today. Similar polymers are Flemion<sup>®</sup> produced by Asahi Glass and Aciplex-S<sup>®</sup> produced by Asahi Chemical. Among the three major types, the DuPont product is considered to be superior because of its high proton conductivity, good chemical stability and mechanical strength [26]. The proton conductivity in Nafion is dependent upon its microstructure and water content. In the presence of water, protons as well as the sulfonic acid groups are in the solvated form, and this greatly facilitates the hopping mechanism of protons. To understand the transport of water in perfluorosulfonic acid membranes, quantitative

and qualitative modeling studies were conducted for supporting the optimization of not only the composition of the membrane but operating conditions. In terms of microscopic models, there are many models based on statistical mechanics, molecular dynamics and macroscopic phenomena applied to the microscopic structure of the membrane. These models provide a fundamental understanding of processes like diffusion and conduction in the membrane on a microscopic scale in the early 1980s. Gierke and Hsu [27] were proposed a microscopic structure model for perfluorinated sulfonic group polymers. They describes geometric and phenomenological relationship for the swelling of the polymer due to the uptake of water and its effect on the diffusion coefficient of water in the membrane pores. It has been widely accepted description of the polymeric membrane in terms of an inverted micellar structure in which the ion-exchange sites are separated from the fluorocarbon backbone thus forming spherical clusters (pores), which are connected by short narrow channels. The model was hence termed as ‘cluster network’ model. A schematic of the cluster network model is depicted in figure 3.3.

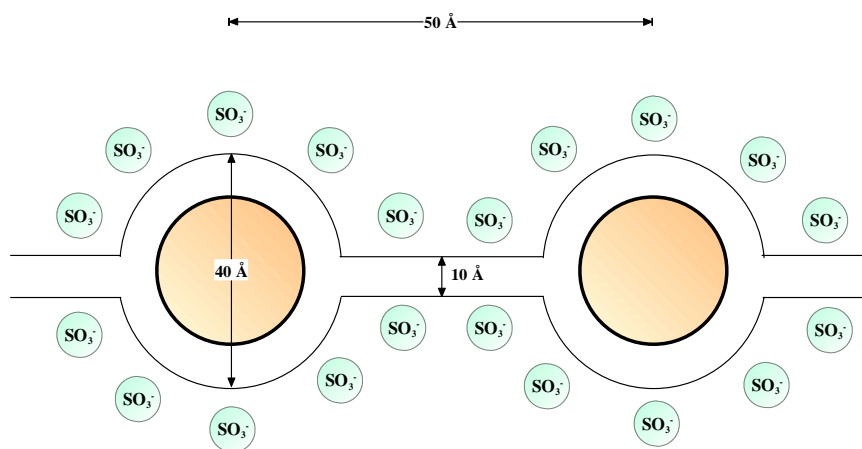


Figure 3.3: Schematic of the cluster network model describes the distribution of sulfonate groups in Nafion membrane.

Macroscopically, the water containing membrane is distinguished in two different water environments in Nafion. For instance, the water in the middle region of the pore is referred to as “bulk water,” through which the mobility of protons is fast. However, water near the pore surface along the array of SO<sub>3</sub><sup>-</sup> groups is referred to as “surface water,” and the proton mobility through the surface is considerably smaller than that in the bulk, due to the strong electrostatic attraction of SO<sub>3</sub><sup>-</sup> groups. Therefore, the proton conductivity of Nafion at a given water content is the result of



weighted average of the surface and bulk conductivities, depending upon the radial distribution of protons and water content in Nafion [28] and can vary by two or more orders of magnitude as the RH is increased from dry conditions to saturations. According to the Datta [29] assumption that the transport of protons in Nafion is via

- i. a surface diffusion mechanism occurring close to the pore wall or under low water activity, *i.e.*, in a layer of around 1 nm from the pore wall [30] and
- ii. a bulk diffusion mechanism prevailing in the central region of the pore or under high water activity condition [31]. In the bulk, proton diffusion is predominantly via the Grotthuss mechanism, but the  $H_3O^+$  ion also undergoes traditional mass diffusion [28], *i.e.*, the so-called *en masse* diffusion.

Figure 3.4 shows the various proton transport mechanisms along with an electrical analog. Thus, the proton conductivity in a pore  $\sigma_p$  can be written as

$$\sigma_p = \sigma_{H^+}^S + \sigma_{H^+}^G + \sigma_{H^+}^E \quad (3.16)$$

where  $\sigma_{H^+}^S$ ,  $\sigma_{H^+}^G$ , and  $\sigma_{H^+}^E$  represent the contributions of proton conductivity from the surface, Grotthuss, and *en masse* diffusion mechanisms, respectively.

The proton conductivity can be written in terms of the diffusion coefficient and concentration using the Nernst-Einstein relation [32, 33]

$$\sigma_{H^+}^\alpha = \frac{F^2}{RT} D_{H^+}^\alpha C_{H^+}^\alpha \quad (3.17)$$

For *en masse* diffusion, the diffusion coefficient can be written as [34]

$$\frac{1}{D_{H^+}^E} = \frac{x_w}{D_{H^+}^W} \left( 1 + \frac{1-x_w}{x_w} \frac{D_{H^+}^W}{D_{H^+}^M} \right) \quad (3.18)$$

where  $x_w$  is the mole fraction of water in the membrane phase, and  $D_{H^+}^W$ , and  $D_{H^+}^M$  are the Stefan-Maxwell diffusion coefficient of hydronium ion and bulk water in the pore, and hydronium ion and the polymer matrix M, respectively [35]. Because the water mole fraction in the proton exchange membrane is high even at low activity, *e.g.*,  $x_w = 0.67$  at activity  $a_i = 0.1$ , and quickly approaches 1, Eq. 3.18 may be simplified to

$$\frac{1}{D_{H^+}^E} \approx \frac{1 + \delta_c}{D_{H^+}^W} \quad (3.19)$$

where  $\delta_c \equiv (D_{H^+}^W / D_{H^+}^M)[(1-x_w)/x_w]$ . Thus, the total proton conductivity in a pore within Nafion can be written in terms of diffusion coefficients, concentrations, and the

ratio  $\delta_c$ :

$$\sigma_p = \frac{F^2}{RT} \left( D_{H^+}^S C_{H^+}^S + D_{H^+}^G C_{H^+} + \frac{D_{H^+}^W}{1 + \delta_c} C_{H^+} \right) \quad (3.20)$$

Next, to account for the tortuous nature of the pores and the reduced cross-sectional area available for proton transport, the parallel pore model [36] is utilized. The effective diffusion coefficient for the membrane is thus obtained by multiplying the diffusion coefficient for a single pore by  $\varepsilon_i/\tau$ , where  $\varepsilon_i = \lambda_i/(\lambda_i + r)$ ,  $\lambda_i$  is the moles of water sorbed per acid site,  $r$  is the ratio of partial molar volume of membrane to that of water [37], and  $\tau$  is the tortuosity factor [38]. Then, the overall membrane conductivity  $\sigma_{H^+}$  is

$$\sigma_{H^+} = \frac{\varepsilon_i}{\tau} \left[ \frac{F^2}{RT} \left( D_{H^+}^S C_{H^+}^S + D_{H^+}^G C_{H^+} + \frac{D_{H^+}^W}{1 + \delta_c} C_{H^+} \right) \right] \quad (3.21)$$

Therefore, the total conductivity depends upon the structural characteristics represented by  $\delta_c$  and  $\tau$ , as well as the distribution of proton concentration between the surface ( $C_{H^+}^S$ ) and the bulk regions ( $C_{H^+}$ ) within the membrane, which in turn are determined by the acid strength of the functional groups. The diffusion coefficient of surface, Grotthuss, and *en masse* diffusion mechanism values are reported as  $D_{H^+}^S = 1.01 \times 10^{-7} \text{ cm}^2/\text{s}$ ,  $D_{H^+}^G = 7 \times 10^{-5} \text{ cm}^2/\text{s}$ , and  $D_{H^+}^E = 1.71 \times 10^{-5} \text{ cm}^2/\text{s}$  respectively [39].

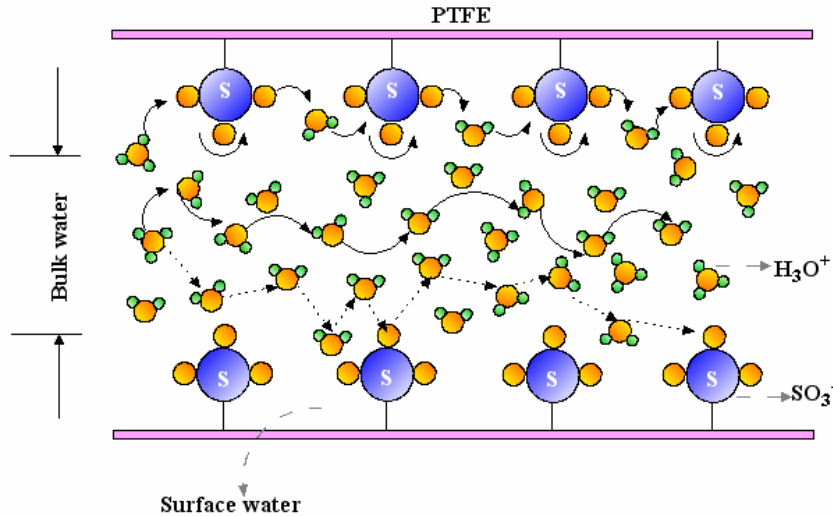


Figure 3.4: A schematic picture of structure and proton transfer in Nafion in fully hydrated state.

### 3.4.2 Solid oxide perovskite type electrolyte

#### 3.4.2.1 Ideal perovskite

Ideal perovskites have the general formula  $ABX_3$ , where the *A*-site cations are typically larger than the *B*-site cations and similar in size to the *X*-site anion. Figure 3.5 shows that in this structure the *A* cations are surrounded by twelve anions in cubo-octahedral coordination and the *B* cations are surrounded by six anions in octahedral coordination. The *X* anions are coordinated by two *B*-site cations and four *A*-site cations. Perovskite having the ideal structure adopt the cubic space group  $Pm\bar{3}m$ .

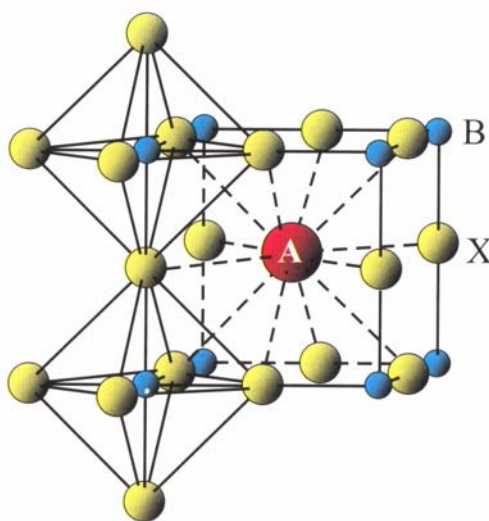


Figure 3.5: The ideal  $ABX_3$  perovskite structure showing the octahedral *B*-site and cubo-octahedral *A*-site.

#### 3.4.2.2 Layered perovskite

The structure of layered perovskites and their derivatives are characterized by excess anion relative to ideal perovskite. Currently, such layered perovskites are considered to form three groups of homologous compounds, which are defined on the basis of the interlayer composition or orientation of the layer plan relative to the aristotype cubic lattice as:

- 1) The  $A'[A_{n-1}B_nX_{3n+1}]$  or Dion-Jacobson (D-J) series with layering parallel to  $\{001\}$ , e.g.,  $KCa_2Nb_3O_{10}$  (figure 3.6a);
- 2) The  $A_{n+1}B_nX_{3n+1}$  or  $A'_2[A_{n-1}B_nX_{3n+1}]$  or Ruddlesden-Popper (R-P) series with layering parallel to  $\{001\}$  e.g.,  $Sr_3Ti_2O_7$  (figure 3.6b); and
- 3) The  $(Bi_2O_2)[A_{n-1}B_nX_{3n+1}]$  or Aurivillius phases with layering parallel to  $\{001\}$ , e.g.,  $Bi_4Ti_3O_{12}$  (figure 3.6c).

These perovskite like fragments of the structures are referred to as slabs containing  $n$  layers of  $BX_6$  octahedra, with the separation between the layers being termed the interlayer distance. The structures of layered perovskite type compounds were reviewed by Aleksandrov [40] and Aleksandrov & Beznosikov [41].

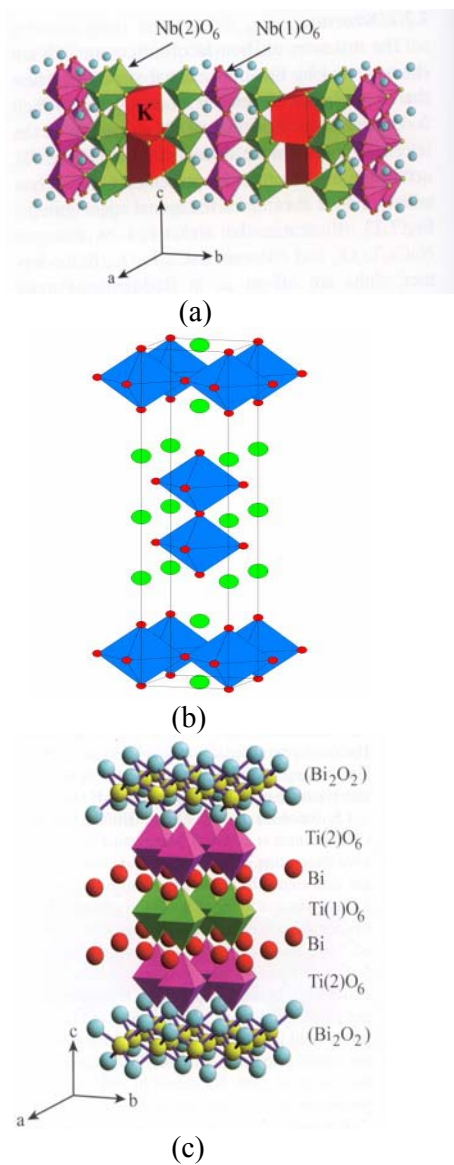


Figure 3.6: The structure of Layered perovskite phase compounds (a) Polyhedron representation of the structure of D-J phase e.g.  $KCa_2Nb_3O_{10}$ , (b) Ruddlesden-Popper phase e.g.  $Sr_3Ti_2O_7$  and (c) the ideal Aurivillius compound e.g.  $Bi_4Ti_3O_{12}$ .

### 3.4.2.3 Dion-Jacobson phase

The A-site ordered compounds  $A'[A_{n-1}B_nX_{3n+1}]$  (where  $A' = H, NH_4$ , alkali metals;  $A = Ca, Sr, La, Ba$ ;  $B = Ti, Nb, Ta$ ) are intensively studied because of their ion-exchange, intercalation, ionic conduction and luminescence properties. These compounds, termed the D-J series by Gopalakrishnan et al. [42] after the initial descriptions by Dion et al. [43] and Jacobson et al [51] are similar in their structure to the R-P compounds but differ in that they contain A-site ordered cations and only one sheet of interlayer A-cations. The lower interlayer alkali ion density favours ion exchange and promotes higher ionic conductivity as compares to the R-P compounds.

### 3.4.3 Ionexchangeability of layered perovskites / IEC of layered perovskites

D-J compounds have been subject of many investigations because of the ease with which ion exchange or intercalation occurs in molten salts or acidic solutions as consequence of the low charge density in the interlayers, relative to that of R-P compounds. Dion-Jacobson phases were the first reported examples of ion-exchangeable layered perovskites, and the initial ion-exchange reactions involved the replacement of larger interlayer cations such as  $Cs^+$ ,  $Rb^+$ , and  $K^+$  with smaller cations such as  $Na^+$ ,  $Li^+$ , and  $NH_4^+$  using molten nitrate salts ( $T_m \sim 300\text{ }^\circ C$ ) as the ion-exchange medium [44,45]. Dion-Jacobson phases containing small interlayer cations such as  $Li^+$  or  $Na^+$  are often difficult to synthesize as phase-pure materials at traditional solid-state reaction, occurs at higher temperatures ( $>1000\text{ }^\circ C$ ) where three-dimensional perovskites are usually more stable. Larger cations, such as  $Cs^+$ , favour the formation of layered perovskites because  $Cs^+$  fits better in the large interlayer A'-site of a layered perovskite than in the smaller A-site of a three-dimensional perovskite [46]. Smaller cations are often desired between the layers, however, because of the improved ionic conductivity [47,48] and the cation-size considerations that are crucial for subsequent low temperature reactions [49]. Divalent ion exchange of Dion-Jacobson phases is also possible [50], although it results in phases that have less than half of the interlayer sites filled. In addition, the exchange efficiencies are often low compared with those involving monovalent ion exchange. The reported studies have focuses on the ion exchange of alkali metals by monovalent cations or protons e.g.  $HCa_2Nb_3O_{10}$  from  $KCa_2Nb_3O_{10}$  in 6 M aqueous HCl at  $60\text{ }^\circ C$  [51];  $AgLaNb_2O_7$  form  $RbLaNb_2O_7$  in a  $AgNO_3$  melt at  $230\text{ }^\circ C$  [52]. Protonation of D-J compounds reported by Jacobson et al. [51]  $KCa_2Na_{n-3}Nb_nO_{3n+1}$  and Gopalakrishnan [45]  $K_{1-x}La_xCa_{2-x}Nb_3O_{10}$  series results in a change from orthorhombic to tetragonal symmetry. In these compounds the proton is bonded to a terminal layer oxygen to form an OH group that is hydrogen bonded to a terminal oxygen atom from an

adjacent layer. Hydrated protonated compounds also form during ion exchange with H<sub>2</sub>O groups located in the interlayer region. Mangamma et al. [53] have shown in these compounds layers of H<sub>2</sub>O are sandwiched between half occupied proton sites located adjacent to the terminal oxygens of the perovskite layers. The location of H<sub>2</sub>O groups in hydrated, but non-protonated, compounds such as NaLaNb<sub>2</sub>O<sub>7</sub>.xH<sub>2</sub>O has been described by Sato et al. [54]. In this compound Na is present in two eight-fold coordinated interlayer sites and is hydrogen bonded to four water molecules and four oxygen atoms associated with the NbO<sub>6</sub> octahedra. In the anhydrous form Na occurs in only one site in perfect tetrahedral coordination. Because of the similarities in structure, D-J phase can be transformed into R-P phase by intercalation of cations e.g. Na<sub>2</sub>Ca<sub>2</sub>Ta<sub>3</sub>O<sub>10</sub> from NaCa<sub>2</sub>Ta<sub>3</sub>O<sub>10</sub> by reaction with sodium nitrate at 400 °C [55] and Rb<sub>2</sub>LaNb<sub>2</sub>O<sub>7</sub> from RbLaNb<sub>2</sub>O<sub>7</sub> by reaction with Rb vapour at 250 °C [56]. In addition Aurivillius phases can also be exchanged with D-J and R-P phases, e.g. (Bi<sub>2</sub>O<sub>2</sub>)BiPbTi<sub>2</sub>NbO<sub>10</sub> [57].

In 1966, the ionic conduction mechanism in oxide materials was proposed by Stotz and Wagner [58]. The existence of protonic defects in wide band-gap oxides at high temperatures may be extended to proton conduction in perovskites, by the reaction leading to the formation of protonic defects at moderate temperatures is the dissociative absorption of water, which requires the presence of oxide ion vacancies, V<sub>o</sub><sup>••</sup>. The vacancies may be formed intrinsically by varying the ratio of the main constituents, or they may be formed extrinsically to compensate for an acceptor dopant. In order to form protonic defects, water from the gas phase dissociates into a hydroxide ion and a proton; the hydroxide ion fills an oxide ion vacancy, and the proton forms a covalent bond with a lattice oxygen. In Kröger-Vink notation this reaction is given as



where two hydroxide ions substitute for oxide ions, i.e., two positively charged protonic defects (OH<sub>o</sub><sup>•</sup>) are formed. The charged defects can diffuse into the bulk of the oxide only when accompanied by the counter diffusion of oxide ion vacancies (V<sub>o</sub><sup>••</sup>) [59]. This implies that oxides show some oxide ion conductivity in the dry state and an affinity for chemical diffusion for water (ambipolar diffusion of V<sub>o</sub><sup>••</sup> and OH<sub>o</sub><sup>•</sup>) [60]. It should also be mentioned that, apart from oxide ion vacancies existing at low-water partial pressures, the appearance of holes (h<sup>•</sup>) has to be considered at high-oxygen activities. By assuming the ideal behaviour of all species involved in the hydration reaction, and with a single standard chemical potential for each quasi chemical species the equilibrium condition is then written as

$$K = \frac{[OH_o^\bullet]^2}{([V_o^{\bullet\bullet}][O_o^x]P_{H_2O})} \quad (3.23)$$

where  $kT \ln K = T\Delta S^\circ - \Delta H^\circ$ . Because a water molecule is eventually split into a hydroxide ion and a proton, the formation reaction for protonic defects may also be considered an amphoteric reaction. Norby et al. [61] determines the enthalpy of this reaction using the structural and chemical parameters to confirm that the enthalpy of the hydration reaction tends to become more exothermic with decreasing electronegativity of the cations interacting with the lattice oxygen.

### 3.5 Kinetic consideration on electrode/electrolyte interfaces

The electrical performance of the total device is based on the manufacturing of appropriate junctions whereas both ions and electrons have to be taken into consideration. It is therefore of both fundamental and practical interest with respect to the systems performance to understand the phenomena dominating that region since the kinetics of the whole device may be dependent on the interfacial equilibrium. In the following sections the fundamental aspects on equilibrium at the electrode-electrolyte interface for both polymer and ceramic based sensor systems will be analysed.

#### 3.5.1 Metal-Polymer interface

Electrostatic potential drops occur only at the interfaces between the polymer electrolyte and the Pt electrodes in the case of emf measurements since all materials are good electrical (ionic or electronic) conductors. Only for driving electrical currents across the galvanic cell, commonly small additional electrical fields are observed within the electrolyte and across the interfaces (Ohmic bulk and interfacial polarizations). The electrostatic potential drops occurring at the interfaces are the result of the equilibration of all mobile charge carriers [62].

Figure 3.7 shows schematically the chemical potential, electrostatic potential and electrochemical potential of both electrons and protons across the Pt electrode | polymer-membrane interface and within the polymer membrane. The fluxes of the protons and electrons by diffusion ( $j_D$ ) are compensated by fluxes in the electrical field ( $j_E$ ) generated by the displacement of the charge carriers, i.e., in the case of ideal behaviour:

$$j_{D,H^+} + j_{E,H^+} = -D_{H^+} \frac{\partial c_{H^+}}{\partial x} - \frac{\sigma_{H^+}}{q} \frac{\partial \varphi}{\partial x} = 0 \quad (3.24)$$

$$j_{D,e^-} + j_{E,e^-} = -D_{e^-} \frac{\partial c_{e^-}}{\partial x} - \frac{\sigma_i}{q} \frac{\partial \varphi}{\partial x} = 0 \quad (3.25)$$

where  $D$ ,  $c$ ,  $\sigma$ ,  $q$  and  $\phi$  are the diffusivity, concentration, electrical conductivity, elementary charge and electrostatic potential, respectively.

Considering that the electrical conductivity may be expressed by the product of the concentration and diffusion coefficient [63]

$$\sigma_i = \frac{c_i D_i z_i^2 q^2}{kT} \quad (3.26)$$

where  $z_i$ ,  $k$  and  $T$  are the charge number of species  $i$ , Boltzmann's constant and absolute temperature, respectively, eqns. (3.24) and (3.25) result in

$$\frac{\partial \phi}{\partial x} = -\frac{kT}{q} \frac{\partial \ln c_{H^+}}{\partial x} = \frac{kT}{q} \frac{\partial \ln c_{e^-}}{\partial x} \quad (3.27)$$

In the case of non-ideal behaviour, the chemical potential gradient  $\partial\mu/\partial x$  has to be considered as driving force, which results in the general formula:

$$\frac{\partial \phi}{\partial x} = -\frac{1}{q} \frac{\partial \mu_{H^+}}{\partial x} = \frac{1}{q} \frac{\partial \mu_{e^-}}{\partial x} \quad (3.28)$$

Accordingly, equal magnitudes of chemical potential gradients of protons and electrons are established across the interface. An increased hydrogen concentration in the gas phase results in increased proton and electron concentration in the electrolyte and electrode. This is most noticeable in the phase in which the species are minority charge carriers, i.e. protons in the metallic conducting Pt and electrons in the proton conducting electrolyte.

There are two general models of pathways for the protons to reach the electrolyte-electrode interface after they are initially generated from the  $H_2$  molecule at the Pt surface exposed to the gas by spending two electrons to the metal electrode. This is schematically shown in figure 3.8.

The dissociative adsorption rate of hydrogen at the platinum surface is determined by the initial sticking coefficient [64], and the probability of molecules/atoms hitting the surface and becoming bound to the surface. Adsorption of hydrogen occurs favourably at Pt surfaces which have a high density of d-electron states, i.e., the sticking coefficient of the (111) Pt surface is close to 1, and there is no energy barrier for the dissociative adsorption of hydrogen. The surface diffusion and the incorporation of hydrogen into Pt are fast. Eventually, with increasing hydrogen gas partial pressure the surface area or the number of adsorption sites may become rate limiting for the adsorption of species.

If hydrogen is sufficiently rapidly dissolved and mobile in the platinum, both protons and electrons diffuse to the electrolyte/electrode interface and equilibrium is



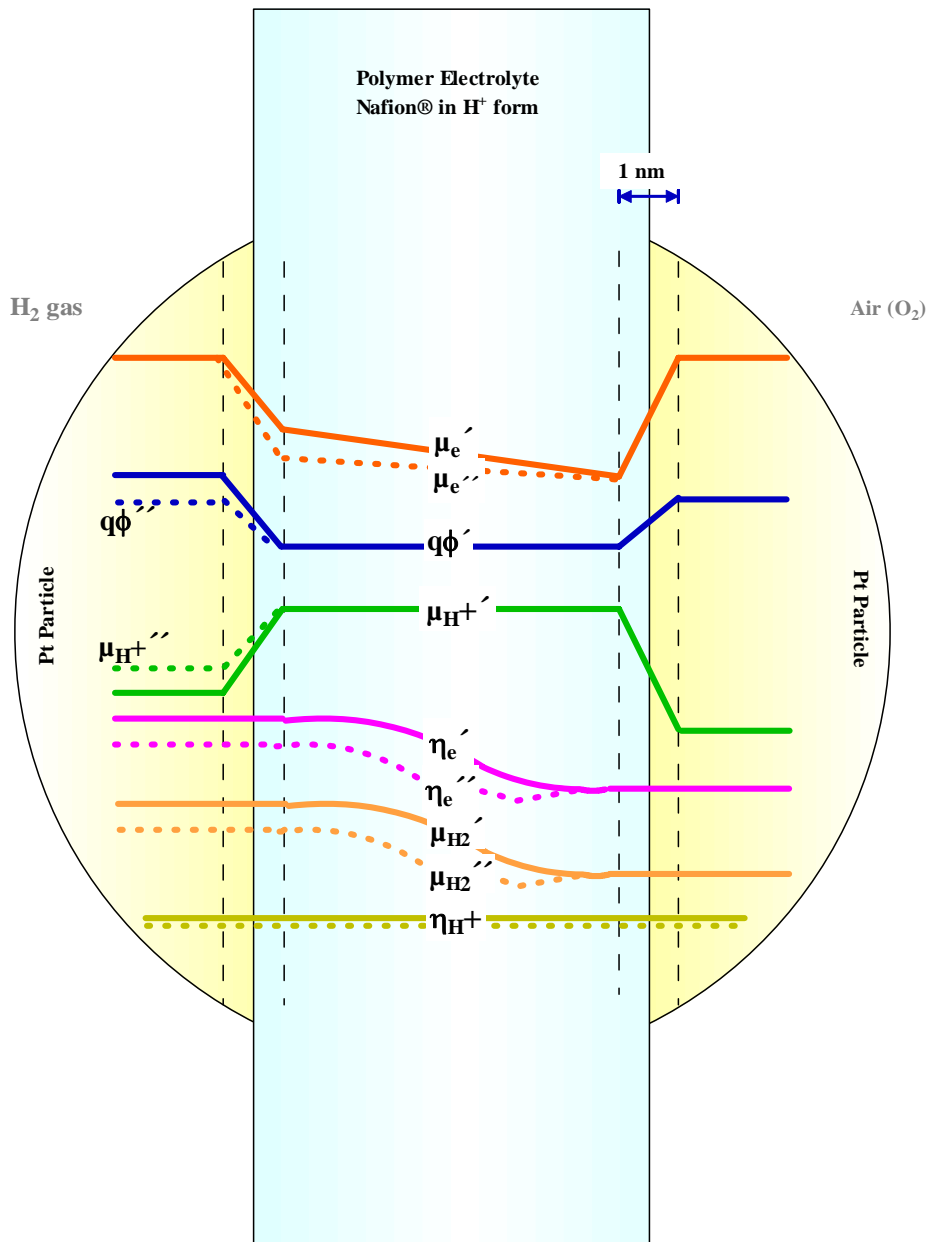


Figure 3.7: Schematic diagram of the chemical potentials of hydrogen, protons and electrons, electrostatic potential and electrochemical potential drop of both electron and proton concentrations along the Pt electrode/polymer membrane interface and within the polymer membrane. (solid line ( \_\_\_ ) represents higher  $P_{H_2}$ ; dotted line (-----) lower  $P_{H_2}$  ).

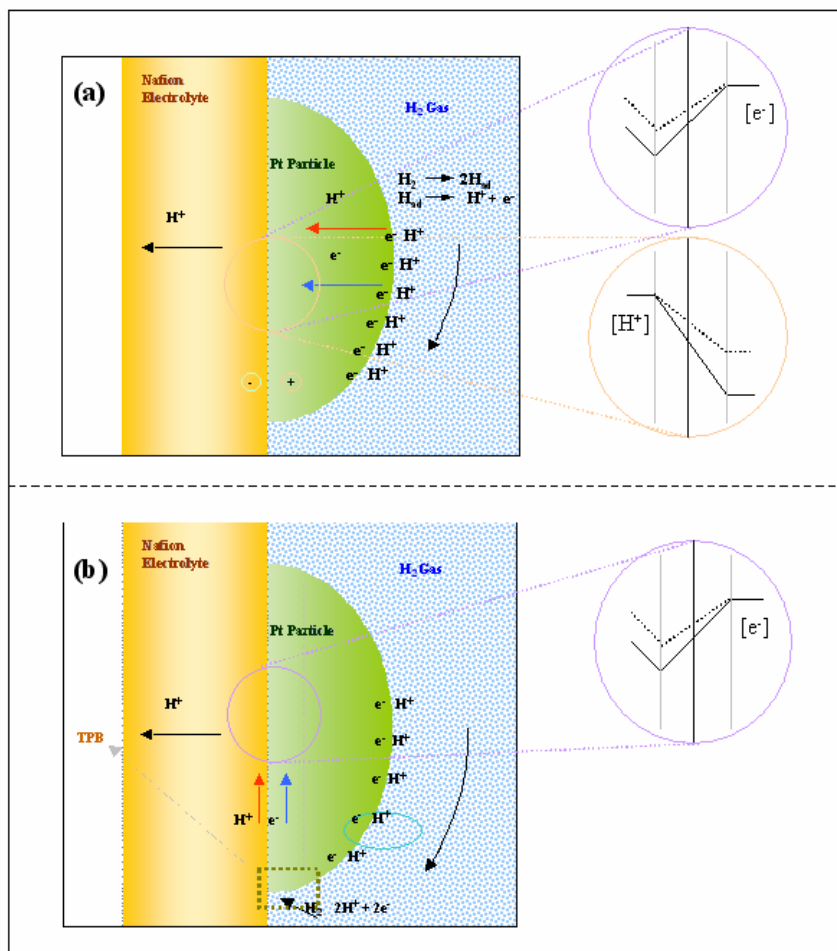


Figure 3.8: Schematic diagram of the process to build up an electrostatic potential drop across the Pt|Nafion interface. The proposed charge diffusion mechanisms are in (a) Bulk diffusion; (b) interface diffusion.

achieved when the chemical potential of neutral hydrogen is the same at the electrolyte and the platinum electrode side of the interface. It may happen, however, as this is commonly observed for Pt electrodes on oxide ion conductors, that the solubility and transport rate of the mobile ions, i.e., oxide ions, are slow in the bulk of the electrode and the ions diffuse along the Pt surface to the electrolyte-electrode-gas

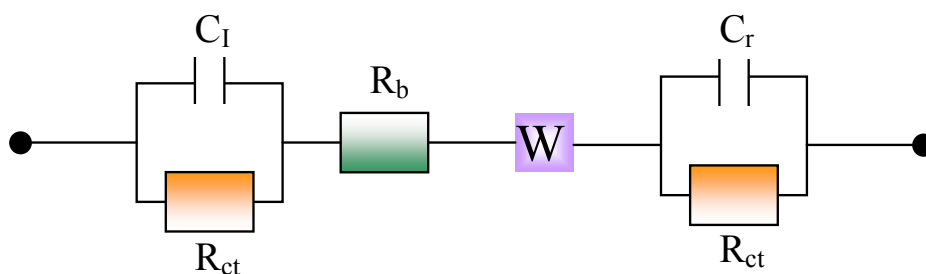


Figure 3.9: Equivalent circuit of a single Pt particle electrode on polymer membrane cell model.

triple-phase boundary (TPB). This generates a driving force for the ions and electrons along the electrolyte-electrode interface by chemical diffusion [65]. The electrons may move rapidly in the metallic conducting Pt while the ions are moving in the electrolyte. The concentration change of the ions results in an equivalent change of the concentration of electrons in the electrolyte and the electrostatic potential drop across the interface will be adjusted accordingly. The galvanic cell voltage is in this case only determined by the equilibration of electrons across the interface. The device may be considered to be a common electronic junction with the only difference that the concentration of the electrons is variable with the outside  $H_2$  partial pressure at one side (i.e., in the electrolyte) of the junction. This mechanism was described initially for noble metals in contact with ceramic oxide ion conductors for  $O_2$  partial pressure measurements [65].

The equivalent circuit of the diffusional transport mechanism of protons to the Pt-electrolyte interface is shown in figure 3.9. The circuit components  $R_{ct}$ ,  $R_b$ ,  $C_I$  and  $C_r$  correspond to the resistance of the charge transfer reaction between the Pt electrode (anode) and electrolyte interface, the ionic resistance of the electrolyte, the new double layer capacitances at the left and right hand electrode interface upon change of  $P_{H_2}$ , and the capacitance of the double layer at the air reference side (cathode), respectively. The gas diffusion in the electrode may be represented by a Warburg (W) type diffusion based on the resistor  $R_{ct}$  and capacitor  $C_I$ .

It is possible that the latter mechanism also holds in the presently employed

galvanic cells because of the low operating temperature and the comparatively fast H<sup>+</sup> motion along the Pt surface. The chemical diffusion is in contrast to the bulk of electrolytes - not controlled by the simultaneous motion of slow electrons but by the mobility of the ions in the electrolyte since electrons may move in the metal along the interface for fast compensation of electrical charges.

In the case of electrical currents, the ions are transported through the electrolyte along the cluster network formed by hydrophilic “nano-channels”. When the protons reach the opposite cathode-electrolyte interface, a reverse protonic and electronic process occurs which results in the reaction of the proton with oxygen from air to form H<sub>2</sub>O molecules. These water molecules partially diffuse into the electrolyte and maintain the required humidity in the membrane.

### References to chapter 3

- [1] S. Litster and G. McLean, *J. Power Sources* **130**, 61–76 (2004)
- [2] H.W. Bay, K.F. Blurton, J.M. Sedlak and A.M. Valentine, *Anal. Chem.* **46**, 1837-1839 (1974)
- [3] *Lange's Handbook of Chemistry*, 13th ed. McGraw-Hill, New York, Chap. 9 (1985)
- [4] M.S. Hossain, D. Tryk and E. Yeager, *Electrochim. Acta* **34**, 1733-1737 (1989)
- [5] C.A. Cavalca, J.H. Arps and M. Murthy, US Pat. No. 6,300,000 (2001)
- [6] S.Y. Cha and W.M. Lee, *J. electrochem. Soc.* **146**, 4055-4060 (1999)
- [7] R. O'Hayre, S.J. Lee, S.W. Cha and F.B. Prinz, *J. Power Sources* **109**, 483-493 (2002)
- [8] E.A. Ticianelli, C.R. Derouin, A. Redondo and S. Srinivasan, *J. electrochem. Soc.* **135**, 2209-2214 (1988)
- [9] O. Murphy, *J. Power Sources* **47**, 353-368 (1994)
- [10] S. Lee, *Electrochim. Acta* **43**, 3693-3701 (1998)
- [11] E. Gulzow, *J. Power Sources* **86**, 352-362 (2000)
- [12] V.A. Paganin, E. A. Ticianelli and E. R. Gonzalez, *J. Appl. Electrochem.* **26**, 297-304 (1996)
- [13] M. Wilson, US 5234777 (1993)
- [14] M.S. Wilson and S. Gottesfeld, *J. Appl. Electrochem.* **22**, 1-7 (1992)
- [15] H. Takenaka, E. Torikai, Y. Kawami and N. Wakabayashi, *Int. J. Hydrogen Energy* **7**, 397-403 (1982)
- [16] P. Millet, F. Andolfatto and R. Durand, *J. Appl. Electrochem.* **25**, 233-239 (1995)

- [17] P. Millet, R. Durand, E. Dartyge, G. Tourillon and A. Fontaine, *J. Electrochem. Soc.* **140**, 1373-1380 (1993)
- [18] Z. Ogumi, K. Inatomi, J.T. Hinatsu, and Z.I. Takehara, *Electrochim. Acta* **37**, 1295-1299 (1992)
- [19] S.J. Gentry and T.A. Jones, *Sens. Actuators* **10**, 141-163 (1986)
- [20] D. Kohl, *Sens. Actuators B* **18**, 71–113 (1989)
- [21] D.Kohl, *Sens. Actuators B* **1**, 158-165 (1990)
- [22] F.A. Lewis, Academic Press, New York (1967) pp 153-184
- [23] G.A. Somorjai, “Principles of surface chemistry”, Chapter 5. Prentice-Hall, Englewood Cliffs. NJ (1972)
- [24] I. Lundström, *Sens. Actuators* **1**, 403-426 (1981)
- [25] H.J.R. Magnet, in: C. Berger (Ed.), “Handbook of Fuel Cell Technology” Prentice-Hall, Englewood Cliffs, NJ (1968)
- [26] S. Motupally, A.J. Becker and J.W. Weidner, *J. Electrochem. Soc.* **147**, 3171–3177 (2000)
- [27] T.D. Gierke, W.Y. Hsu, in: A. Eisenberg, H.L. Yeager (Eds.), “Perfluorinated Ionomer Membranes”, ACS Symposium Series No. 180, American Chemical Society, Washington, DC (1982)
- [28] S. J. Paddison and R. Paul, *Phys. Chem. Chem. Phys.* **4**, 1158-1163 (2002)
- [29] P. Choi, N.H. Jalani and R.Datta, *J. Electrochemical Soc.* **152**, E123-E130 (2005)
- [30] E. Spohr, P. Commer, and A. A. Kornyshev, *J. Phys. Chem. B*, **106**, 10560-10569 (2002)
- [31] M. Eikerling, A. A. Kornyshev, A. M. Kuznetsov, J. Ulstrup, and S. Walbran, *J.Phys. Chem. B* **105**, 3646-3662 (2001)
- [32] G. Prentice, “Electrochemical Engineering Principles”, Prentice-Hall, Inc., Englewood Cliffs, NJ (1991)
- [33] J. O’M. Bockris and A. K. N. Reddy, “Modern Electrochemistry-1 Ionics”, Plenum Press, New York (1998)
- [34] T. Thampan, S. Malhotra, H. Tang, and R. Datta, *J. Electrochem. Soc.* **147**, 3242-3250 (2000)
- [35] K. S. Spiegler, *Trans. Faraday Soc.* **54**, 1408-1419 (1958)
- [36] E. H. Cwirko and R. G. Carbonell, *J. Membr. Sci.* **67**, 227-247 (1992)
- [37] P. Choi, N. H. Jalani, and R. Datta, *J. Electrochem. Soc.* **152**, E84-E89 (2005)
- [38] R. B. Bird, W. E. Stewart, and E. N. Lightfoot, “Transport Phenomena”, 2nd ed., John Wiley & Sons, Inc., New York (2002)
- [39] P. Choi, N.H. Jalani and R.Datta, *J. Electrochem Soc.* **152**, E123-E130 (2005)

- [40] K.S. Aleksandrov, *Crystallography Reports* **40**, 251-272 (1995)
- [41] K.S. Aleksandrov and B.V. Beznosikov, *Crystallography Reports* **42**, 613-623 (1997)
- [42] J. Gopalakrishnan, T. Sivakumar, V. Thangadurai and G.N. Subbanna, *Inorg. Chemi.* **38**, 2802-2806 (1999)
- [43] M. Dion, M. Ganne and M. Tournoux, *Mater. Res. Bull.* **16**, 1429-1435 (1981)
- [44] K. Toda and M. Sato, *J. Mater. Chem.* **6**, 1067-1071 (1996)
- [45] J. Gopalakrishnan, S. Uma and V. Bhat, *Chem. Mater.* **5**, 132-136 (1993)
- [46] J. Gopalakrishnan, S. Uma, N.Y. Vasanthacharya and G.N. Subbanna, *J. Am. Chem. Soc.* **117**, 2353-2354 (1995)
- [47] V. Thangadurai, A.K. Shukla and J. Gopalakrishnan, *J. Solid State Ionics* **73**, 9-14 (1994)
- [48] V. Thangadurai, A.K. Shukla, J. Gopalakrishnan, O. Joubert, L. Brohan and M. Tournoux, *Mater. Sci. Forum* **965**, 321-323 (2000)
- [49] R.E. Schaak and T.E. Mallouk, *J. Am. Chem. Soc.* **122**, 2798-2803 (2000)
- [50] B.L. Cushing and J.B. Wiley, *Mater. Res. Bull.* **34**, 271-284 (1999)
- [51] A.J. Jacobson, J.W. Johnson and J.T. Lewandowski, *Inorg. Chemi.* **24**, 3727-3729 (1985)
- [52] M. Sato, T. Jin, K. Uematsu, *J. Solid State Chemi.* **102**, 557-561 (1993)
- [53] G. Mangamma and S.V. Bhat, *Solid State Ionics* **35**, 123-125 (1989)
- [54] M. Sato, J. Abo, T. Jin and M. Ohta, *Solid State Ionics* **51**, 85-89 (1992)
- [55] K. Toda, T. Teranishi, M. Takahashi, Z.G. Ye and M. Sato, *Solid State Ionics* **115**, 501-508 (1998)
- [56] A.R. Armstrong and P.A. Anderson, *Inorg. Chem.* **33**, 4366-4369 (1994)
- [57] Y.S. Hong, C.H. Han and K. Kim, *J. Solid State Chem.* **158**, 290-298 (2001)
- [58] S. Stotz and C. Wagner, *Ber. Bunsen-Ges. Phys. Chem.* **70**, 781-787 (1966)
- [59] T. Takahashi and H. Iwahara, *Rev. Chim. Mine'r.* **t17**, 243-249 (1980)
- [60] F. Shimojo, K. Hoshino and H. Okazaki, *J. Phys. Soc. Jpn.* **66**, 8-10 (1997)
- [61] Y. Larring and T. Norby, *Solid State Ionics* **77**, 147-51 (1995)
- [62] W. Weppner, *Ionics* **9**, 444-464 (2003)
- [63] H. Rickert, "Electrochemistry of solids", Springer-Verlag, Berlin Heidelberg New York, (1982)
- [64] K. Christmann, *Surf. Sci. Rep.* **9**, 1-12 (1988)
- [65] E.D. Tsagaraki and W. Weppner, Proceedings - Electrochemical Society (Solid-State Ionic Devices II: Ceramic Sensors) (2001)

---

## Chapter 4

### Experimental aspects

This chapter describes the experimental details for the preparation of the electrode and solid proton conductor electrolyte materials. The structural and electrical characterisation techniques are described with experimental parameters utilised in this work.

#### *4.1 Electrode preparations*

In the following section, the preparation conditions of electro-catalytically active electrodes for hydrogen sensing are described. It is mainly divided into two parts: thick and thin film methods of preparation. The electrode syntheses on layered perovskite D-J phases are given briefly.

##### *4.1.1 Thick layer electrode*

Different preparation methods were chosen in order to obtain electro-catalytic active surface morphologies. The reductive precipitation of noble Pt metal on a carbon support was performed (i) in aqueous solution and (ii) from commercial products. Carbon black (Lancaster, England) with a nominal specific surface area of 320 m<sup>2</sup>/g was used as support for all catalysts. Two different electroless reduction methods [1] in aqueous phase were applied for the synthesis of Pt/C catalysts, differing in reaction time, pH and temperature. In this work, until otherwise mentioned distilled water used in the experiments was purified to resistivity of 0.005 μs/cm by filtration through a Seralpur Pro 90CN water system.

##### *4.1.1.1 Catalyst synthesis using formaldehyde as reducing agent*

An aqueous solution of 0.015 M hexachloroplatinic acid [H<sub>2</sub>PtCl<sub>6</sub> × 6H<sub>2</sub>O] (Alfa Aesar) was added drop wise to a magnetically stirred suspension of 0.5 g carbon black in 100 ml distilled water at room temperature. While the mixture was heated to 75 °C, sodium hydroxide NaOH (Alfa Aesar) pellets were added, until a pH of 8–9 was reached. After slow addition of 0.5 ml of formaldehyde (37 wt % in water), the suspension was filtered and rinsed with hot water, several times. The resulting Pt/C catalyst was dried at 100 °C in a vacuum drying oven for 6 hours.

##### *4.1.1.2 Catalyst synthesis using hydrazine as reducing agent*

An amount of 0.5 g carbon black was suspended in 100 ml distilled water and heated

to 75 °C. An aqueous solution of 0.015 M hexachloroplatinic acid [ $\text{H}_2\text{PtCl}_6 \times 6\text{H}_2\text{O}$ ] neutralized with an appropriate amount of sodium carbonate [ $\text{Na}_2\text{CO}_3$ ] powder to yield a pH value of 9, was added to the suspension within 10 min and refluxed for two hours. After addition of 0.5 ml hydrazine, the mixture was refluxed for 30 min, filtered and washed repeatedly with hot distilled water. The resulting Pt/C catalyst was air-dried at 100 °C in a dryer oven for 6 hours.

#### *4.1.1.3 Catalyst synthesis using alkali borohydrides as reducing agent*

Initially, the reducing agent of 1 M - 0.1 M sodium tetrahydridoborate [ $\text{NaBH}_4$ ] (97+ %, Alfa Aesar) was prepared in different concentrations. An amount of 0.5 g carbon black was suspended in about 100 ml distilled water and heated to 75 °C. After drop wise addition of 0.015 M hexachloroplatinic acid the solution was constantly stirred. The slurry was stirred for 30 min, then 5 ml reducing agent was added and the solution was filtered after an hour. The resulting catalyst was washed with distilled water several times and then dried at 100 °C in vacuum atmosphere.

Similarly Pt/C metal catalyst was synthesized from tetra ammine platinum (II) chloride [ $\text{Pt}(\text{NH}_3)_4\text{Cl}_6 \cdot \text{H}_2\text{O}$ ] complex salt under the same condition. Alternatively, different alkali based reducing agents was used to optimize the electrode based on their electrochemical performances. All catalyst synthesis were repeated several times with reproducible results for the structural and electrochemical characterisation.

#### *4.1.2 Slurry paste brush method*

The following section gives the preparation of thick-film electrode with the supported catalysts. Typically, gas diffusion layers are constructed on porous carbon cloth, with a thickness of 100-300  $\mu\text{m}$ . This layer adjoins on top of carbon cloth and provides a hydrophobic distribution network for the gases. Thus, gas diffusion layers with Teflon coated layer provides hygroscopic surface, to ensure that the pores of the carbon cloth does not block with water. In this work, the referred carbon cloth was commercially purchased (QuinTech, Goppingen, Germany) as a large sheet mat and cut into 15 mm diameter circular discs.

##### *4.1.2.1 Synthesised catalyst electrode*

The synthesised Pt/C powders from the three different methods were used as carbon supported catalyst material. A mixture containing 80 mg of Pt/C powder, 0.02 ml of Teflon solution (Aldrich Chemicals), and 0.5 ml of distilled water was ultrasonically blended in a glass beaker for 10 min to obtain thick catalyst ink. A volume of 100  $\mu\text{l}$



of this thick paint was spread on the surface of an uncoated carbon cloth, i.e., unTeflonized side, using a micropipette and dried in a vacuum oven at 125 °C for about 20 min to obtain a thick active layer. To obtain reproducible results using this sensitive technique, it is important to maintain a constant Pt/C powder loading on the carbon cloth surface. Hence, it is important to note that the paint should be made very uniform by extensive ultrasonic blending and the volumetric withdrawals of this viscous paint using micropipette must be constant. To confirm the reproducibility of the results, more than four electrodes as a minimum, were prepared and tested for each catalyst.

#### *4.1.2.2 Commercial catalyst electrode*

A catalyst ink was prepared from a commercial Nafion solution (5 w/o % solution from Fumatech GmbH, Ingbert/ Saar, Germany) and from 20 wt % platinum on carbon (Aldrich) combined with glycerol and water and then thoroughly mixed by ultrasound bath. The addition of glycerol and water results in a mixture that is relatively viscous and holds the carbon particles in suspension and minimizes their agglomeration once the ink is extensively ultrasonicated. The ink does not readily dry out or segregate, and it is easily painted onto a surface in a thick coat. When the applied layer is baked at about 125 °C, under vacuum the mixture provides a very uniform film. The similar procedures were applied to prepare Pd/C catalyst by using  $\text{Pd}(\text{NH}_3)_4\text{Cl}_6 \cdot 6\text{H}_2\text{O}$  and  $\text{NaBH}_4$  metal complex. The product yield obtained from Pd compound was less than the Pt compound.

#### *4.2 Preparation of the membrane electrode assembly (MEA)*

MEA with an active electrode area of 1.76 cm<sup>2</sup> per electrode were manufactured. Commercially available Nafion either in the form of sheet or solution were applied as proton conducting membrane and in all cases membrane of 2 cm<sup>2</sup> area was chosen per assembly. A standard 55 mg of Pt/C powder containing Vulcan XC-72 catalyst was used at both cathode and anode sides. The schematic representations of gas diffusion electrode MEA process are shown in figure 4.1.

##### *4.2.1 Preparation of MEA using Nafion film*

A sheet of Nafion membrane of an appropriate size was ion-exchanged as discussed in membrane pre-treatment section 4.4.1.1. Then, the membrane was rinsed with double distilled water, fixed to a specially designed Teflon table. The catalyst ink was prepared by mixing 55 mg catalyst powder, 20 µl Nafion solution, 60 µl distilled

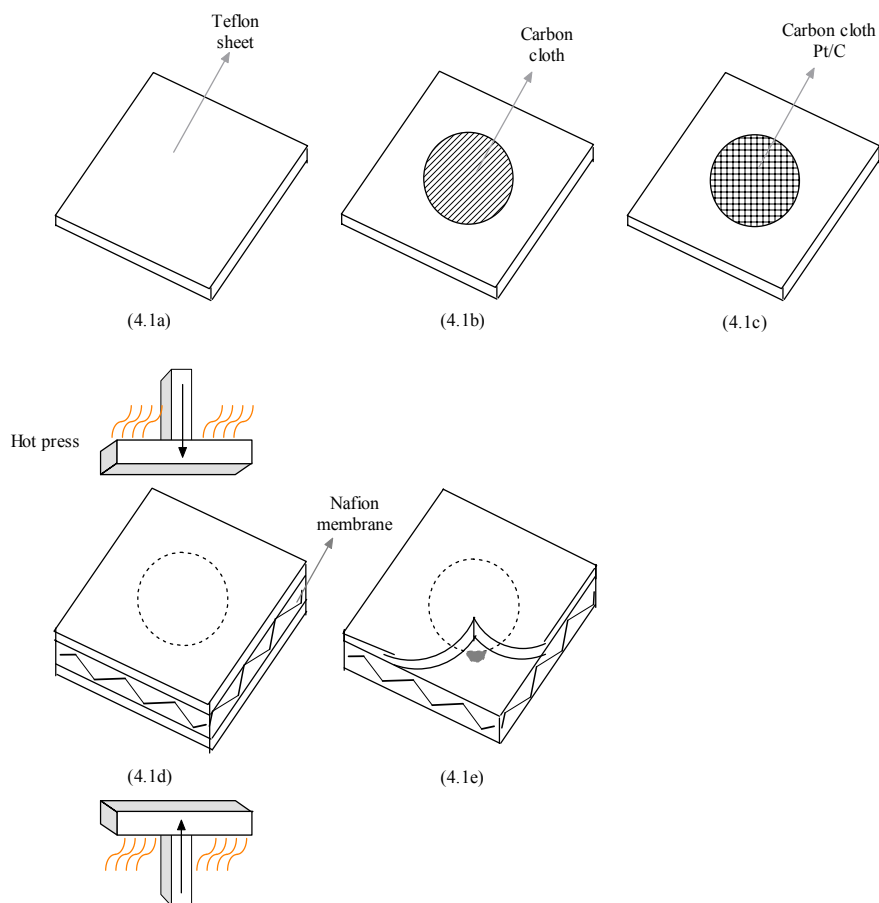


Figure 4.1: Primary steps in the fabrication of a thick layer catalyst bonded to an ionomeric membrane.

water, and 20  $\mu\text{l}$  glycerol in an ultrasonic bath. The obtained homogeneous suspension was successively brushed in several thin layers on the membrane surface, allowing each complete layer to dry for 2 min. After one electrode had been manufactured in this way, the membrane was soaked into distilled water for 30 min to rejuvenate its optimum water content. Then, the other electrode was prepared in the same way. Finally, the obtained MEA was heated to 120  $^{\circ}\text{C}$  for 1 hour to remove remains of the solvents, and ion-exchanged in 1 M  $\text{H}_2\text{SO}_4$  for at least 3 hours. The preparation process was completed by boiling the already prepared MEA in double distilled water for a minimum of 2 hours.

#### 4.2.2 Preparation of MEA using Nafion solution

A measured volume of 1 ml Nafion solution (5 wt %) was taken in glass discs and diluted from isopropanol solution to brushable consistence. The prepared supported catalyst electrode was rinsed with double distilled water, fixed to a specially designed Teflon table. The membrane solution was poured on top of catalyst layer and the second catalyst electrode was placed on top of the membrane solution. Then, the assembly was covered with a circular cylindrical Teflon block on top, to form a good interfacial electrode contact with cased film and allowed to dry for 8 hours. Figure 4.2 shows the schematic representation of composite of carbon, Pt particles, and Nafion solution in MEA. The preparation process was completed by boiling the assembled MEA in double distilled water for a minimum of 2 hours.

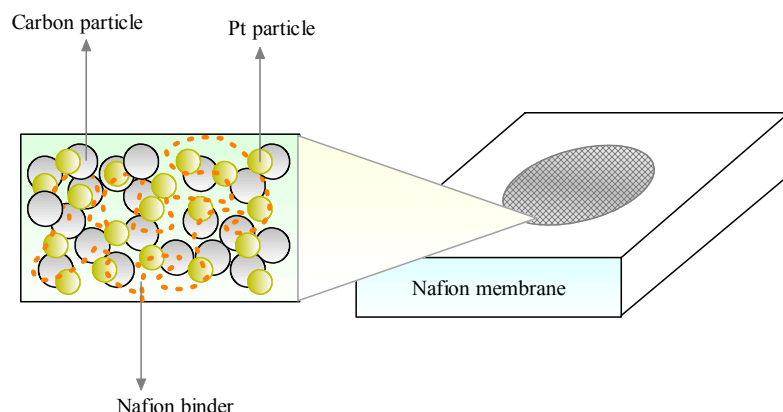


Figure 4.2: Representation of a continuous three-phase interface (carbon, catalyst and Nafion).

The following is a summary of preparation protocol:

1. Mix solution of Nafion and 20 wt% Pt on carbon. A weight ratio of 1:5 for the catalyst supported Pt/C is preferable.
2. Add water and glycerol such that its weight ratios are approximately 5:1:2 for catalyst/water/glycerol+binder.
3. Mix and ultrasound extensively. Although the mixture is initially not uniformly viscous, it will eventually thicken. If alcohols from the Nafion solution are allowed to stay in the mixture, the ink will dry more quickly in the oven.

4. Clean thoroughly a blank of carbon cloth (figure 4.1a) and coat with a thin layer of Teflon solution. Paint the ink on a blank layer by layer (figure 4.1b) and bake in a vacuum oven at 120 °C (figure 4.1c) until dry. If necessary, additional layers can be added to achieve the desired catalyst loading, although it is desirable to minimize the overall baking time.
5. Use silicon rubber sheet to cover the coated blank, a polymer electrolyte membrane, and counter electrodes in order to keep all component in aligned manner, and hot-press together in a conventional manner (figure 4.1d) of temperature about 120 °C and apply light force until the press heats up to 130 °C for 2 min. The schematic diagram of indigenously designed hot press mount is as shown in figure 4.3.
6. Remove the membrane/catalyst assembly from the press and allow to cool, and then the silicon sheet can be peeled away from the assembly, check catalyst film adhesion with the membrane (figure 4.1e) before storage.
7. In few cases, an uncatalyzed Teflon-bound electrode (Fumatech GmbH, Ingbert/ Saar, Germany) is used as gas diffusion barrier for the thick film catalyst layer, i.e., no hot press or other gluing was done.

### *4.3 Thin layer electrode*

This section deals with experimental procedures and synthesis conditions used for thin layer of metal catalyst prepared by using sputter and electroless coating. The thickness of each thin film was measured by surface Profilometer (Dektak 8000).

#### *4.3.1 Sputter deposition*

Sputtering is a physical vapour deposition process that employs plasma to generate energetic species that bombards target material, knocking its atoms/molecules to free. Atoms from the target accumulate on the surrounding surfaces, forms a thin layer of the target material. The plasma generation was achieved by igniting a low-pressure gas in an electric field. The sputter deposition process used a Pt metallic target with an AC voltage of 13.56 Hz to generate the plasma [2]. To decrease the electron bombardment of the substrate and increase ionization in the plasma, a magnetic field is applied to the plasma, usually with permanent magnets located behind the target. Trapping the electrons near the target, this method is known as magnetron RF sputtering [3].

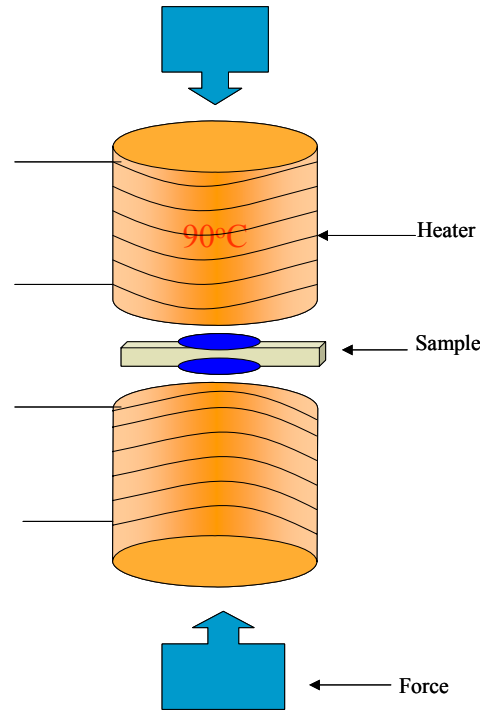


Figure 4.3: Hot press setup.

Solid polymer (Nafion) membrane electrolyte and layered perovskite (niobate and tantalate) ceramic electrolyte were used as substrates for sputter deposition. A thin film of electrode deposition was carried out by RF magnetron (Alcatel 450, France) sputter coating tool Ruthenium alloyed Pt target. A specially made sample stage was used to support Nafion membrane substrate of size 2x2 cm while masking diameter of 1.6 cm about the membrane's perimeter. All electrode depositions were completed at a pressure of  $10^{-2}$  mbar in argon atmosphere at the power of 150 Watt for 5 min. The vacuum chamber was used to evacuate each substrate to a pressure of  $10^{-6}$  mbar, before sputtering.

#### 4.3.2 Electroless deposition

This section gives an overview of deposition steps and conditions of Pt metal on both solid polymer and ceramic electrolytes. In literatures [4,5] several methods were proposed by different groups to plate adequate catalytic structures on both sides of the electrolyte surfaces. Electroless is the simple and cost effective method which deposit Pt particles without the use of binders. In order to deposit a porous structured electrode provided with TPB regions for gas sensing purpose on solid proton

conductors T-T, I-R, and Multistep-impregnation-reduction (M-I-R) methods were applied.

In all methods, the plating of Pt metal could be deposited in pure form on to both polymer and ceramic surfaces. As reported by Takanaka et al. [6] the former two methods were applied successfully on polymer and the preparation steps of I-R was slightly modified to extend on ceramic niobates and tantalates. In general, the bath contains an aqueous solution of Platinum complex salt and various molar concentrations were prepared from ammonium hydroxide ( $\text{NH}_4\text{OH}$ ) solution. Throughout the plating process, constant temperature was maintained in both metal salt and reducing solution agent. The electrode depositions were carried out at different higher temperatures (50, 60, and 70 °C) and finally optimised to proceed at room temperature. The boiling temperature of the bath should be avoided as at higher temperatures the salt solution evaporates. An important factor influencing the plating process is pH. The pH needs to be maintained between 10-12 for plating to occur. At lower pH, no deposition was achieved.

#### *4.3.2.1 Electrode deposition by T-T method*

The Pt metal deposition was carried out on both sides of ion exchangeable proton conducting solid polymer membrane surface by T-T method. The membrane was placed in between polyacrylic holder circular flow lines with inlet and outlet. The photograph of fluid flow line is shown in figure 4.4. One surface was circulated at 1 M ( $\text{Pt}(\text{NH}_3)_4\text{Cl}_2$ ) metal salt solution and the other surface held in contact with 1 M ( $\text{NaBH}_4$ ) reducing agent solution. In this method the reducing agent solution continuously penetrates through the membrane and comes in contact with the metal

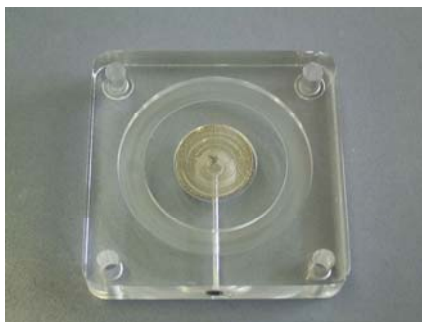


Figure 4.4: Photograph of fluid flow line.

salt solution. This procedure was continued for 2 hours maintaining constant pH of solution, ranging 10-12. After adequate deposition of metal, the membrane was washed with water to remove excess of reductant compounds and again boiled in 1 M  $\text{H}_2\text{SO}_4$  at 80 °C for 30 min.

#### 4.3.2.2 Electrode deposition by I-R method

The ionic polymer-metal electrodes were formed by employing ionic polymers which were chemically treated with an ionic salt solution of a metal complex by the (I-R) method [7].

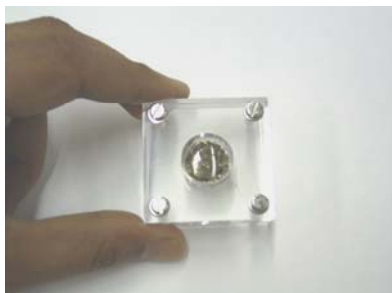


Figure 4.5: Photograph of Plexiglas holder.

Commercially available metal complexes such as tetra-ammine platinum (II) chloride ( $\text{Pt}(\text{NH}_3)_4\text{Cl}_2$ ) from Sigma Aldrich were used in aqueous concentrations of 0.001, 0.01 and 0.1 M. The membrane was stretched and fixed in a Plexiglas holder with a circular opening of 16 mm in diameter as shown in figure 4.5. The metal complex solution was exposed to the membrane for 3 hours at a fixed pH value of 11-12 maintained by the addition of ammonium hydroxide solution. Then, the membrane was rinsed 2-3 times with double distilled water. The impregnated metal ions  $[\text{Pt}(\text{NH}_3)_4]^{2+}$  were reduced by using a strong reducing agent, sodium tetrahydroborate ( $\text{NaBH}_4$ ), with concentrations from 0.004 to 0.1 M for 2 hours. The reducing solution was replaced every 20 min. Both impregnation and reduction were carried out at room temperature. Subsequently, a similar procedure was applied to the other side of the membrane in order to get the second electrode with the same thickness as the first one. Similarly the impregnated metal ions  $[\text{Pt}(\text{NH}_3)_4]^{2+}$  were reduced by using a weak reducing agent, potassium tetrahydroborate ( $\text{KBH}_4$ ), with concentrations from 0.004 to 0.1 M, under the same conditions as mentioned above.

#### 4.3.2.3 Electrode deposition by M-I-R method

The porous Pt metal electrodes were prepared by chemical treatment of the solid  $\text{KC}_2\text{Nb}_3\text{O}_{10}$  electrolyte by employing M-I-R method with an ionic salt solution of a metal complex such as 0.1 M tetra-ammine platinum (II) chloride  $[\text{Pt}(\text{NH}_3)_4\text{Cl}_2 \cdot \text{H}_2\text{O}]$ . However, the procedure for Pt deposition was modified for successful deposition on a ceramic surface. The metal complex solution was exposed to 1 cm diameter-sized

pellet for 20 min at a fixed pH value of 11-12 maintained by the addition of ammonium hydroxide solution. The impregnated metal ions  $[\text{Pt}(\text{NH}_3)_4]^{2+}$  were reduced by using a strong reducing agent, potassium tetrahydroborate ( $\text{KBH}_4$ ), with concentrations from 0.1-3 M for 20 min. The same procedures were repeated 6 times in order to get proper electronically conducting film on one side of the oxide surface. Both impregnation and reduction were carried out at room temperature. Subsequently, a similar procedure was applied to the other side of the solid electrolyte in order to get counter electrode with same thickness as the first one. The platinised solid electrolyte was washed with double distilled water.

The similar procedure was applied to deposit a porous platinum electrode on surface of the tantalates systems. Since these compounds are synthesized from soft chemistry route, they were anhydrous in nature due to the large interlayer distances. Specifically,  $\text{NaCa}_2\text{Ta}_3\text{O}_{10}$  was readily soluble in water containing solutions. In order to avoid the compound to dissolve into Pt complex salt solution the reaction times were modified. In the case of  $\text{NaCa}_2\text{Ta}_3\text{O}_{10}$ , the Pt complex solution was exposed to 11 mm diameter-sized solid pellet for 5 min and then allowed to dry for 10 min. The procedures were repeated for four times prior to the reduction step. Similarly, the reduction was carried out in the time intervals of every 5 min. The rest of the pellet surfaces were covered with easily detachable plastic glue (commercial thermo plastic adhesion glue) to protect the electric leakage between the electrodes. In the hydrogen exchanged  $\text{NaCa}_2\text{Ta}_3\text{O}_{10}$  compounds of  $\text{HCa}_2\text{Ta}_3\text{O}_{10}$ , similar steps were followed on a size of 8 mm diameter pellet faces. To improve the electrical conductivity of both tantalate samples the electrode surfaces were platinised for 3-4 times.

#### *4.4. Electrolyte preparations*

This section gives details of the solid electrolyte preparation methods, reactant chemical composition, quantity, time-temperature of sintering/curing, in addition, size and shape dimensions of both solid polymer, and ceramic niobates and tantalates.

##### *4.4.1 Polymer Electrolyte*

###### *4.4.1.1 Solid polymer membrane (SPE) pre-treatment*

Commercial Nafion membranes, provided by DuPont (Wilmington, DE, USA), were employed in the present work. A large sheet of fuel cell graded copolymer of tetrafluoroethylene (Teflon) and perfluoro-3,6-dioxa-4-methyl-7-octene-sulfonic acid, Nafion 112, Nafion 115, and Nafion 117 in a dry form. These solid polymer membranes are generally characterized by their equivalent weight and thickness.



Specifically, Nafion 117 with an equivalent dry weight of the polymer per mol sulfonic acid group of 1100 g/mol which presents a measure for the mass based concentration of the SO<sub>3</sub>H groups and a membrane thickness of 0.7 μm was used. Due to the manufacturing process, the received Nafion contains sodium ions within the exchange sites. Before performing electrochemical measurements, the sodium ions were replaced by protons and the membrane was soaked in water. This process was performed by boiling the membrane in 3% hydrogen peroxide solution and then in 1 M H<sub>2</sub>SO<sub>4</sub> for 2 hours at a temperature of 100 °C. To remove the remaining acid, the membrane was then boiled three to four times in pure de-ionized water for 30 min. The swollen membranes were stored in distilled water to prevent drying.

The solution form of 25ml Nafion (5 wt%) in alcohol was purchased from Fumatech GmbH, Ingbert/ Saar, Germany. A thin film of solid polymer membrane was casted from solution, as described in the catalyst preparation section 4.2.2 and the above mentioned protonated treatments were applied to these casted membranes.

#### 4.4.2 Ceramic Electrolyte

This section is divided into two: the synthesis of layered structure perovskite by conventional high temperature solid state sintering route and the corresponding parent compound alkali ions were exchanged to Na and H phase by soft chemistry at room/low temperatures.

##### 4.4.2.1 Solid state sintering

All the chemicals were of analytical grade. The starting material of KCa<sub>2</sub>Nb<sub>3</sub>O<sub>10</sub> was prepared as reported in the literature [8]. Reagents such as K<sub>2</sub>CO<sub>3</sub> (Aldrich), CaCO<sub>3</sub> (Merck), and Nb<sub>2</sub>O<sub>5</sub> (Aldrich) were of 99% purity or higher. Stoichiometric amounts of the carbonated and oxide were thoroughly mixed and ground by using high-speed planetary ball mill Pulverisette 5 (FRITSCH, Germany). Excess 20 wt% K<sub>2</sub>CO<sub>3</sub> was added to compensate for the loss due to volatilization. The mixture was initially calcinated at 1000 °C for 24 hours and after regrinding it was sintered at 1200 °C for an additional 24 hours in air. The temperature was controlled using a thermocouple junction placed in the centre of the furnace in close proximity to the samples. Sample temperature was assumed to be the same as furnace temperature which was measured using the control thermocouple. A programmable furnace was used to control specific heating schedules and hold times. Unless otherwise stated in this thesis, sintering was performed by heating at 2 °C/min from room temperature to 1200 °C. Samples were held at desired temperature for 24 hours. The temperature of cooling rate was controlled identically to the temperature of heating cycle.

A series of niobate compounds  $ACa_2Nb_3O_{10}$  ( $A = Rb$ , and  $Cs$ ) were prepared by the reaction stoichiometric quantities of  $CsCO_3$  (Chempur),  $CaCO_3$ , and  $Nb_2O_5$  with 99% purity at  $1000\text{ }^\circ\text{C}$  for 24 hours. In between one step grinding, excess amount of alkali carbonate was added as described in the literature [9]. The mixture was sintered in an alumina crucible with partially closed alumina lid at  $1200\text{ }^\circ\text{C}$  for 24 hours.

Similarly the  $ACa_2Ta_3O_{10}$  ( $A = Rb$ , and  $Cs$ ) stoichiometric amounts of parent tantalate compounds carbonate and oxides were thoroughly mixed and ground. The mixture was initially heated at  $1000\text{ }^\circ\text{C}$  for 12 hours and was sintered at  $1200\text{ }^\circ\text{C}$  for an additional 12 hours in air, after regrinding.

#### 4.4.3 Protonation of layered perovskites

Both layered perovskite oxides of niobate and tantalates were protonated to apply then in the hydrogen sensing cell component. The protonation of these compounds were carried out in a reducing (hydrogen) atmosphere as described in the literature [10]. The isostatically pressed pellet discs were placed in a quartz glass tube

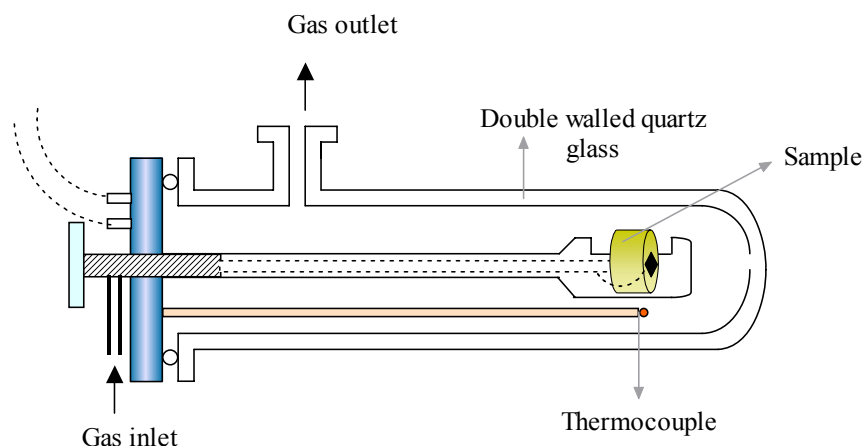


Figure 4.6: Schematic representation of the apparatus for electrochemical measurements under defined temperature and gas mixtures (“Kiel cell”).

provided with gas inlet and outlet. The schematic diagram of the quartz glass arrangements (“Kiel cell”) are shown in figure 4.6. Prior to the protonation process, the furnace chamber was purged approximately for 10 min with high pure argon. The high purity hydrogen was then flowed continuously throughout the heat-treatment cycle at a flow rate of  $0.5\text{ l/min}$ . Outlet of the chamber was passed through a bubbler filled with glycol before being sent to a fume hood. The bubbler provides a slight positive pressure inside the furnace tube and also prevents back-diffusion of air though the exhaust compartment.

#### 4.4.4 Ion exchange reaction (IER)

Ion exchange is the most common low temperature solid-state synthesis of layered perovskite. It is also called as *chime douce* or *soft chemistry*, which involves low temperature modification of existing solid structures to form a new solid that retain many of the structural features of the parent phase. Using the principles of soft chemistry, it is possible to synthesis a variety of metastable solids having structures that do not form in conventional high temperature synthesis. This section deals with the ion exchange reaction between solid-state synthesis powder and molten salt/acid bath of I-main group ions.

##### 4.4.4.1 IER of niobate

The Na and H derivatives,  $\text{NaCa}_2\text{Nb}_3\text{O}_{10}$  and  $\text{HCa}_2\text{Nb}_3\text{O}_{10}$ , with a layered perovskite structure were obtained by ion exchange of  $\text{KCa}_2\text{Nb}_3\text{O}_{10}$ . The sodium exchanged compound was prepared by ion exchanging 10 g of  $\text{KCa}_2\text{Nb}_3\text{O}_{10}$  finely ground powders in a  $\text{NaNO}_3$  melt bath at 400 °C for 24 hours. After the reaction, the product was thoroughly washed with distilled water to remove excess  $\text{NaNO}_3$ . Whereas, hydrogen exchanged compound was prepared in acid solution of 1 M  $\text{HNO}_3$  at room temperature, for a week. For comparison another set of  $\text{CsCa}_2\text{Nb}_3\text{O}_{10}$  and  $\text{RbCa}_2\text{Nb}_3\text{O}_{10}$  was ion exchanged in 1 M  $\text{HCl}$  at 40 °C for one week each.

##### 4.4.4.2 IER of tantalate

Another D-J phase  $\text{NaCa}_2\text{Ta}_3\text{O}_{10}$  was prepared by a single step ion exchange reaction between molten bath of  $\text{NaNO}_3$  (Alfa) and 60 g of  $\text{CsCa}_2\text{Ta}_3\text{O}_{10}$  powder. The reaction was carried out in an alumina crucible at 400 °C to convert into a Na phase for 2 days. The reaction was interrupted during exchange process to add an excess of  $\text{NaNO}_3$  salt by removing the crucible in every 8 hours. Subsequently, the melt was periodically stirred well in every 30 min for about 1 min. After 2 days, the solidified melt was subsequently washed with distilled water for several times to remove unreacted, excess  $\text{NaNO}_3$ . A fine and white in colour anhydrous powder of 53 g product was obtained. Since the resultant tantalate was a hydrated phase, which contains water in the interlayers, dehydration process was carried out in vacuum oven at 250 °C. The Na phase of 25 g powder was protonated with 200 ml of 1 M  $\text{HCl}$  in a round bottom glass container. The acid bath reaction was constantly stirred using magnetic pellet at room temperature for a week. The magnetic stir was interrupted and powders were allowed to sediment for an hour and the bath was refilled with acid solution for every 10 hours. The resulting 18 g solid powder was washed with

distilled water for several times and dried in air at 60 °C. The similar procedures were followed to ion exchange the layered perovskite series from the parent compound of  $\text{RbCa}_2\text{Ta}_3\text{O}_{10}$ , which was synthesized by solid-state reaction.

#### *4.4.5 Preparation of solid electrolyte circular pellet discs*

As prepared anhydrous D-J phase powders were pressed into a cylindrical shape by using isostatic force in hydraulic press. The powders were well ground, dried, and filled with cylindrical rubber mould of 40 mm length and 15 mm diameter, prior to the press. The green ceramic cylinder was covered with the same powder in alumina crucible while sintering to minimize the loss of alkali metal atoms due to volatilization. The sintered dense samples were machined into approx. 10 mm diameter pellets of each 1 mm thickness. Fairly dense pellets were obtained from the ion exchanged powders and machined into the discs in green form itself. The rough surfaces of pellets were polished with a grinding machine (Rotopol-V, Struers, Copenhagen, Denmark) using water/oil thereby lubricating the abrasive discs of different roughness down to 1  $\mu\text{m}$ .

#### *4.5 Gas sensor measurement setups*

This section deals with the experimental arrangements for the detection of hydrogen in the concentration ranges from ppm to percentage level at various temperatures.

##### *4.5.1 Gas detection test-bench setup*

A complete gas sensor test bench was established in a fixed place with the following equipments:

- Gas bottles
- Mas flow Meter/controllers
- Potentiostat
- Computer (PC)

Highly pure specific gases or gas mixtures of 50 litre large bottles were purchased commercially (Messer, Griesheim, Germany). The accurate ratios of dry gases were mixed through electrically controlled mass flow meters/controllers (Tylan General FC 280, USA). The gas flow lines were constructed with stainless steel of 3 mm diameter tubes and interconnected with metallic connectors (Swagelok, USA). Both electrochemical measurements and sensor device output signals were measured with high input impedance potentiostat PG 2.0 (Ionic Systems, Stuttgart, Germany [11]).

This device is simple and excellent in performance in both potentiostatic and galvanostatic mode provided with analog to digital interface converter. The gas sensor cell output signals were interfaced with computer via GPIB (National Instruments) card. The data were collected with regard to changes in the current and response time as a function of the hydrogen partial pressures. Sensor output signals were observed and recorded by using self programmed Labview<sup>®</sup> software and stored in a computer file for post run analysis. The schematic layout of test bench arrangements are shown in figure 4.7.

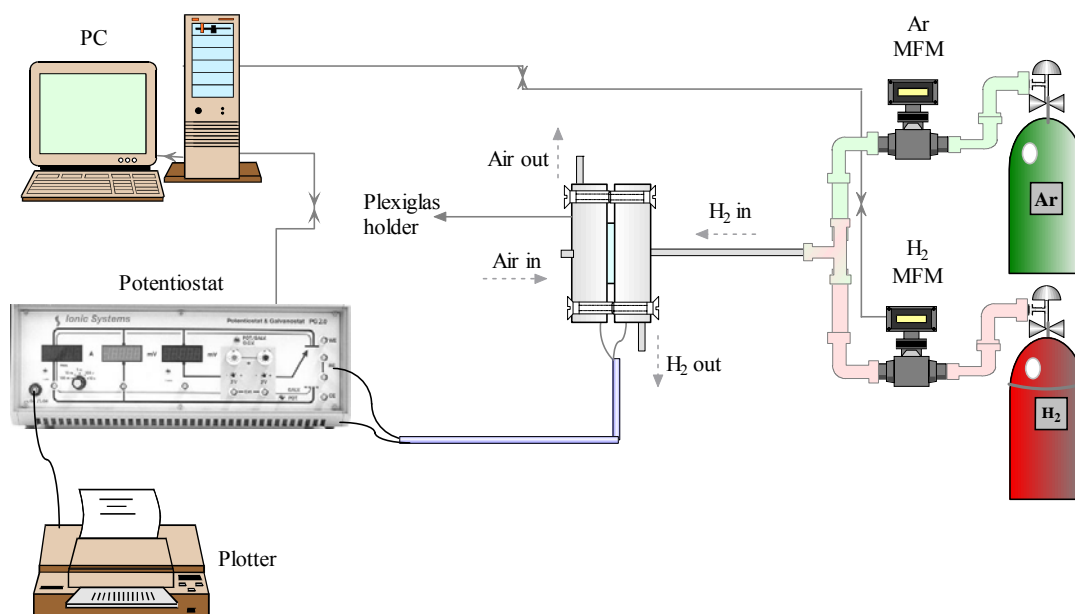


Figure 4.7: The representation of sensor test bench arrangement.

#### 4.5.2 Design of sensing device

The aim of the hydrogen gas detection principle based on amperometric method, makes the device component and its design rather simple. The preparation of the MEA was described in section 4.2. A flexible MEA of whole cell is about 3 mm in thickness and sandwiched between 10 mm thick Plexiglas holder. The inner side of the PMMA holder was integrated with circular continuous gas flow line provided an exit channel as shown in figure 4.8. The electrical lead was established with 0.3 mm diameter platinum wire grid on top of the MEA carbon electrodes. Each MEA of all types were assembled in PMMA holder with same screw tightness. The schematic

diagram of complete cell arrangement in excelled view is shown in figure 4.9. To operate the device above 30 °C, sensors were constructed with Teflon holder instead of PMMA, due to its less thermal instability.

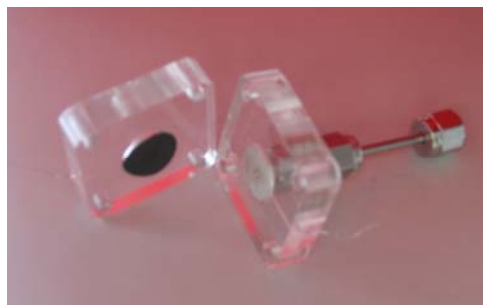


Figure 4.8: Photograph of PMMA holder.

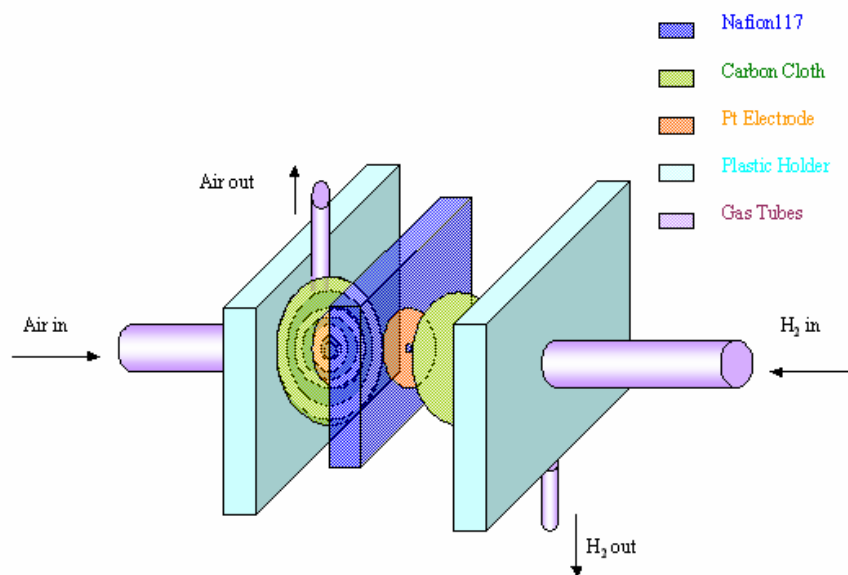


Figure 4.9: Construction of polymer based amperometric H<sub>2</sub> gas sensor cell.

#### 4.5.3 Gas Measurement in air and inert atmospheres

The leakage sensor as well as concentration monitor device was studied under the principle of short circuit amperometric method. After the cell was assembled in a holder, open circuit voltages were measured. The cell was then switched to potentiostatic mode, where the voltage was kept zero i.e., the two electrodes were shorted, in which both electrodes reach an equal chemical potential. Extensive care was taken during the constructions of the sensors, more towards the onsite applications. The sensor demands for safety largely in fuel cells industry. The amount of hydrogen gas was measured in Ar (Argon 5.0), N<sub>2</sub> (Nitrogen 5.0) gas line at anode side and the same was used as a carrier gas. Whereas, the ambient air was maintained at the cathode side. However, in some cases, air was forced to pump using mini air pump. The hydrogen and argon/nitrogen gases were mixed in an appropriate ratio to measure in ppm to percentage of hydrogen concentration. Also the hydrogen detections were measured in air (synthetic air 5.0), i.e., 90% N<sub>2</sub> and 10% O<sub>2</sub> + H<sub>2</sub>. Unless otherwise stated, the gases were purged through the mass flow meter in dry condition. In few cases, moisturiser column was placed in between the sensor and the flow meters. The entire work was studied over years, where the ambient condition varies, i.e., ambient relative humidity (RH) between 48-60 %.

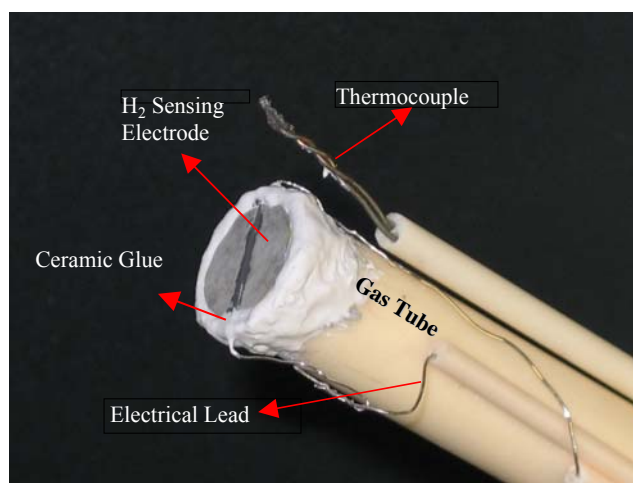


Figure 4.10: Construction of polymer based amperometric H<sub>2</sub> gas sensor cell on an alumina tube.

When the layered perovskite type niobates and tantalates were employed as a solid electrolyte, the sensor design construction was changed according to its size and stability. Most of the layered perovskite oxides pellets were obtained in a brittle form,

but sometimes even highly hygroscopic tend to volume change and subsequently cracks. With the knowledge gathered over a decades in this laboratory, it was not difficult to handle such samples. The construction of the layered perovskite oxides was carried out in a long ceramic alumina tube. The difficulty to operate the device at high temperature and controlled atmosphere were ruled out in “Kiel cell” arrangement, as shown in figure 4.6. The fabricated pellet type sensor element was sealed to one end of a ceramic tube which was equipped inside with a tube leading the gas to the sample and with electronic Pt leads. A photograph of the sensor element attached to a gas-tight ceramic tube with thermocouple and electrical leads is shown in figure 4.10.

#### *4.6 Characterization of materials*

This section deals with the characterization methods utilised to study the structure, surface morphology, core/vibrational energy spectra, and electrochemical process of the catalytic materials prepared with chemical and non-chemical route.

##### *4.6.1 X-Ray diffractometer (XRD)*

The structure of the catalysts and electrolyte samples were investigated by X-ray powder diffraction using a SEIFERT XRD 3000TT and 3000PTS, with monochromized Cu K<sub>α</sub> radiation. For preliminary investigation the materials used in this work were either in a powder or a circular pellet form. The initial position was adjusted with respect to the strongest reflection peak of silicon from time to time. Very thin film samples were characterized by GIXRD mode. All the structural studies were carried out on both Pt catalyst electrode and perovskite proton conductors at ambient temperature and atmosphere. Scans of both film and powdered samples were performed in a step-wise procedure using 0.02° 2θ steps with a 2 s hold at each position. Both, chemically prepared Pt catalyst powders and films were in a nano meter scale. Due to their small particle sizes, coherently scattering regions below a certain extension were not distinguishable from the amorphous background. Therefore, the evaluation of the X-ray patterns was mainly done to check the apparent crystallographic phases and estimate the particle size according to the *Scherrer* equation [12]

$$d = \frac{K\lambda}{\beta \cos \theta} \quad (4.1)$$

where d is the crystallite diameter, K is the Scherrer constant, λ is the wavelength of the K<sub>α</sub> radiation from the Cu target, β is the integral breadth of the peak at 2θ, i.e., β



is the FWHM (full width at half-maximum) for a Gaussian shaped peak and  $\theta$  is the Bragg angle for the peak at  $2\theta$ . The subtraction of the instrumental broadening effects could be eliminated by computing the actual line broadening  $\beta_1$  from the expression:

$$\beta_1 = (\beta^2 - b^2)^{1/2} \quad (4.2)$$

where  $b$  is the instrumental broadening, i.e. FWHM of the standard Pt sample. The respective lattice space analysis of the layered perovskite powered compound phases were determined by using the prozki package [13].

#### 4.6.2 X-ray photoelectron spectroscopy (XPS)

XPS measurements were carried out in Omicron Full Lab in UHV condition (Perkin Elmer) with  $AlK\alpha$  radiation, a hemi-spherical analyzer was used as detector. Suitable pass energy of 100 eV was applied, a pressure of  $3 \times 10^{-9}$  mbar was maintained within the spectrometer chamber. Samples were prepared by pressing a small amount of supported catalyst powder onto a carbon tape. The spectra were fitted and evaluated by standard calculation software using a mixed Gauss-Lorentzian function for the peak shapes. The binding energy shift fitting was compared with the literature values and standards.

#### 4.6.3 Fourier transform infrared (FTIR) spectrometer

FTIR studies were carried out on a continuous scan Michelson interferometer (with sealed and desiccated optics) from Nicolet 20DXB, using a thermo-electrically cooled deuterated triglycine sulphate (DTGS) detector, multi-layer germanium coated KBr beam splitter, and a dual source working in wave number ranges of 4800–400  $cm^{-1}$ . The powder samples were dried, ground in a granite mortar together with spectroscopic grad KBr granules in 1:10 wt ratio. The powder mixture of 25 mg of each sample was pressed into a 50  $\mu m$  thick and 6 mm diameter pellet. The optically transparent disc, with nearly no particle agglomeration, was placed in a specially designed stage for transmission FTIR studies. This stage was operated at room temperature in a moisture free chamber. Spectra were recorded in the wave number range of 4000–500  $cm^{-1}$  and each spectrum was an average of 100 scans and with 2  $cm^{-1}$  resolution. The size of the aperture was 3 mm diameter, and hence this area of the sample was always exposed to IR radiation.

#### 4.6.4 Thermo gravimetric analysis (TGA)

The thermal analysis comprises of the methods by which physical and/or chemical properties of a substance are measured as a function of temperature. In this work

TGA, differential thermal analysis (DTA) thermograms were measured with a STA 409 C thermal analysis device (Netzsch). All samples of oxide powders were measured performed with an identical heating and cooling cycles. The powder sample was heated at the rate of 2 °C/min in a corundum crucible under a flow of dry hydrogen or ambient air. The layer perovskite oxide powder was filled to  $\frac{3}{4}$  of crucible height independent of the same sample weight. The structural changes on each sample after the measurement were analyzed by XRD.

#### *4.6.5 Optical microscope*

Optical microscopy samples were prepared using standard metallographic techniques. In some cases samples were embedded in hot mount with phenolic resin. The samples were polished using 10 $\mu$ m diamond emery sheet. Final polishing was done with 1 $\mu$ m polycrystalline diamond suspended in oil. Prepared samples were observed using 2000x magnification Leica MeF3A optical microscope equipped with a digital image CCD camera.

#### *4.6.6 Scanning electron microscope (SEM) and EDAX*

Images of the chemically reduced catalytic surfaces and layered perovskite oxide fractured surfaces were obtained, using a field emission gun scanning electron microscope (Philips XL 30). An acceleration voltage of 10 kV was chosen, yielding beam currents of about 18–20  $\mu$ A. Secondary electrons (SE) were detected in all cases, as they provide a better morphology contrast than the backscattered electrons (BSE). The charging effect was observed on a layered perovskite oxides and polymer Nafion membrane electrodes due to the poor electronic conductivity. Charging effect was minimised by gluing the MEA catalyst surface with a piece of the conducting carbon/aluminum tape on the sample holder. This procedure yielded satisfactory results, so that additional Au sputtering was not applied in order to preserve the nano structured electrodes. A fine particle of oxide powders were pressed on a soft conducting carbon tape and fixed on the sample holder. Cross-section of the MEA was prepared by cutting a small strip and fixed it to the edge of the vertical sample holder. Images of the catalyst surface and MEA cross-section were taken at several magnifications. However, the nanoparticles on the carbon support grains were not able to scan clearly, as the resolution of the microscope was limited to about 5 nm.

X-rays emitted from the atoms with a characteristic energy distribution is unique to the element from which it is originated. The EDAX analysis was carried out in line scan mode to perform elemental specific analysis along a certain direction.

In order to get required signal intensity in element analysis the acceleration energy of the electron beam was set to be three times higher than the X-ray energy emitted by the electron transition of the relevant elements. It allows detecting signals of different elements and its spatial resolution is in the range of 10 to 100 nm, depending on the detected element.

#### 4.6.7 Atomic force microscope (AFM)

The functionality of AFM is based on the inter-atomic force between a thin tip and the surface atoms, see figure 4.11. By scanning the tip over a defined area of the surface, it is possible to receive detailed information about the surface topography. The AFM could either be operated in contact mode where repulsive coulomb forces dominate or in non-contact mode where attractive Van der Waals forces prevail. The former case is termed static atomic force microscopy and the latter dynamic atomic force microscopy. Contact mode AFM is unfavorable for samples that are either weakly bound or soft, because the tip can simply move or damage the surface features. The resulting images are generally not highly resolved. AC mode AFM, which operates in intermittent contact regime or in non-contact regime, solves this problem. In AC mode, the cantilever with the mass  $m$  oscillates near its resonant frequency  $\omega_0$  given by the equation

$$\omega_0 = \sqrt{\frac{k_c}{m}} \quad (4.3)$$

where,  $k_c$  is cantilever spring constant.

In the intermittent contact mode the tip is closer to the sample and the amplitude of the oscillation is bigger than in the non-contact mode. The interaction between the tip and the sample is predominately vertical, thus negligible lateral forces exists.

The AFM images were obtained with an Autoprobe cp (Park scientific instruments) microscope using silicon probe. Phosphorus (n) doped silicon cantilevers of 1-10 ohm-cm with typical force constant 0.01–0.03 N/m, 20 nm radius of curvature was employed. High-resolution images were acquired at a scanning frequency of 1-3 Hz. The samples were dried in desiccators before scanning with AFM tip, notably niobates and tantalates were hygroscopic, which absorbs moisture from the atmosphere. The optical microscope light was turned off while scanning over the Nafion membrane due to expansion of the polymer chains under the light radiation.

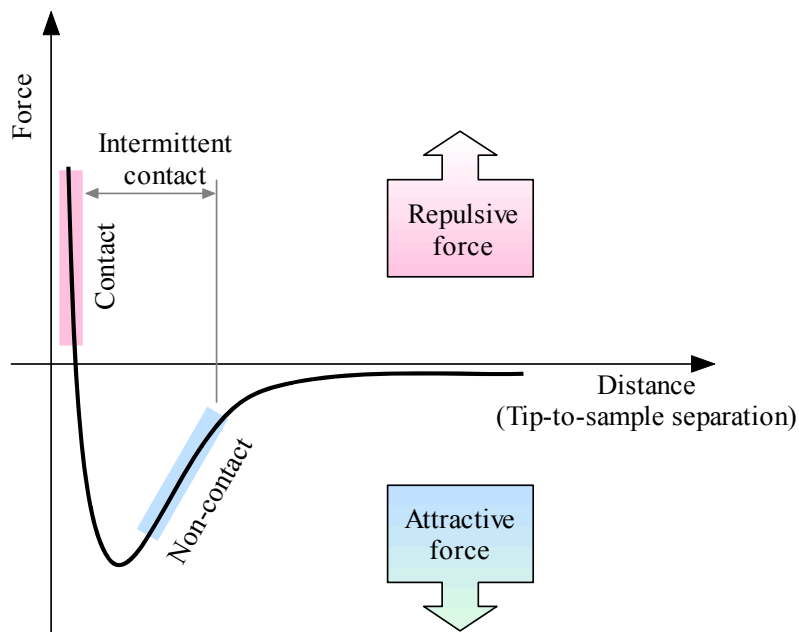


Figure 4.11: Dependence of the interatomic force between tip and sample atoms and its distance.

#### 4.6.8 AC impedance analyser

Proton conductivity is one of the key properties of a solid electrolyte which directly affects the performance of an electrochemical cell through ohmic losses. Therefore, in order to attain a high sensitive current, the area resistance of a proton conductor should be low. The proton conductivity is a dynamic process. When a sensor device has to be operated under such complex conditions, it is important to study the temperature and relative humidity dependents. Thus the effects of temperature on protonic conductivities of the membranes were measured in a two-electrode cell, where the membrane was sandwiched between Pt electrodes of  $1.76 \text{ cm}^2$  in area. A temperature-controlled heater was used to measure temperature dependent proton conductivity study in air and hydrogen containing atmospheres. The effects of temperature and RH on ionic conductivities of the membranes were measured. The RH was regulated by retaining appropriate salt solution or pure water at the bottom of the cell and the measurements were done at 100 % RH, the cell was also flushed with humid nitrogen.

As the aim of sensor development was to simplify the design construction, the relative humidity dependence was not conducted for all measurements; nevertheless

the ambient humidity was monitored with laboratory hygrometer. These values were compared with literature data [14]. The electrodes were connected to an HP 4192A LT impedance analyser (Japan) interfaced with self-programmed software. The complete impedance spectra were recorded in the frequency range of 5Hz to 13 MHz and the membrane resistance was considered in the range of kilohertz on Nyquist plot. The conductivity was calculated from this resistance, thickness of the membrane, and the area of the electrodes.

Layered perovskite D-J phases were performed with ionic conductivity measurements in air and humid hydrogen atmospheres. The measuring instruments were used as mentioned in section 4.5.2, the cell arrangements were slightly changed. The solid oxide electrolyte was plated with Pt by chemically reduced or sputter electrodes. The electrolyte was protonated before plating, the protonation procedures were described in section 4.4.3. The pellet was pasted with ceramic glue in face of alumina tube provided with gas flow channel, the arrangements were placed in “Kiel cell” (figure 4.6).

#### 4.6.9 Cyclic voltammetry (CV)

Cyclic voltammetry of chemically reduced electrodes and gas diffusion electrodes of Pt/C were measured with EG & G potentiostat model 273(Ireland). Platinum sheet/mesh was used as counter electrodes. The working electrode of geometric surface area of 1.4 cm<sup>2</sup> was symmetrically provided on both sides. The saturated Ag/AgCl<sub>2</sub> was used as a reference electrode. The CV curves of the chemically reduced electrode layers were measured in round bottom beaker with magnetic stirrer containing 1 M H<sub>2</sub>SO<sub>4</sub> with a scan rate of 5 mV/s between -0.3 and 1.5 V<sub>Ag/AgCl<sub>2</sub></sub>. Initially, continuous cyclic scan between the limits were applied to the electrode until a reproducible voltammetric curve was obtained for about 10 min. This treatment refers to electrode activation, it irreversibly oxidizes adsorbed organic impurities on the electrode surface [15]. Sometimes, the electrode activation was not able to remove the impurities. Under such circumstance, it is necessary to extend the electrode potential sweep limit to more positive potentials during a couple of scans to ensure the complete elimination of impurities. For cyclic voltammetry measurements, the electrolyte was purged with argon (argon 5.0) in order to remove traces of dissolved oxygen for 15 min prior to the measurements.

### References to chapter 4

- [1] P. Millet, F. Andolfatto and R. Durand, *J. Appl. Electrochem.* **25** [3], 233-9 (1995)
- [2] D.L. Smith, "Thin Film Deposition", McGraw-Hill, (1995)
- [3] A. Auciello and A.I. Kingon, Proceedings of ISAF '92. IEEE Eighth International Symposium on Applications of Ferroelectrics, Greenville, SC, USA, pp. 320-331 (1992)
- [4] H. Takenaka, E. Torikai, Y. Kawami, and N. Wakabayashi, *Int. J. Hydrogen Energy* **7** [5], 397-403 (1982).
- [5] C.M. Huang, C.Y. Yuh and M. Farooque, Mohammad. U.S. Pat. Appl. Publ. US 2004157104 (2004)
- [6] H. Takenaka, E. Torikai, Y. Kawami, and N. Wakabayashi, *Adv. Hydrogen Energy* **1**, 107-17 (1981)
- [7] M. Sakhivel and W. Weppner, *Sens. Actuators, B* **113** [2], 998-1004 (2006)
- [8] M. Dion, M. Ganne and M. Tournoux, *Mater. Res. Bull.* **16** [11], 1429-35 (1981)
- [9] V. Thangadurai and W. Weppner, *Ionics* **7** [1 & 2], 22-31 (2001)
- [10] V. Thangadurai and W. Weppner, *J. Mater. Chem.* **11** [2], 636-639 (2001)
- [11] [http://www.ionic-systems.de/Instrumente/PG\\_02.html](http://www.ionic-systems.de/Instrumente/PG_02.html)
- [12] J.L. Langford, *Appl Cryst* **4**, 164 (1971)
- [13] <http://www.ccp14.ac.uk/>
- [14] R. Jiang, H. Kunz, F. Russell and M. James, *J. Power Sources* **150**, 120-128 (2005)
- [15] B.E. Conway, *Anal. Chem.* **45** [8], 1331-1336 (1973)

---

## Chapter 5

### Results

#### *5.1 Polymer based hydrogen sensor*

This section deals with the structural and electrical property performance of the solid polymer proton conducting membrane based hydrogen sensor.

##### *5.1.1 Structure and morphology characterisation of Pt electrodes*

The crystal structure and particle size of the Pt electrodes were analysed by means of X-Ray diffraction. The results of the structure and morphology of chemically reduced Pt electrodes on the deposited solid proton conductor electrolyte prepared by the I-R method are given as a function of the type and quantity of reductants.

###### *5.1.1.1 Reducing agent: NaBH<sub>4</sub>*

Figure 5.1 shows three X-ray diffraction patterns of the Pt electrode deposited onto a Nafion 117 membrane by the chemical reduction method using 0.01 M Pt(NH<sub>3</sub>)<sub>4</sub>Cl<sub>2</sub> metal salt solution and three different concentrations of NaBH<sub>4</sub> reducing agent. The patterns of three samples are shown in the figure 5.1, the top pattern (d) was obtained with a NaBH<sub>4</sub> concentration of 0.08 M, the next one (c) with 0.04 M, and the one below (b) with 0.01 M. The bottom one (a) shows the pattern of the standard JCPDS card 4–802 [1]. All peaks could be well indexed according to the standard. Pattern (b) shows more distortion due to the fact that the base polymer membrane is not covered properly due to lower particle density, which resulted in noisy peaks compared with the top one. All three sample patterns show that the particles were mostly crystalline with (111) orientation parallel to the surface independent of the reductant concentration. Different peak widths were observed for different concentrations of the reductant. Increasing peak widths of the X-ray diffraction patterns were observed for decreasing concentration of the reductant. Smaller particle sizes were estimated from broader peaks, which appeared in the 0.01 M pattern. The crystallite diameters (d) were determined from Scherrer's equation as described in section 4.6.1.

The crystallite's diameters were estimated from the full width at half maximum (FWHM) intensity of Pt (111), (200), (220) (311) at corresponding 2θ values of 40°, 46°, 68°, and 82°, respectively. The calculated grain size diameter (d-values) for different concentrations are shown in Table 5.1. Figure 5.2 shows the particle size

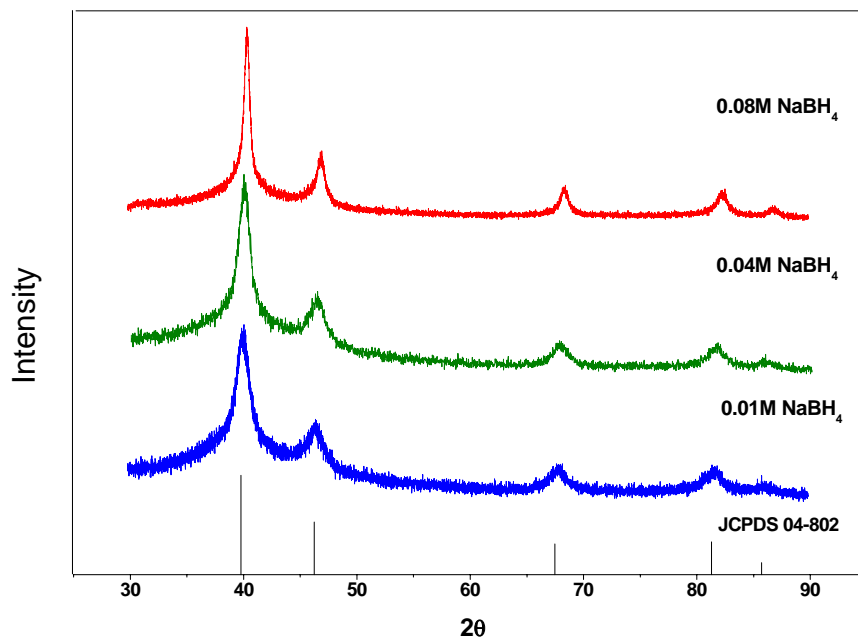


Figure 5.1: X-ray diffraction pattern of Pt | Nafion electrode prepared from 0.01M  $\text{Pt}(\text{NH}_3)_4\text{Cl}_2$  and three different reductant concentrations (a) JCPDS 04-802, (b) 0.01 M , (c) 0.04 M and (d) 0.08 M  $\text{NaBH}_4$ . Optical micrographs of the corresponding samples are shown in the pattern (b), (c) and (d).

Table 5.1: Average crystalline diameter of the Pt grains deposited at the surface of the Nafion electrolyte prepared from  $\text{Pt}(\text{NH}_3)_4\text{Cl}_2$  of 0.01 M concentration and various reductant concentrations.

Conc. of $\text{NaBH}_4$ (mol)	$39.7^\circ$ (111) d (nm)	$46.2^\circ$ (200) d (nm)	$67.5^\circ$ (220) d (nm)	$81.2^\circ$ (311) d (nm)	$85.7^\circ$ (222) d (nm)
0.01	16	24	49	46	23
0.04	74	26	16	15	13
0.08	211	116	142	105	92



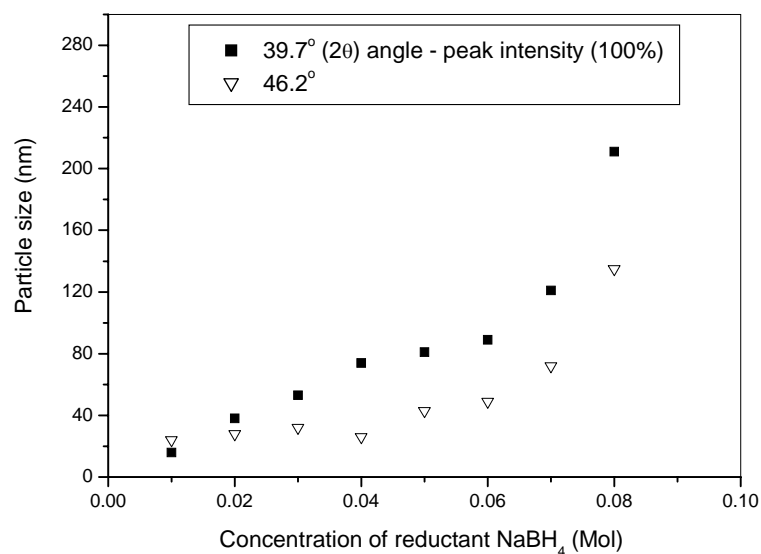


Figure 5.2: Particle size effect on electrode preparation using different concentrations of reducing agent NaBH<sub>4</sub>.

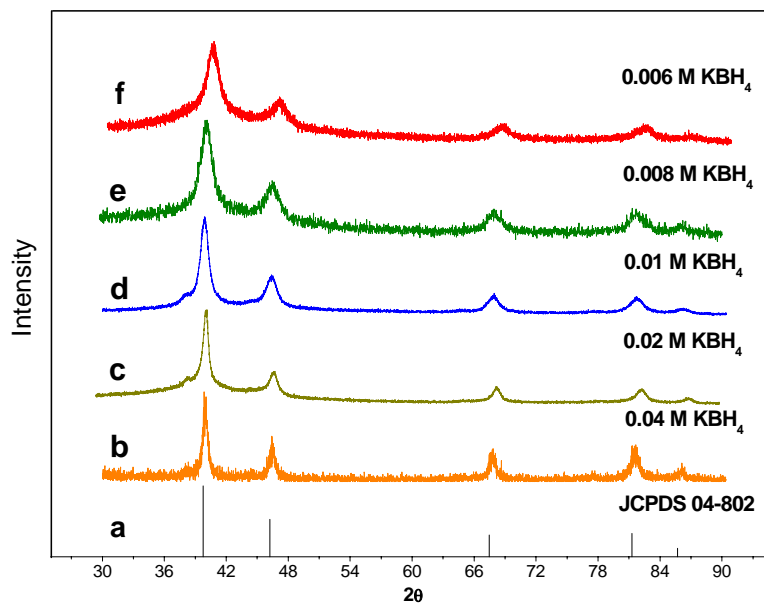


Figure 5.3: X-ray diffraction pattern of Pt | Nafion electrode prepared from 0.01 M Pt(NH<sub>3</sub>)<sub>4</sub>Cl<sub>2</sub> and five different reductant concentrations (a) JCPDS 04-802, (b) 0.04 M, (c) 0.02 M, (d) 0.01 M, (e) 0.008 M and (f) 0.006 M KBH<sub>4</sub>.

determined from (111) and (200) plane crystal orientation at angles of 39.7° and 46.2°, respectively.

#### 5.1.1.2 Reducing agent: $\text{KBH}_4$

Figure 5.3 shows the X-ray diffraction patterns of the platinum electrode samples deposited by applying a 0.01 M  $\text{Pt}(\text{NH}_3)_4\text{Cl}_2$  metal salt solution and five different concentrations of reducing agent, i.e., 0.006, 0.008, 0.01, 0.02 and 0.04 M  $\text{KBH}_4$  (from top to bottom). The vertical line pattern shows the data of the standard JCPDS card 4–802. All peaks could be well indexed according to the standard. All five XRD patterns show only Pt peak angles, irrespective of the concentration of the reducing agent, i.e., the  $[\text{Pt}(\text{NH}_3)_4]^{2+}$  ions of the impregnated Nafion membrane were reduced completely. The peaks observed for lower concentrations of the reducing agent show larger distortions than observed for higher concentrations as well as larger broadening. The broader peaks show the strain induced between the smaller Pt particles growth. The size of the Pt particles (Table 5.2) was calculated using Scherrer's equation.

#### 5.1.1.3 Comparison of: $\text{NaBH}_4$ and $\text{KBH}_4$

The effects of reducing agent concentrations on the Pt reduction process were observed by comparing the extreme concentrations of strong and weak reducing agent. Figure 5.4 shows the X-ray diffraction patterns of the platinum electrode samples prepared by using the two different reducing agents. The two bottom patterns were recorded for the sample prepared with 0.01 M concentration of  $\text{NaBH}_4$  and  $\text{KBH}_4$  as reducing agent. The two top patterns were recorded for the sample prepared with 0.08 M concentration of  $\text{NaBH}_4$  and  $\text{KBH}_4$  as a reducing agent. Initially, both sets of samples were impregnated with 0.01 M concentration of  $\text{Pt}(\text{NH}_3)_4\text{Cl}_2$ . The bottom pattern shows the data of the standard JCPDS card 4–802. All peaks could be well indexed according to the standard. All four XRD patterns show only Pt peak angles, irrespective of the type and concentration of the reducing agent, i.e. the impregnated Nafion membrane contains  $[\text{Pt}(\text{NH}_3)_4]^{2+}$  ions which were reduced completely. The size of the Pt particles were calculated using Scherrer's equation. The calculated crystallite size diameter (d-values) for different concentrations are given in Table 5.2.

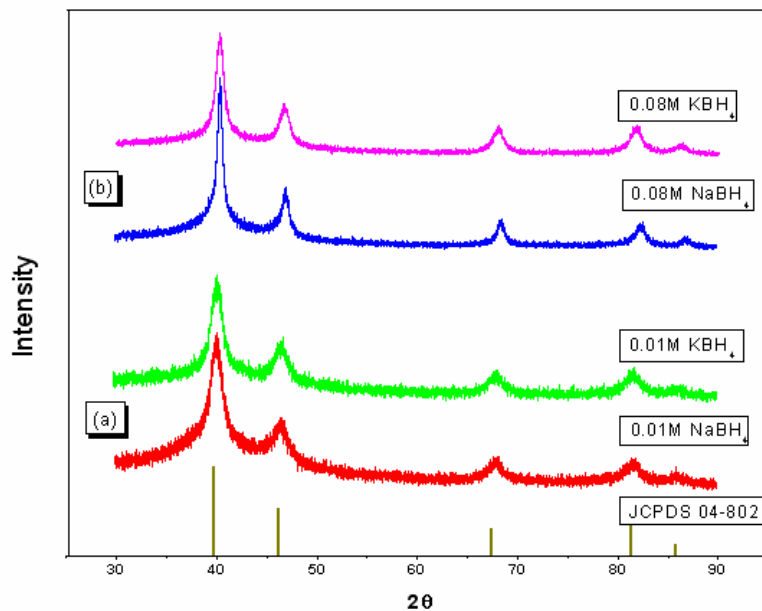


Figure 5.4: X-ray diffraction pattern of the Pt | Nafion<sup>®</sup> electrode assembly prepared from 0.01M Pt(NH<sub>3</sub>)<sub>4</sub>Cl<sub>2</sub> and three different reductant concentrations (a) 0.01 M NaBH<sub>4</sub> and KBH<sub>4</sub>, (b) 0.08 M NaBH<sub>4</sub> and KBH<sub>4</sub>.

Table 5.2: Average crystallite diameter (d) of the Pt grains deposited at the surface of the Nafion electrolyte prepared from Pt(NH<sub>3</sub>)<sub>4</sub>Cl<sub>2</sub> of 0.01 M concentration and two different reductant concentrations.

Angle (2θ)	d(nm) 0.01 M NaBH <sub>4</sub>	d(nm) 0.01 M KBH <sub>4</sub>	d(nm) 0.08 M NaBH <sub>4</sub>	d(nm) 0.08 M KBH <sub>4</sub>
39.7° (111)	16	28	211	262
46.2° (200)	24	32	116	135
67.5° (220)	49	56	142	158
81.2° (311)	46	51	105	117
85.7° (222)	23	30	92	108

### 5.1.2 XPS spectral studies of Pt/Nafion

Figure 5.5 shows Pt 4*f* and S 2*p* XPS spectra acquired after the protonation of the chemically reduced Pt film on Nafion membrane. These data indicate that no evidence is found for the formation of platinum sulfides after the complete removal of H<sub>2</sub>SO<sub>4</sub> solution at the catalytic Pt surface (A Pt 4*f* binding-energy shift of 1.0–1.4 eV is expected for the formation of PtS<sub>x</sub> compounds [2]). Similar results were reported for the reaction of S<sub>2</sub> with Pt (111) [3]. The surface roughness of the Pt film was not influenced by the formation of platinum sulfides. In general, the formation of PtS<sub>x</sub> from metallic Pt and S<sub>2</sub> should occur spontaneously, i.e.,  $\Delta G = -180$  to  $-230$  kJ/mol [4], but the big cohesive energy of Pt and the large difference between the surface-free energies of Pt and S provide a potential barrier for the penetration of S into the bulk of the metal.

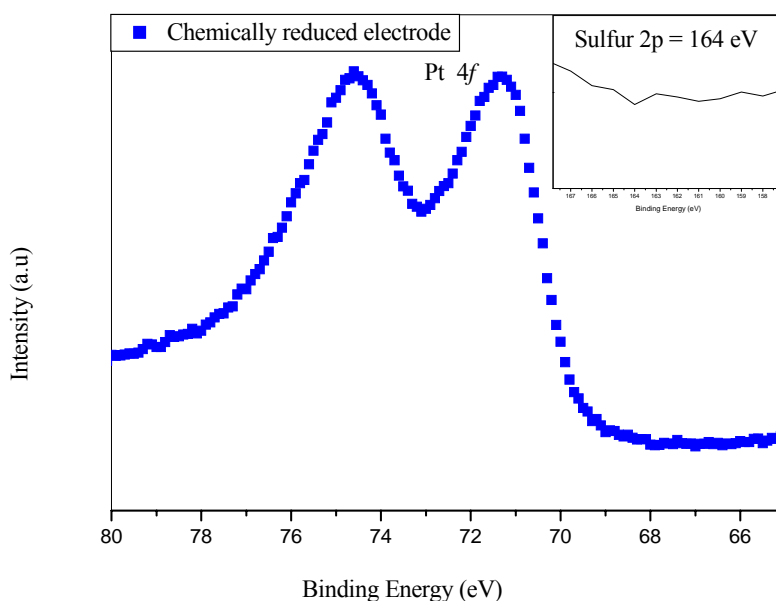


Figure 5.5: XPS Pt 4*f* spectra chemically reduced film electrode.

### 5.1.3 Optical micrographs of chemically reduced electrodes

The chemically reduced platinum electrode surfaces were viewed by the optical microscope. The images have shown different surface morphologies of the Pt particles for the samples prepared using the three different metal salt concentrations of 0.001, 0.01 and 0.1 M Pt(NH<sub>3</sub>)<sub>4</sub>Cl<sub>2</sub>. Microscopic examination of Pt deposited at the lowest (0.001 M) concentration has shown that isolated and inhomogeneous

platinum particles were deposited on the Nafion membrane. The images of the surfaces observed for the highest concentration have shown thick and fully covered layers, which are commonly believed not to be suitable for sensor applications, where the three-phase region is a primary requirement. Therefore, all other electrodes were prepared at the optimum level of 0.01 M concentration of  $\text{Pt}(\text{NH}_3)_4\text{Cl}_2$ .

#### 5.1.3.1 Reducing agent: hydrazine

The optical micrograph of Pt deposition on a Nafion membrane by the T-T method i.e., using hexachloroplatinic acid and hydrazine as a metal salt and reducing agent, respectively, resulted in isolated thicker particles. Moreover the adherence of the metallic film on Nafion was poor and the particle distribution was not uniform over the exposed to the solution surfaces. The initial experiments showed that the results were not reproducible using this method.

#### 5.1.3.2 Reducing agents: $\text{NaBH}_4$ and $\text{KBH}_4$

Optical micrographs of the chemically reduced ionic polymer- electronic platinum electrode surfaces with Na and K reductant compounds are shown in figure 5.6. The Pt surfaces of the samples prepared by three different concentrations of  $\text{NaBH}_4$  and  $\text{KBH}_4$  using 0.1, 0.01, and 0.001 M solutions as reducing agents. The  $\text{NaBH}_4$  reduced Pt surfaces show highly strained and smooth reflecting film, whereas in the case of 0.01 M  $\text{KBH}_4$  less strain and larger particle sizes are observed. XRD crystallite size analysis for the corresponding samples were in agreement with the optical observations. In addition, both sample surfaces have shown a major difference in porosity. The samples prepared with  $\text{KBH}_4$  as reducing agent have given more homogeneous pores than those prepared with  $\text{NaBH}_4$ . Porous structures were obtained by the weak reducing nature of the potassium compound. Similar conditions were followed to prepare Pt electrodes using  $\text{NaBH}_4$  and  $\text{KBH}_4$  as well, in which the reduction rate differed from one another. The higher the reduction rate the more strain and particle growth is observed, whereas the weak reducing agents show less strain and slow growth rate, resulting in uniform small pores.

The optical micrographs of Pd metal electrodes chemically reduced on Nafion membrane are shown in figure 5.7. The Pd metal deposition was possible with palladium metal complex, after the impregnation and reduction time was slightly increased. The formation of Pd film on Nafion membrane was too thick and continuous. A similar amount of both reducing agents was applied in the concentration range of 1 to 0.001 M. In contrast to Pt in the case of Pd formation

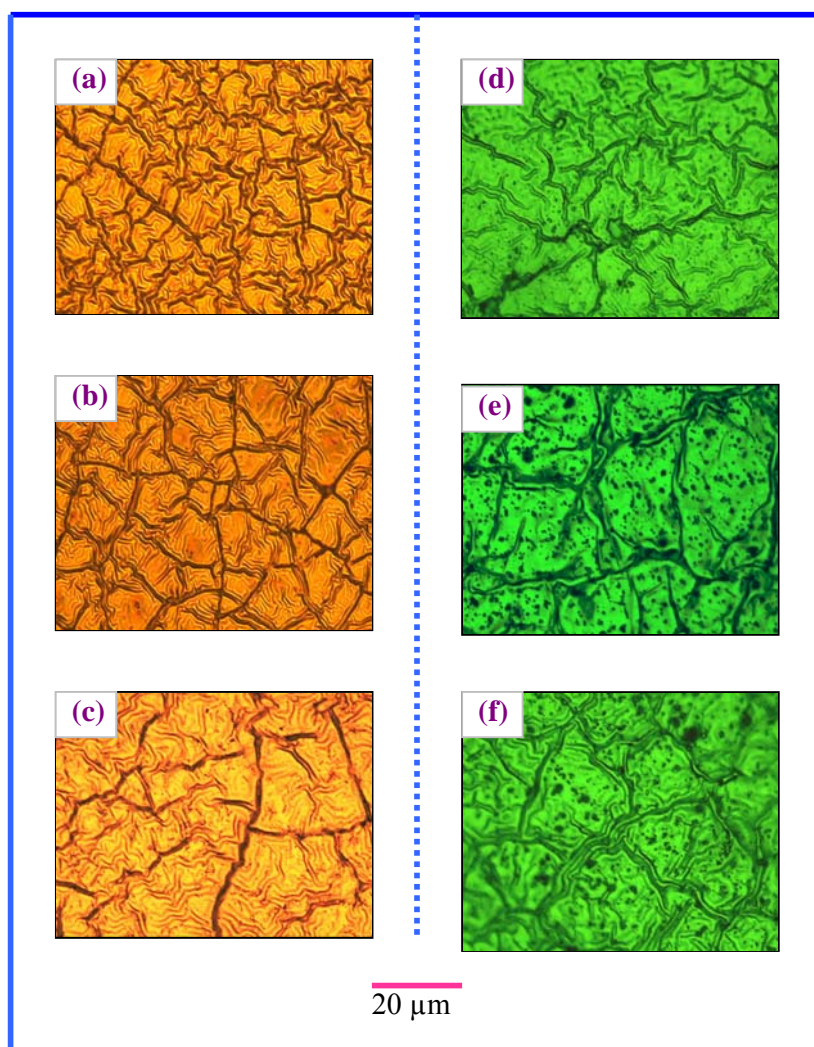


Figure 5.6: Optical micrograph of chemically deposited Pt electrode on Nafion 117 membrane using 0.01 M  $\text{Pt}(\text{NH}_3)_4\text{Cl}_2$  and reductant concentrations (a) 0.001 M, (b) 0.01 M, (c) 0.1 M of  $\text{NaBH}_4$ ; and (d) 0.001 M, (e) 0.01 M, (f) 0.1 M of  $\text{KBH}_4$ .

neither a strain induced film nor porous structure was obtained. A non-porous structured film contains less or nearly no TPB sites for the electrochemical reduction or oxidation processes.

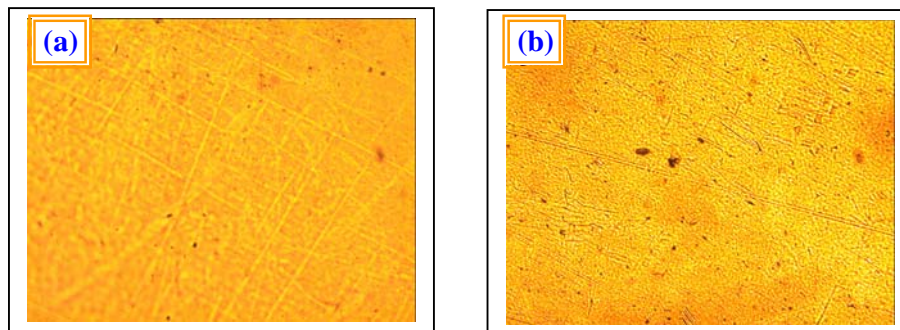


Figure 5.7: Optical micrograph of Pd film deposited on Nafion membrane using 0.01 M of (a) NaBH<sub>4</sub> and (b) KBH<sub>4</sub>.

The effect of water uptake by the membrane was observed with chemically reduced Pt metal films. Such studies were conducted only by optical micrographs, since high resolution scanning microscopes are operated under vacuum and are not suitable for water uptake studies. The formation of the micro cracks of the electrode surface structure under wet conditions is shown in figure 5.8. The samples of both Na and K based reducing agents have shown similar results. For comparison, the MEA electrode of a dry surface is shown. These microcracks were reversible, i.e., it tends

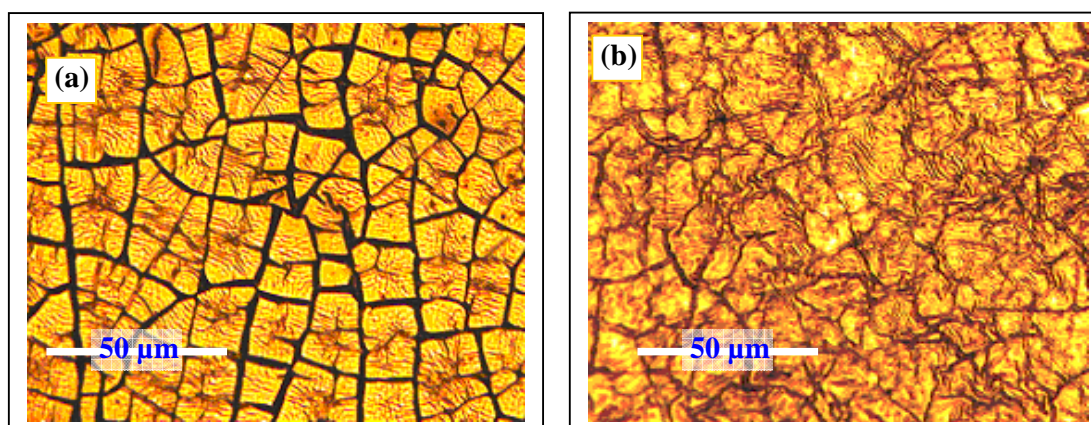


Figure 5.8: Optical micrograph of (a) wet and (b) dry Pt|Nafion electrode surfaces.

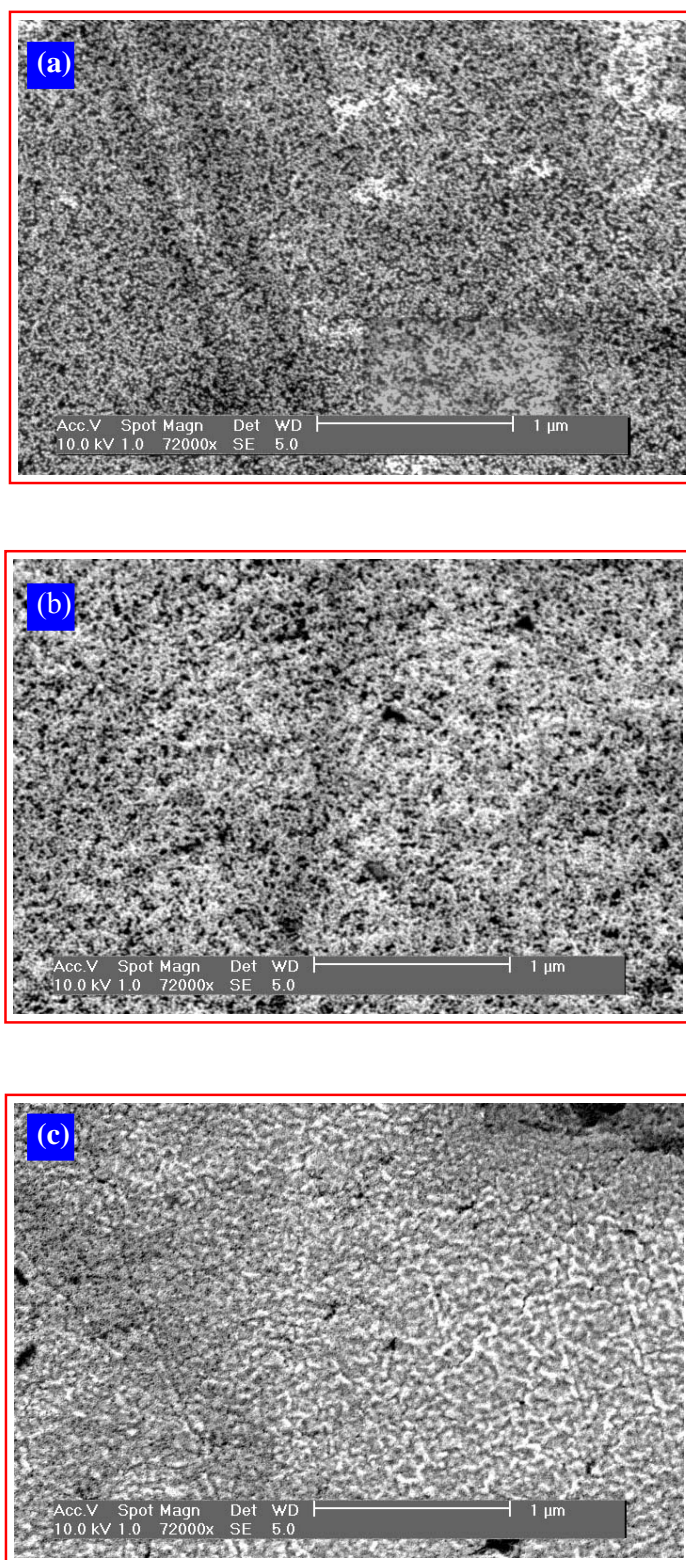


Figure 5.9: SEM photograph of Pt electrode deposited on Nafion117 membrane using 0.01 M  $\text{Pt}(\text{NH}_3)_4\text{Cl}_2$  and reductant concentration (a) 0.01 M, (b) 0.04 M & (c) 0.08 M  $\text{NaBH}_4$ .



to close when the membrane gives off the surface water, the isolated cluster of particles results in poor electrical conductivity. The higher and lower magnifications of the optical images were observed in both wet and dry conditions.

#### 5.1.4 SEM of chemically reduced electrodes

##### 5.1.4.1 Reducing agent: $\text{NaBH}_4$

The morphologies of the Pt electrode deposited on the Nafion membrane were observed in SEM as shown in figure 5.9. The three different micrographs were taken from electrode surfaces of 0.01 M Pt  $(\text{NH}_3)_4 \text{Cl}_2$  prepared with concentrations of 0.01, 0.04 and 0.08 M  $\text{NaBH}_4$ . In general, all three micrographs show uniform and homogeneous sizes of the electrode particles. However, the size of the particles increased when the concentration of the reductant increased. The particle sizes estimated from the XRD pattern agreed well with those derived from SEM micrographs. Figure 5.9 (a) shows small particles with enhanced surface area for high electrocatalytic activity, which was obtained from the smallest reductant concentration (0.01M); but most of the particles are isolated from each other, resulting in an interruption of the electrical contact. In contrast, high concentrations show good electronic contact. The particles were grown up to micrometer size with less surface area, which reduces the electrocatalytic activity. The micrograph shows an optimum particle size of 74 nm and good interparticle connections were found at 0.04 M concentration which also shows a good electrochemical sensor performance.

##### 5.1.4.2 Reducing agent: $\text{KBH}_4$

The SEM images of the porous structures of the chemically reduced ionic polymer-platinum electrode surfaces prepared with various concentrations of  $\text{KBH}_4$  reductant are shown in figure 5.10. Pt deposited at the lowest (0.006 M)  $\text{KBH}_4$  concentration resulted in isolated and inhomogeneous platinum particles deposited on the Nafion membrane. The Pt surface of the sample prepared with 0.04 M  $\text{KBH}_4$  shows high strain and an increased particle size. In addition, both sample surfaces show a large variation in porosity. The samples prepared with an intermediate 0.01 M concentration of  $\text{KBH}_4$  as reducing agent provide more homogeneous pores than in the case of 0.02 and 0.008 M. Porous structures were obtained with the weak reducing nature of  $\text{KBH}_4$ . Similar conditions were applied when five Pt electrodes five different  $\text{KBH}_4$  concentrations with different reduction rates.

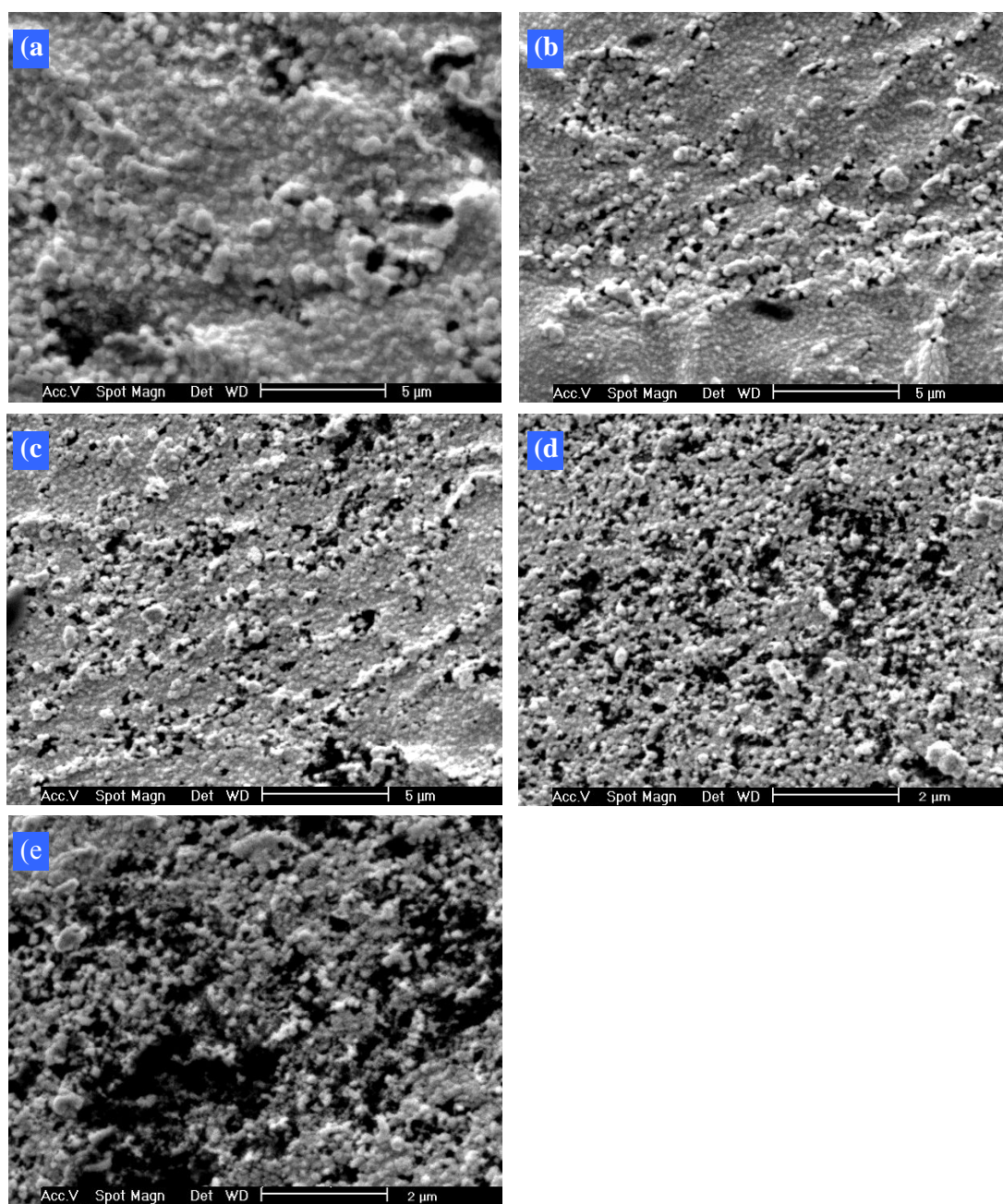


Figure 5.10: SEM photograph of Pt electrode deposited on Nafion117 membrane using 0.01 M  $\text{Pt}(\text{NH}_3)_4\text{Cl}_2$  and reductant concentrations (a) 0.04 M, (b) 0.02 M, (c) 0.01 M, (d) 0.008 M, and (e) 0.006 M  $\text{KBH}_4$ .

#### 5.1.4.3 The effect of deposition temperature

Identical structures and surface morphologies of Pt deposited on Nafion membrane were obtained by increasing the reduction temperature, whereas an effect of temperature in chemical reduction on Nafion membrane has occurred at the electrode-electrolyte interface. It was observed that the Nafion membranes impregnated at higher temperatures have more isolated Pt particles deposited deeply in the membranes. SEM images of the cross section of Pt metal|Nafion interface prepared by 0.01 M NaBH<sub>4</sub> at two different temperatures are shown in figure 5.11. In the case of the films deposited at higher temperatures, a thick dense Pt layer is observed at the interface and a considerable number of isolated particles was found as far as 20 μm from the membrane surface. The density of particles decreases with increasing distance from the surface, whereas the particle size increase with the distance from the surface. A well-defined interface boundary between Pt metal particles and Nafion was established in the case of room temperature deposition. The thickness of the interfacial film is only 0.5 μm and there are few isolated particles within the membrane.

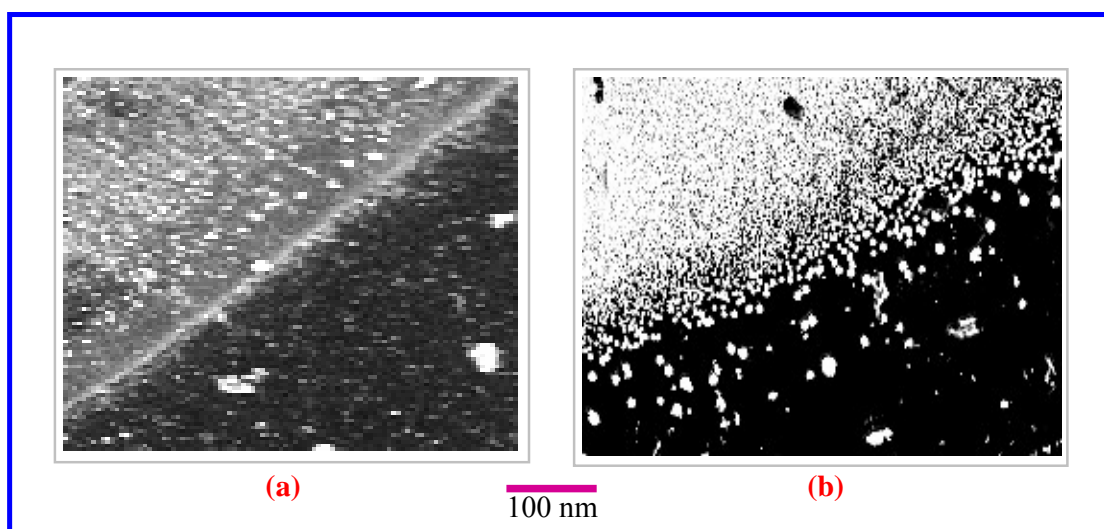


Figure 5.11: The cross sectional photograph of SEM images at Pt|Nafion interface prepared in (a) 27 °C and (b) 70 °C temperature.

### 5.1.5 The elemental analysis of chemically reduced electrode by EDX

Since the chemical route was applied to prepare electrodes with complex metal salts, these may contain impurity elements. Surface species were analysed using an energy dispersive X-ray spot analyser. Figure 5.12 shows the spectrum of Pt peak in M and L energy level and a small percentage of fluorine and carbon peaks due to the base perfluorated polymer membrane. For comparison EDX spectrum of sulfonated Nafion membrane with Pt electrode is shown in figure 5.12(inlet), the presence of copolymer PTFE shows a fluorine peak in the backbone of the polymer structure and less amount of sulphur from  $\text{SO}_3^-$  group.

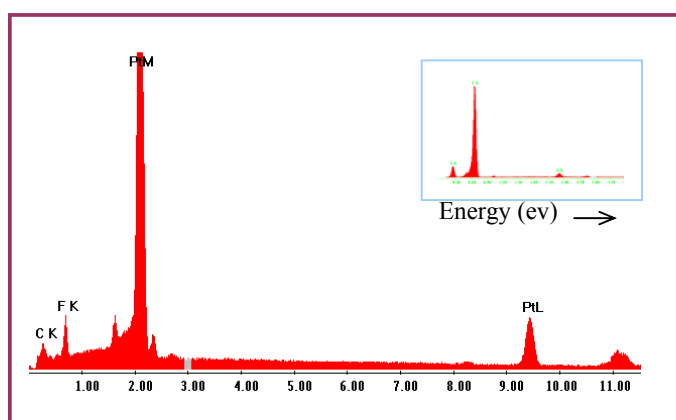


Figure 5.12: EDX spectra of Pt|Nafion MEA surface and (inlet) Nafion

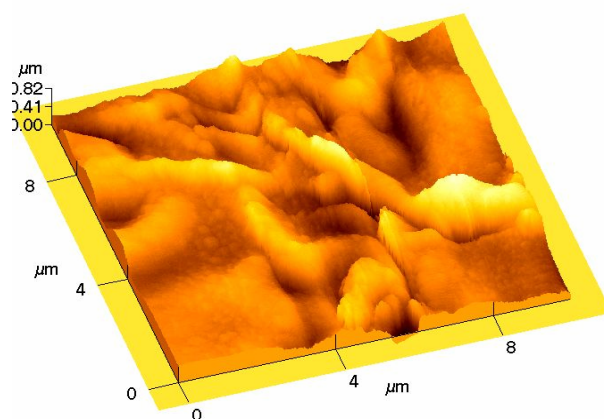


Figure 5.13: AFM image of MEA Pt surface.

### 5.1.6 Atomic force micrograph of chemically reduced electrodes

During the SEM study, it was found that the Nafion membrane undergoes a state of dehydration under vacuum condition. Simultaneously it may affect the chemically bonded Pt particle structure with the substrate influence. Therefore, the structural observation was extended to ambient condition measurable techniques. Figure 5.13 shows the atomic force micrograph of MEA Pt particles observed under air. The chemically reduced MEA surface is characterised by a granular appearance of platinum metal with a peak/valley depth of approximately 200 nm. This granular nano-roughness seems to be responsible for producing a high level of sensor performance and also provides a porous nature with a large number of TPB regions. During the AFM study, it was also found that the platinum particles are porous and, to some extent, possess coagulated shapes. The pliable Nafion membrane was affected with optical microscope light radiation during the measurements. The large surface roughness of the membrane was produced by an artifact effect on the images.

### 5.1.7 Electrical conductivity of Pt/Nafion MEA's

The proton conductivity measurements were carried out using a Nafion 117 membrane stored at various relative humidity's and temperatures. The AC impedance measurements were conducted on type of electrodes prepared from various methods as described in the previous chapter. Figure 5.14 shows the change in conductivity of the Nafion 117 membrane with the relative humidity of saturated inorganic salt solution maintained in a hydrogen gas containing specific atmosphere prior to the measurement. The measured conductivity was compared with the reported [5] data obtained for electrodes of Pt metal sheet, each of the saturated salt solution measurements were marked with numbers 1 to 4. The conductivity increased rapidly with the relative humidity from 30 to 48 %, but further increase in humidity did not improve the proton transport. Therefore, the experiments were conducted in an ambient atmosphere with a relative humidity in the range of 48–60 %. Figure 5.15 shows the conductivity of the membrane as a function of temperature using MEAs with chemically reduced, mechanically pressed, and physically sputtered electrodes. The change in the membrane conductivity was measured over the temperature range of 27–100 °C. Beyond 100 °C, Nafion behaves non linear because the membrane has a glass transition temperature of about 110 °C [6]. The increased molecular motion changes the structure of the membrane and causes lower water content.

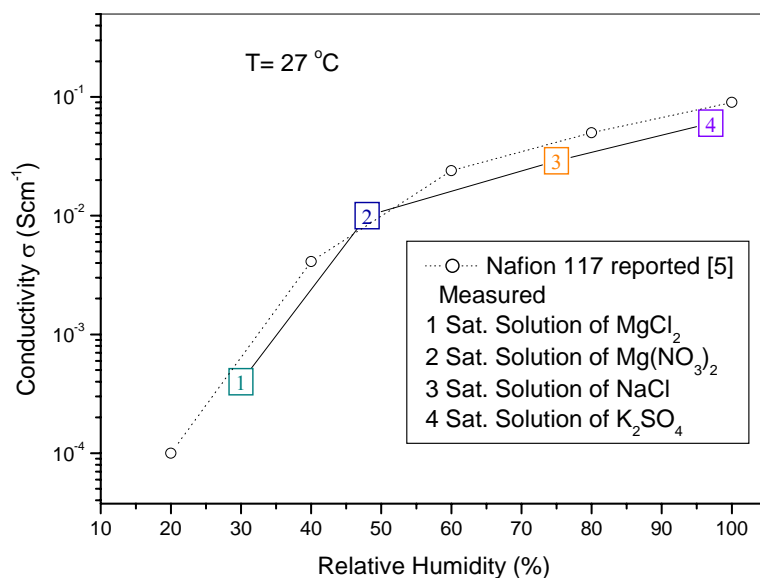


Figure 5.14: Conductivity of Nafion117 as function of various Relative Humidity (RH%) using standard solutions.

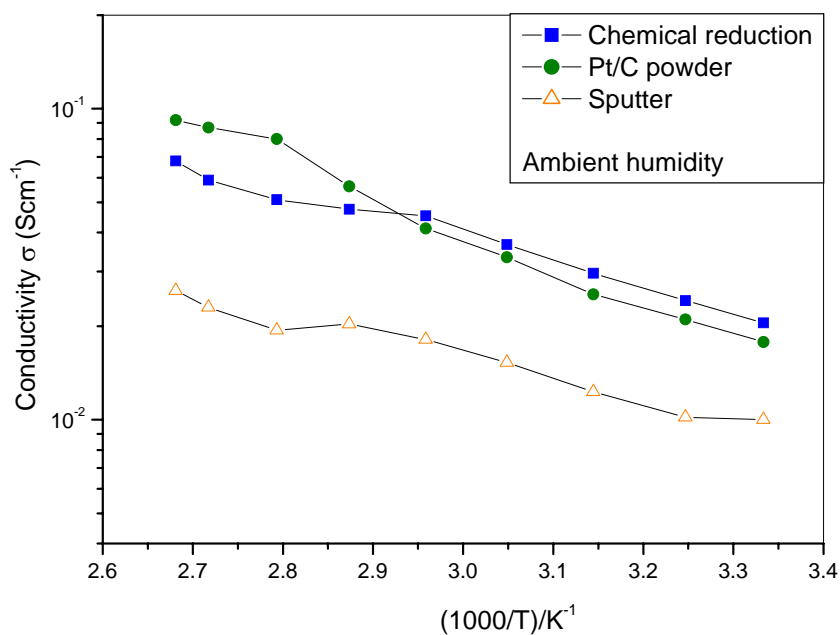


Figure 5.15: Temperature dependent proton conductivity of Pt|Nafion MEA's prepared with three different methods.

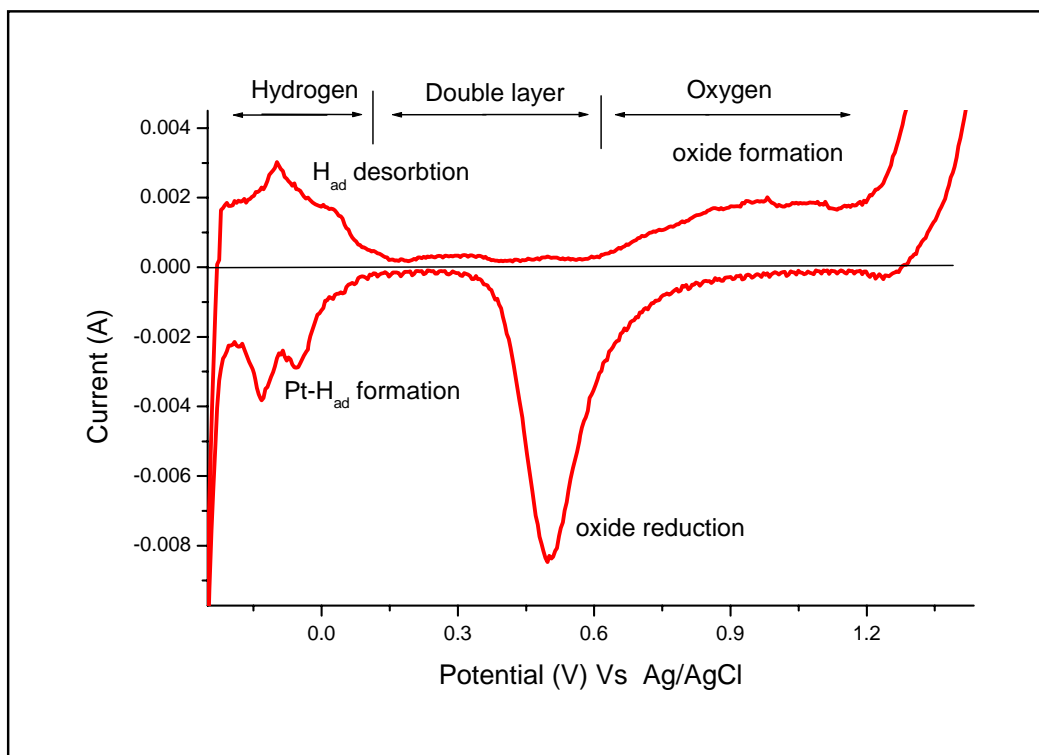


Figure 5.16: Cyclic voltammetry of chemically reduced Pt electrode measure in 1 M H<sub>2</sub>SO<sub>4</sub> at 27 °C.

Table 5.3: Electrocatalytic active surface areas of various amount of Pt loading.

Pt/C amount taken (gms)	Active surface area of Pt in Pt/C electrode (cm <sup>2</sup> /g)	0.01 M Pt (NH <sub>3</sub> ) <sub>4</sub> Cl <sub>2</sub> and various KBH <sub>4</sub> (mol)	Active surface area of Pt in Pt/Nafion electrode (cm <sup>2</sup> )
0.055	1.531	0.006	0.023
0.060	2.084	0.008	0.054
0.065	2.525	0.01	0.096
0.070	3.159	0.04	0.084
0.080	3.741	0.08	0.062

#### *5.1.8 Estimation of electroactive surface area*

The impregnated gas diffusion electrodes were characterised independent of the sensor testing by cyclic voltammetry. Figure 5.16 presents the resulting voltammograms for the chemically reduced Pt on Nafion electrode. During this initial cycling procedure no changes in shape or size of the voltammograms can be observed at room temperature. The electrochemically active surface area of the electrodes was determined by the integration of the cathodic part of the hydrogen region [7]. The charge under both the anodic and the cathodic branch of the voltammogram was integrated in the Had area. The double layer capacitance of the gas diffusion electrodes was estimated from the cyclic voltammograms. The result presents the charge consumed or released during the adsorption/desorption of one monolayer of hydrogen on the electrode surface. The resulting electroactive surface areas are listed in Table 5.3.

#### *5.1.9 Sensing characteristics of solid polymer based systems*

The Sensing performance of the amperometric sensor was examined for the detection of H<sub>2</sub>. In order to develop the electrode material and preparation method, a sequential approach was followed. The response of platinum and palladium was tested and three methods of preparation were screened at a constant H<sub>2</sub> concentration. The electrocatalytic Pt particle was deposited on the solid polymer Nafion electrolyte by means of chemical reduction, mechanical attachment and physical sputtering. The hydrogen gas response behaviour of the electrodes are presented for the percentage to ppm level.

##### *5.1.9.1 Response based on the type of electrode materials*

Figure 5.17 shows the performance of chemically reduced platinum and palladium electrode on Nafion. For the percentage level of H<sub>2</sub> concentrations, palladium shows a higher current than the platinum electrode, but the stability of the palladium films was not comparable with that of platinum. Since the absorption (or diffusion) coefficient of Pd is two orders of magnitude higher than that of Pt, the observed higher current are in agreement. A higher tendency to form Pd as hydride in H<sub>2</sub> containing atmospheres [8], which was readily show a brittle nature on a continuous film. Heating the palladium arrangement is required to remove the structurally stored hydrogen, since the aim of the work is to develop a device for operation at room temperature. Further studies were focused on the platinum electrode. The preliminary experiments were conducted below 4% H<sub>2</sub> concentrations, i.e., below the LEL.



Figure 5.18 shows the typical step response curve for 4% H<sub>2</sub> in air at room temperature. The response was studied by changing the atmosphere of the sensing electrode from a flux of air to the flux of gas with defined hydrogen concentration. With air, the short circuit current between two electrodes was zero. On contact with the sample gas, a rapid increase in the current was observed. The 90% response time

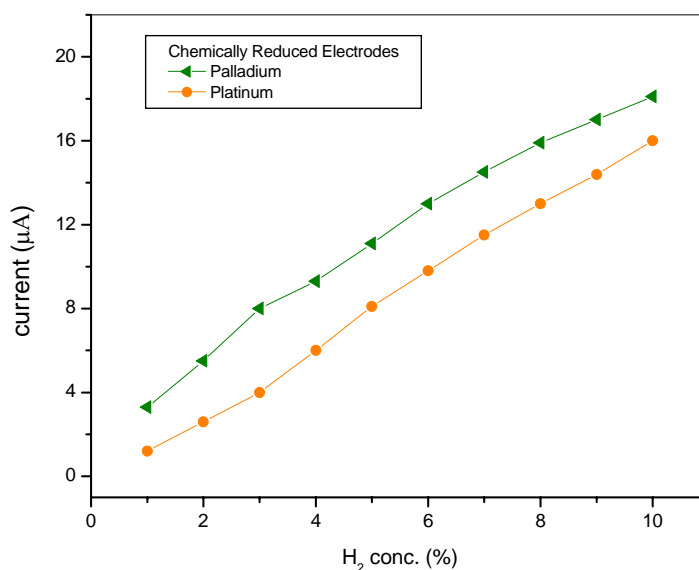


Figure 5.17: Calibration plot of sensor output current from two different noble metal electrodes.

was about 20 s and the steady state current value was 320 μA. When the air flow was resumed, the current returned to zero within about 15 s. When the sensor was investigated at 4% of H<sub>2</sub> diluted with N<sub>2</sub> the observed current was 420 μA with  $t_{90} = 14$ s. In this case, the cell is actually a H<sub>2</sub>-O<sub>2</sub> fuel cell which accounts for a higher electrical current due to the large hydrogen activity difference. In both cases, calibration different H<sub>2</sub> concentrations shows a linear dependence with the current over wide ranges. As mentioned in chapter 2, this fact suggests that for practical purpose the amperometric sensor is more accurate than the potentiometric sensor. The following results were obtained by using N<sub>2</sub> as a carrier gas, which has resulted in increase current at low ppm detection levels. Moreover the objective of this work was based on fuel cell type short circuit amperometric H<sub>2</sub> sensor.

### 5.1.9.2 Response in dependence of the electrode deposition method: Sputtered electrode

Figure 5.19 shows the typical response curve at various concentrations of hydrogen using a sputtered Pt electrode on Nafion membrane. The thickness of the film was about 200 nm at both sides of the membrane. The electrode sputtered under vacuum was hydrated again in boiling water. During the first exposure to relatively low hydrogen concentration, the sensor tends to show an increasing current without approaching a steady state. Further increase in  $H_2$  shows a decrease of the current even during the initial period of gas exposure. The response of the initial experiments with sputtered Pt film were seen to be concentration independent, thus further work was focused onto a stable and inexpensive way to prepare under ambient conditions.

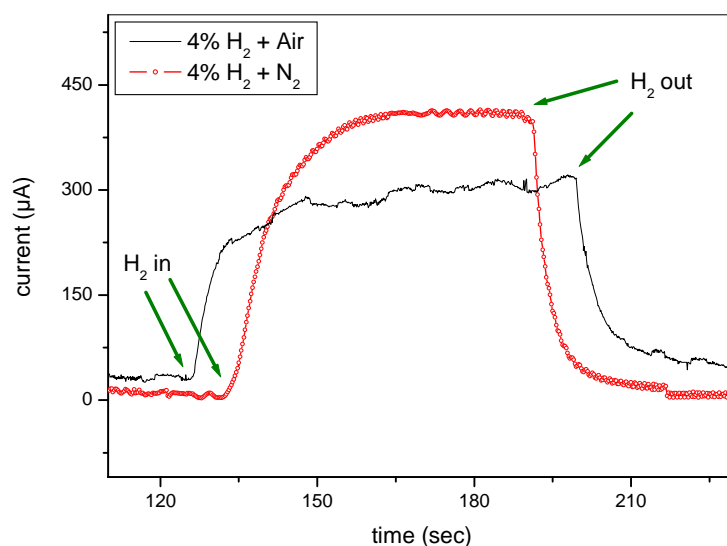


Figure 5.18: Effect of carrier gas on hydrogen sensing.

### 5.1.9.3 Response in dependence of the electrode deposition: Gas diffusion electrode (GDE)

As mentioned above the aim of this work is to develop a fuel cell type  $H_2$  sensor, the GDE electrode was used in fuel cell research, here the same was chosen as a catalyst layer. Figure 5.20 shows the  $H_2$  response on gas diffusion electrode prepared from the chemically reduced Pt/C powder. The response curve, i.e., the sensing current raises to a stable and eventually a plateau value and the background current recovers well in the absence of  $H_2$ . This behaviour implies that the Pt/C|Nafion electrode senses steadily. Figure 5.21 shows the detected steady state currents at different hydrogen

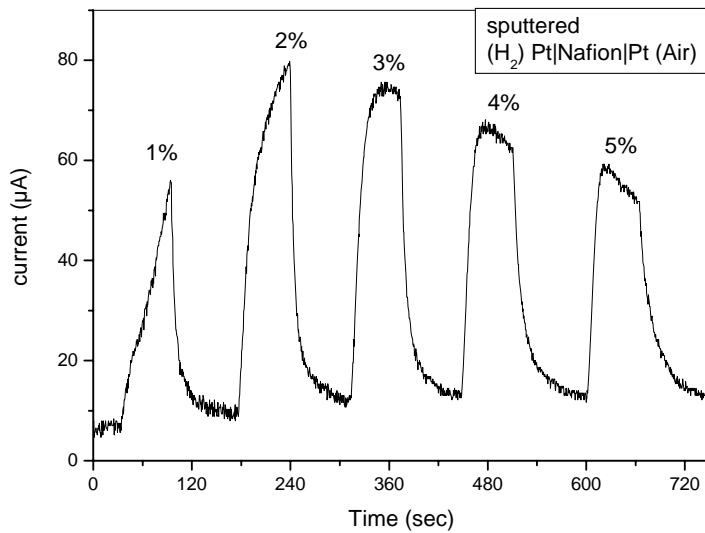


Figure 5.19: Sensor current signal of sputtered Pt electrode.

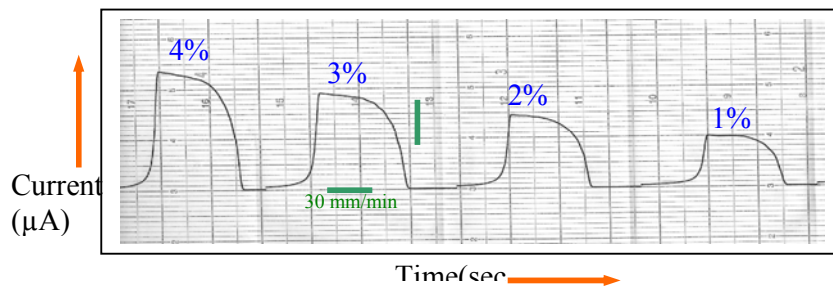


Figure 5.20: A typical step response of GDE electrode based sensor.

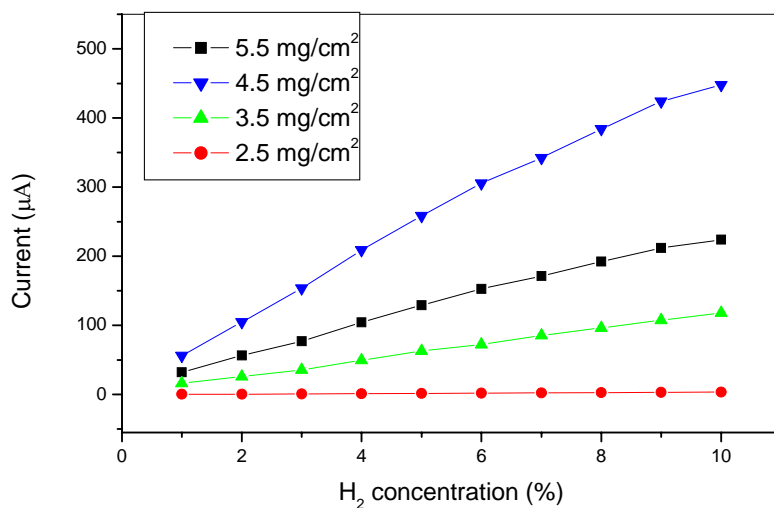


Figure 5.21: The effect of Pt loading on GDE electrode in sensing 1-10 % H<sub>2</sub> concentrations.

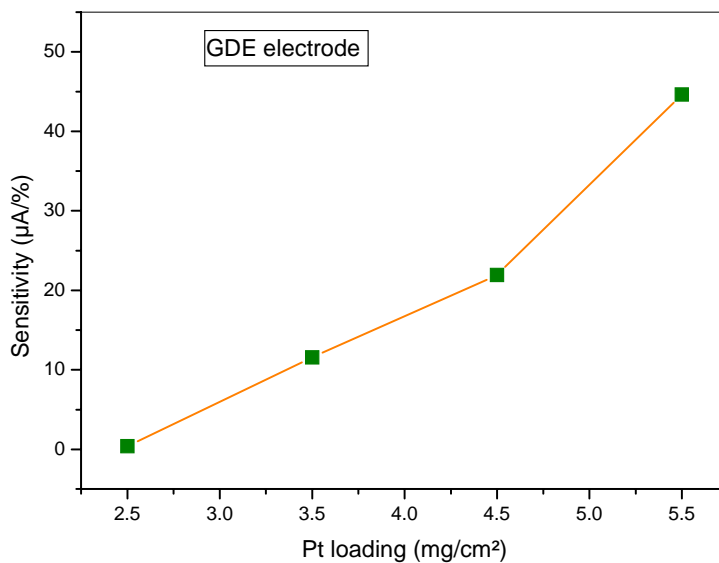


Figure 5.22: Sensitivity of the Pt/C/Nafion electrode as a function of Pt loading.

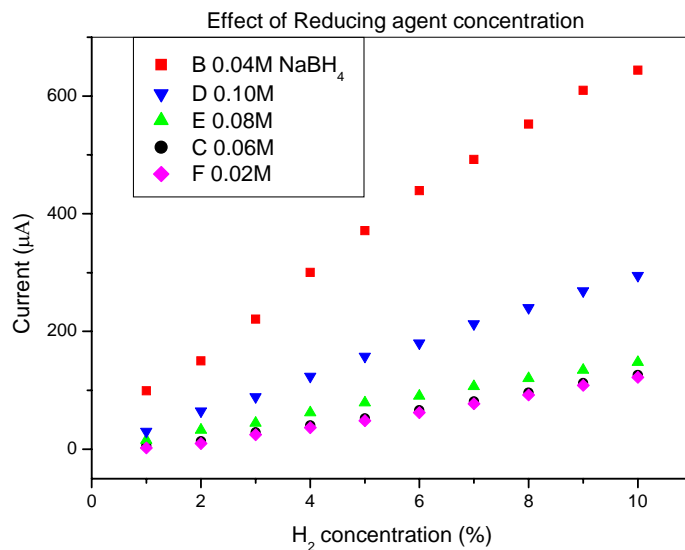


Figure 5.23: Approximate linear relationship between different reductant concentrations over a wide range of hydrogen concentration (1-10 %) and a

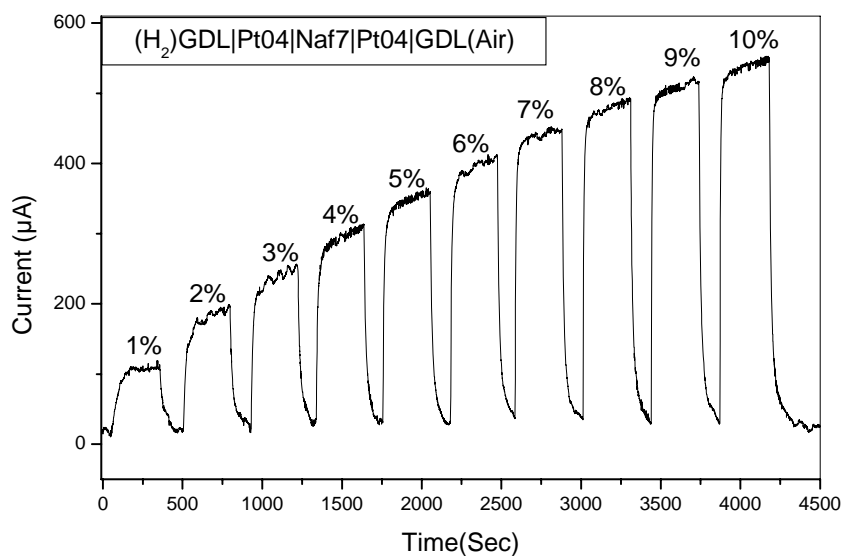


Figure 5.24: Response of the Pt | Nafion<sup>®</sup> electrode with GDL element with an area of 2 cm<sup>2</sup> prepared from 0.01 M Pt (NH<sub>3</sub>)<sub>4</sub> Cl<sub>2</sub> and 0.04 M NaBH<sub>4</sub> for hydrogen gas in the concentration range of 1-10 %.

concentrations. The effect of platinum loading was observed with the sensor response at 1–10% H<sub>2</sub> concentrations. It was optimised that the deposition of 4.5 mg/cm<sup>2</sup> shows a higher response current than lower and higher amounts of Pt loading. The slope of the straight line represents the sensitivity of Pt/C/Nafion electrodes for hydrogen sensing. This sensitivity increases nonlinearly by increasing amounts of Pt loading, corresponding to an increase in the active surface area, as shown in figure 5.22. The micrographs of electrode surface reveal that the Pt clusters are evenly dispersed in the Pt/C/Nafion electrode and are sufficiently employed as catalytic sites in sensing hydrogen even at a higher Pt loading.

#### *5.1.9.4 Response in dependence of the electrode deposition method: Chemically reduced electrode*

The direct deposition of Pt on Nafion was carried out by using [Pt(NH<sub>3</sub>)<sub>4</sub>Cl<sub>6</sub> · H<sub>2</sub>O] metal salt and alkali borohydrates as reducing agent. Most of the work was focused towards the development of this electroless deposition of Pt electrode on proton conductors. Thus, elaborated studies were carried out to optimise the various parameters such as reductant concentrations, temperature, and time of preparation of the Pt electrodes. The H<sub>2</sub> sensing performance of electrodes chemically reduced by the I-R method were characterised using two types of current collectors, namely with GDL and carbon woven fibres.

#### *5.1.9.5 Response based on current collector: Gas diffusion layer (GDL)*

Figure 5.23 shows the effect of reductant concentration in dependence of 1–10% hydrogen. Samples in reductant concentrations in the range from 0.004 to 0.1 M of NaBH<sub>4</sub> and KBH<sub>4</sub> were tested. Significant changes in the current are seen for a ±0.02 M difference in reductant concentration which is influenced by the surface morphology of the electrodes. The formation of porous structures plays an important role in sensing hydrogen, i.e., the number of TPB sites decides the electrochemical process. The particle size effect on the electrode may enhance the higher current in the case of NaBH<sub>4</sub> than KBH<sub>4</sub> samples. The former shows smaller particles with larger surface areas. The sensor current output for a wide range of H<sub>2</sub> concentration (1–10%) shows a linear response and in particular, 0.04 M NaBH<sub>4</sub> samples with GDL show a higher current.

Typical step responses of the sensor element Pt | Nafion (0.01M Pt (NH<sub>3</sub>)<sub>4</sub> Cl<sub>2</sub> and 0.04M NaBH<sub>4</sub>) to various concentration steps of hydrogen in nitrogen at room

temperature are shown in figure 5.24. Before applying hydrogen, the sensors were thoroughly purged with nitrogen gas which has shown a base current of 25  $\mu\text{A}$  (figure 5.24). Different gas concentrations were tested in the ranges beginning at 1% and then going up to 10% hydrogen in steps of one percent hydrogen partial pressure for 5 minutes each time. Similar step responses were observed for each gas concentration. The sensor performance was checked by exposing the sensor to 10% hydrogen and then going down to 1%; the sensor behaviour is in agreement with that shown in figure 5.24. A linear relationship between the output current and the hydrogen concentration was observed for all concentrations. Figure 5.25 shows nearly linear behaviour which was observed for both forward and reverse direction for concentration changes from 1 to 10% of hydrogen gas. The average maximum sensitivity was observed to be  $0.01 \mu\text{A cm}^{-2}\text{ppm}^{-1}$ ,  $0.007 \mu\text{A cm}^{-2}\text{ppm}^{-1}$  and  $0.008 \mu\text{A cm}^{-2}\text{ppm}^{-1}$  in the hydrogen partial pressure ranges of 1–2%, 3–7% and 8–10%, respectively.

The step response measurements show that the sensor responds very rapidly for hydrogen concentrations between 1 and 10 %. The response time ( $t_{90}$ ) was typically less than 10–50 s. Both the response and recovery times decrease with increasing hydrogen concentration. Figure 5.26 shows the response time ( $t_{90}$ ) versus  $\text{H}_2$  concentration in the range 1–10% for a Pt | Nafion sensor electrode prepared from 0.04 M  $\text{NaBH}_4$ .

Figure 5.27 shows cyclic exposure of the Pt | Nafion sensor element to 4 % hydrogen and no hydrogen. Identical maximum output currents were observed for several cycles changing within one minute from 0 to 4 % hydrogen. In general, the sensor needs to operate for much longer periods of time. So, the lifetime was also investigated and it was shown that a sufficient stability exists over several days. A downward drift in the output current was in the range of 2% per day.

Typical hydrogen responses for multicyclic gas exposure of the sensor were observed for each concentration. Figure 5.28 shows a number of identical cycles that attained the maximum output current measured for 1, 4, 6 and 10 % of hydrogen gas concentration. Up to the LEL value, the maximum current was constant over several cycles, but in the higher concentration range, the current was observed to decrease after 40 cycles. Furthermore, the process leading to attain an equilibrium water content corresponding to a given RH of the test gas is slow. For practical purposes, the sensor needs to operate for much longer periods of time. It was found that a sufficient stability exists over several cycles for hydrogen concentrations below the LEL concentration.

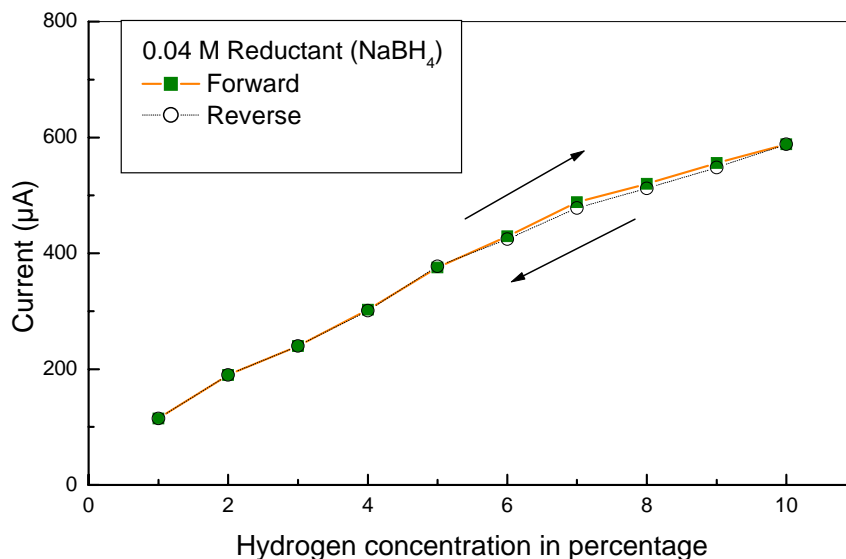


Figure 5.25: Approximate linear relation for 0.04 M NaBH<sub>4</sub> concentration over a wide range of hydrogen concentration (1-10 %) and a sensing area of 2 cm<sup>2</sup>.

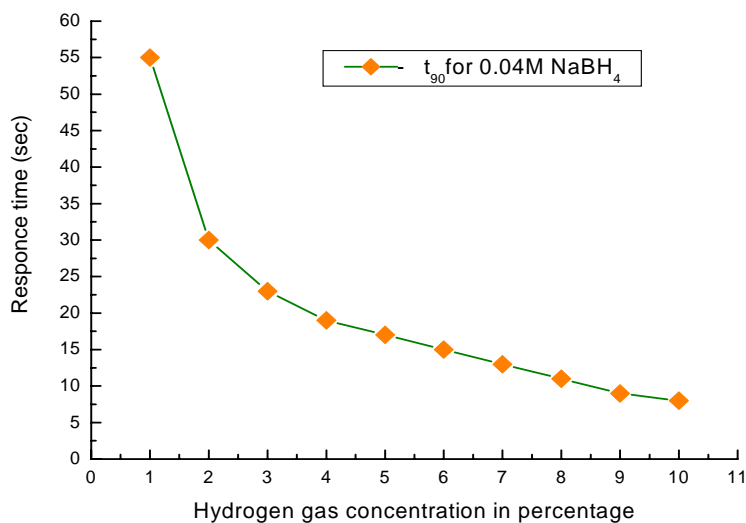


Figure 5.26: Response time vs. hydrogen concentration (1-10%) for Pt | Nafion<sup>®</sup> electrode prepared from 0.01 M Pt (NH<sub>3</sub>)<sub>4</sub> Cl<sub>2</sub> and 0.04 M NaBH<sub>4</sub>.



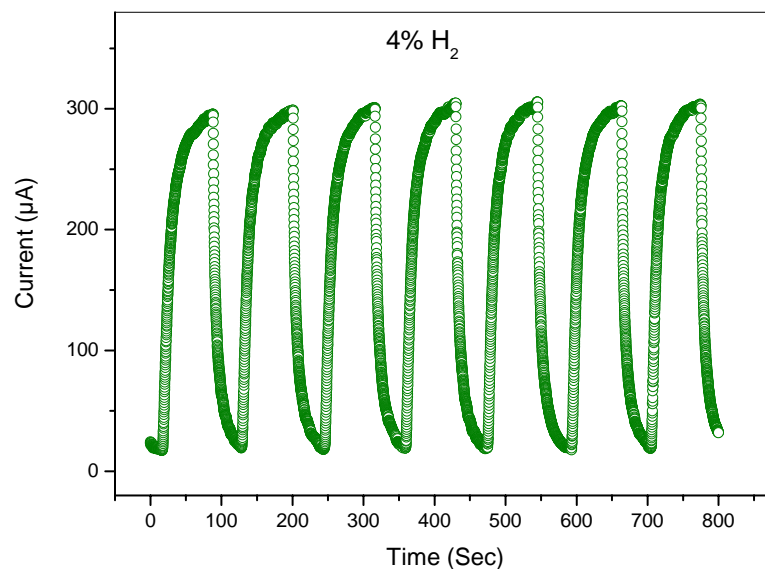


Figure 5.27: Cyclic behaviour of 4% hydrogen gas exposure to the sensor element Pt | Nafion<sup>®</sup> with an electrode area of 2 cm<sup>2</sup> from 0.01 M Pt (NH<sub>3</sub>)<sub>4</sub> Cl<sub>2</sub> and 0.04 M NaBH<sub>4</sub> at one minute time intervals.

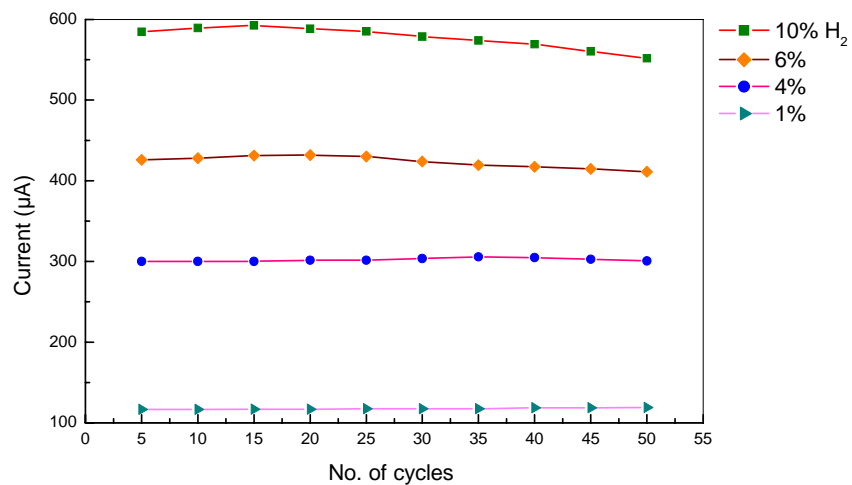


Figure 5.28: Stability of the sensor element Pt | Nafion<sup>®</sup> with an electrode area of 2 cm<sup>2</sup> from 0.01 M Pt (NH<sub>3</sub>)<sub>4</sub> Cl<sub>2</sub> and 0.04 M NaBH<sub>4</sub> for different hydrogen gas concentrations upto 50 cycles.

#### 5.1.9.6 Response in dependence of the current collector: Carbon woven fibre: High $H_2$ gas concentration response ( $NaBH_4$ )

The performance of the hydrogen sensor was observed by employing the Pt | Nafion (0.01 M  $Pt(NH_3)_4Cl_2$  and 0.01 M  $NaBH_4$ ) assembly for different concentration steps of hydrogen in nitrogen at room temperature. The response curve for 1 min exposure of 1–10%  $H_2$  gas is shown in figure 5.29. Different gas concentrations were tested in the ranges beginning at 1% and then going up to 10 % hydrogen in steps of one percent hydrogen partial pressure for 1 min each time. The calibration plot of steady current of the sensor versus hydrogen concentration is shown in figure 5.30. A linear relationship between the output current and the hydrogen concentration was observed for both forward and reverse direction of changes in the concentration from 1 to 10% of hydrogen gas. According to figure 5.30, the linear regression equation is  $y = -47.66 + 119.79x$ , where  $y$  and  $x$  are the response current ( $\mu A$ ) of the sensor and the concentrations (%) of hydrogen, respectively. The average maximum sensitivity was observed to be  $0.01 \mu A \text{ cm}^{-2} \text{ ppm}^{-1}$ ,  $0.007 \mu A \text{ cm}^{-2} \text{ ppm}^{-1}$  and  $0.008 \mu A \text{ cm}^{-2} \text{ ppm}^{-1}$  in the hydrogen partial pressure ranges of 1–2%, 3–7% and 8–10%, respectively. The response time ( $t_{90}$ ) to achieve a change in the signal level of 90% was typically less than 5–15 s. Both the response and recovery times decrease with increasing hydrogen concentration. When the samples were tested at low  $H_2$  concentrations (ppm level) a non-linear behaviour was observed.

#### 5.1.9.7 Response in dependence of the current collector: Carbon woven fibre: Low $H_2$ gas concentration response ( $KBH_4$ )

Optical micrographs of the Pt electrode surfaces prepared with 0.01-0.08 M  $KBH_4$  have shown a more porous nature than when prepared with 0.01-0.08 M  $NaBH_4$ . The porous surface electrode samples prepared with 0.01-0.08 M  $KBH_4$  were employed for the detection of low ppm  $H_2$  gas concentrations. Typical step responses of the sensor element Pt | Nafion (0.01 M  $Pt(NH_3)_4Cl_2$  and 0.01 M  $KBH_4$ ) to various concentration steps of 100–1000 ppm hydrogen in nitrogen at room temperature are shown in figure 5.31. Linear output current responses were observed for different samples over this hydrogen concentration range as shown in figure 5.32. The average maximum sensitivity of the sensor is  $0.0026 \mu A \text{ cm}^{-2} \text{ ppm}^{-1}$  in the range of 100–1000 ppm, which is about 3 times higher than reported [9]. Between 100 and 1000 ppm hydrogen, the response time is of the order of 25 and 5 s, in both forward and reverse

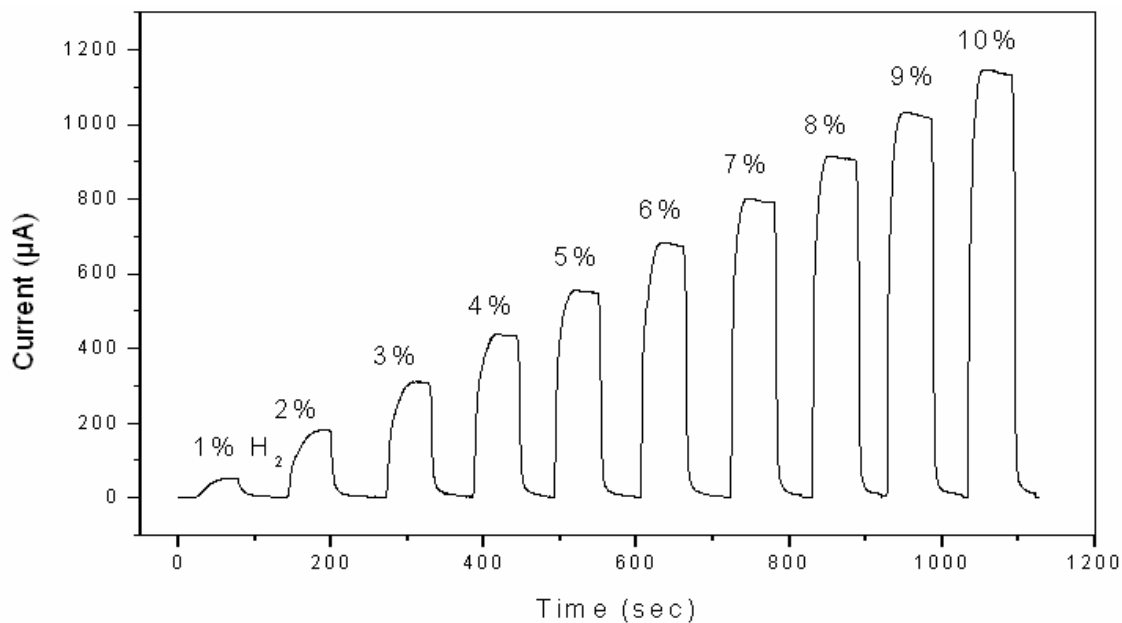


Figure 5.29: Response behaviour of the Pt | Nafion electrode sensor element with carbon woven fibre of an area of  $2\text{ cm}^2$  for hydrogen gas in the low concentration range of 1-10%.

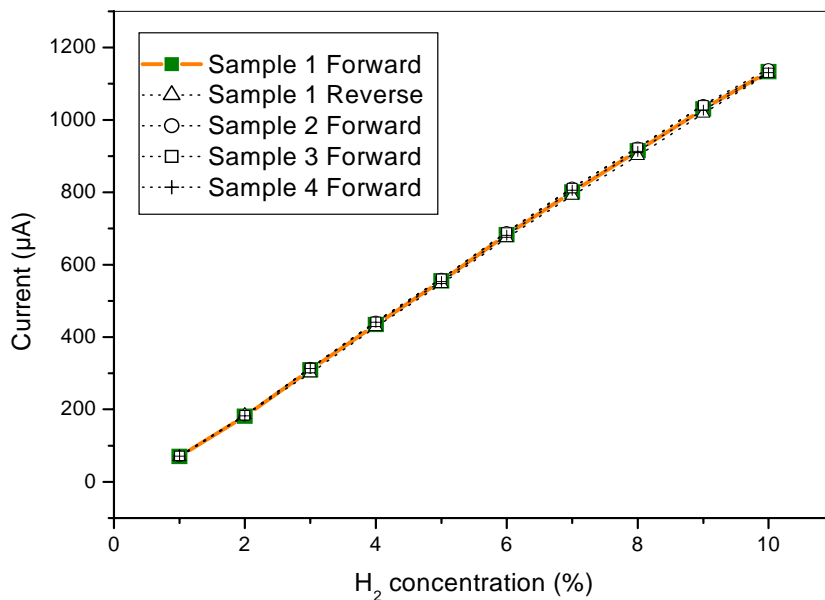


Figure 5.30: Linear relation for hydrogen concentration (1-10 %) range and a sensing area of  $2\text{ cm}^2$ . The dotted lines are results from calibrations with different samples.

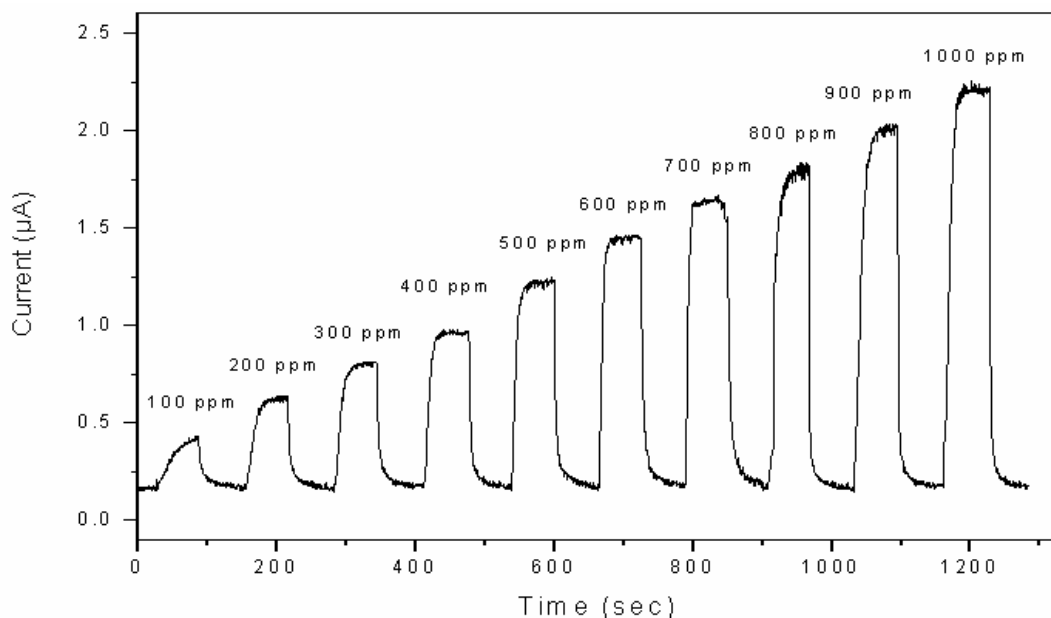


Figure 5.31: Response behaviour of the Pt | Nafion electrode sensor element with carbon fibre of an area of  $2 \text{ cm}^2$  prepared from  $0.01 \text{ M Pt}(\text{NH}_3)_4\text{Cl}_2$  and  $0.01 \text{ M KBH}_4$  for hydrogen gas in the low concentration range of 100-1000 ppm.

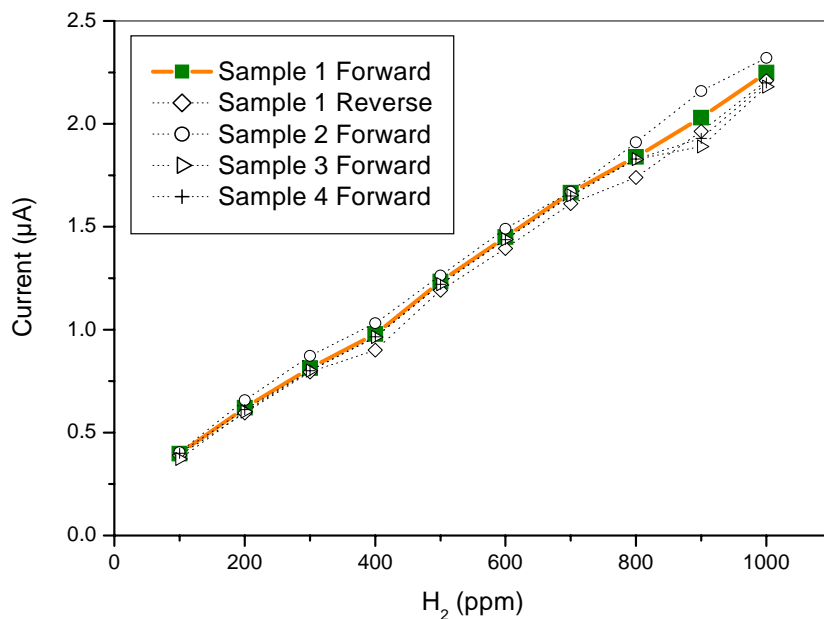


Figure 5.32: Linear relation for  $0.01 \text{ M KBH}_4$  concentration over a wide range of hydrogen concentration (100-1000 ppm) and a sensing area of  $2 \text{ cm}^2$ . The dotted lines are results from calibrations with different samples.

direction, respectively. For practical purposes, the detection of hydrogen at the low ppm level is important. The same sets of samples were exposed to 10–50 ppm hydrogen gas. The response curve for 1 min exposure of 10–50 ppm H<sub>2</sub> gas is shown in figure 5.33. Linear output current responses were observed for different samples over the hydrogen concentration ranges as shown in figure 5.34. The average maximum sensitivity of the sensor is 0.0046  $\mu\text{A cm}^{-2}\text{ppm}^{-1}$  in the range of 10–50 ppm. A summary of both high and low detection ranges with different sensitivities is listed in Table 5.4.

Varying thickness of the electrodes were observed by surface profilometry, which depends on the concentrations of the reducing agent being used. The sensitivity performance shows a wide range of H<sub>2</sub> concentrations. However, the sensitivity is proportional to the charging current rather than the electrode thickness. The optimum sensitivity was observed with an electrode prepared using 0.01 M concentration of KBH<sub>4</sub> as a reducing agent, the layer thickness of which was about 0.3  $\mu\text{m}$ . Electrodes prepared with higher KBH<sub>4</sub> concentrations (i.e 0.06-0.08 M) have thicker Pt deposits but their active surface areas and hydrogen sensitivities were lower than those of the 0.01 M KBH<sub>4</sub> electrode. The SEM image (figure 5.4) shows the increasing amount of porosity resulting from the decreasing reductant concentrations, which was achieved in the case of the 0.006 and 0.008 M KBH<sub>4</sub> samples. The effective electrode area is sensitively varied by the amount of the reducing agent rather than the amount of  $[\text{Pt}(\text{NH}_3)_4]^{2+}$  ions. When the amount of the Pt(NH<sub>3</sub>)<sub>4</sub>Cl<sub>2</sub> solution was varied within the range 0.001-0.1 M with a fixed value of KBH<sub>4</sub> solution (0.04 M), the charging current values were in the range 0.07–1.2  $\mu\text{A}$ . But, when the amount of reducing KBH<sub>4</sub> solution was changed within the range 0.01-0.08 M while that of the Pt(NH<sub>3</sub>)<sub>4</sub>Cl<sub>2</sub> solution was fixed at 0.01 M, the current was observed to be in a higher range of 0.05-0.3  $\mu\text{A}$ . This shows that compared to the ion-exchange step, the reduction conditions have larger effects on the microstructure of the resulting electrodes.

The response time ( $t_{90}$ ) was typically less than 10–30 s. Figure 5.35 shows the results of cyclic exposure of the Pt | Nafion sensor element to 50 ppm hydrogen and hydrogen free gas. Identical maximum output currents were observed for several cycles changing within one minute from 0 to 50 ppm hydrogen. The diagram shows that the sensor remains stable over a substantial number of cycles. The electrodes prepared with different concentrations of both Pt metal salt and reductant deposited in various electrode thicknesses and their sensitivity to 10 ppm H<sub>2</sub> are listed in Table 5.5. Even though the electrode thickness increases by varying the reductant

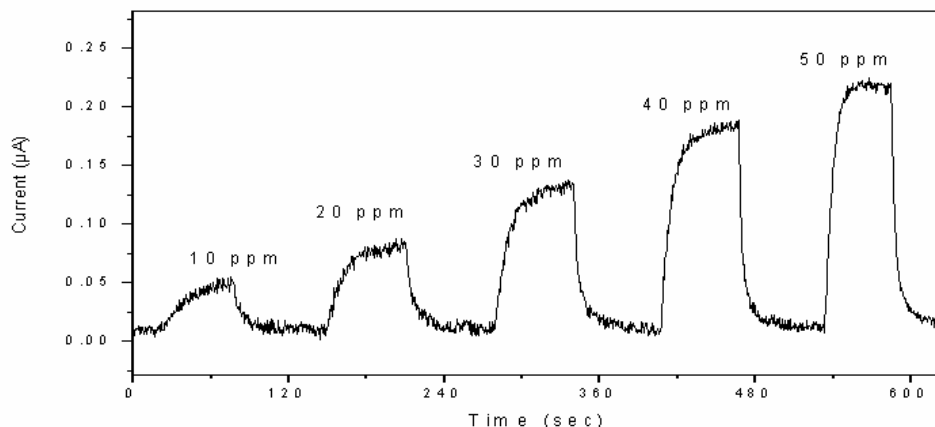


Figure 5.33: Response behaviour of the Pt | Nafion electrode sensor element with an area of  $2 \text{ cm}^2$  prepared from  $0.01 \text{ M Pt}(\text{NH}_3)_4\text{Cl}_2$  and  $0.01 \text{ M KBH}_4$  for hydrogen gas in the low concentration range of 10-50 ppm.

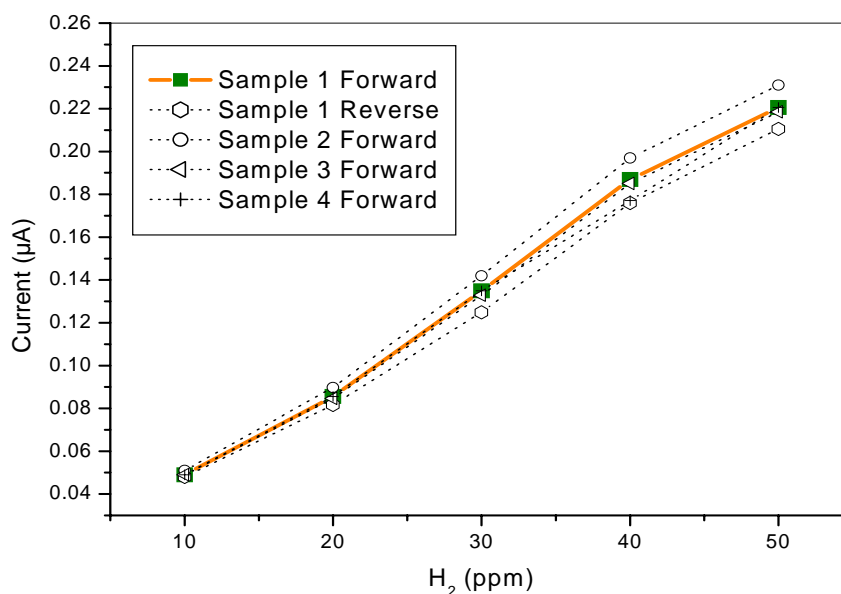


Figure 5.34: Linear relation for  $0.01 \text{ M KBH}_4$  concentration over a low level of hydrogen concentration (10-50 ppm) and a sensing area of  $2 \text{ cm}^2$ . The dotted lines are results from calibrations with different samples.

Table 5.4: A list of average maximum sensitivities of two different sensors in detection range from percentage to ppm level.

Reductant	Detection range	Avg. Max. Sensitivity ( $\mu\text{A cm}^{-2}\text{ppm}^{-1}$ )
0.04 M $\text{NaBH}_4$	1-2%	0.01
	3-7%	0.007
	8-10%	0.008
0.01 M $\text{KBH}_4$	10-50 ppm	0.0046
	100-1000 ppm	0.0026

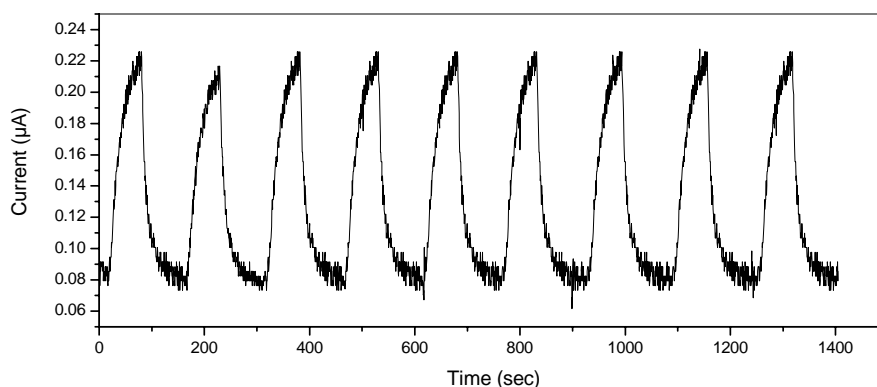


Figure 5.35: Cyclic behaviour of 50 ppm hydrogen and pure nitrogen gas exposure to the sensor element Pt | Nafion<sup>®</sup> with an electrode area of 2 cm<sup>2</sup> prepared from 0.01 M  $\text{Pt}(\text{NH}_3)_4\text{Cl}_2$  and 0.01 M  $\text{KBH}_4$  at one minute time intervals.

Table 5.5: Electrode characterizations and hydrogen sensitivities of the Pt|Nafion electrodes.

Metal salt concentration (Mole)	Reductant concentration (Mole)	Electrode Thickness ( $\mu\text{m}$ )	H <sub>2</sub> Sensitivity (10 ppm) ( $\mu\text{A}$ )
0.001	0.04	0.36	0.012
0.1	0.04	2.10	0.030
0.01	0.006	0.15	-
0.01	0.008	0.20	0.023
0.01	0.01	0.30	0.050
0.01	0.02	0.46	0.031
0.01	0.04	0.62	0.008

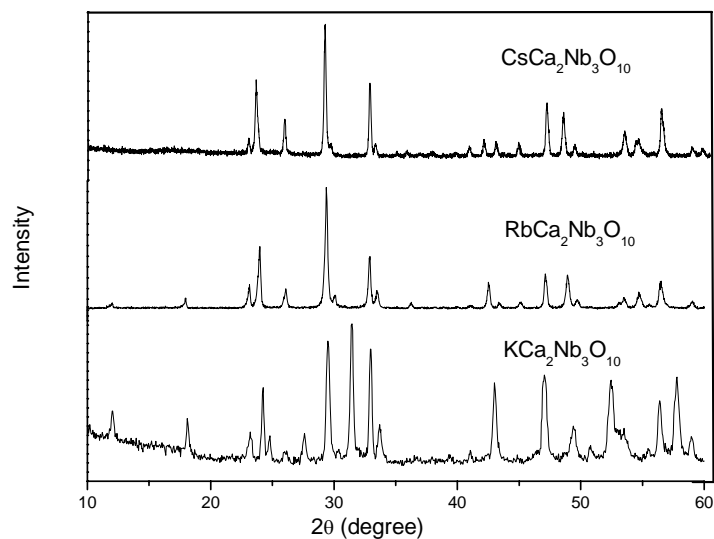


Figure 5.36: X-ray diffraction pattern of solid-state sintered layered perovskite powders.

concentration, the maximum sensitivity was obtained for the 0.01 M  $\text{KBH}_4$  sample. The responses of the other samples were observed to be non-linear in the low hydrogen partial pressure range. The amount of large pores increases the gas diffusion in the electrode although the increase was not large enough to produce sufficient electronic interparticle contact.



## 5.2 Ceramic based hydrogen sensors: Niobates

This chapter deals with the results of the structure and properties of solid oxide proton conducting layered perovskites based hydrogen sensor performance. This section is subdivided into two part deals with two different D-J phase compounds.

### 5.2.1 XRD structure characterisation of niobates

The crystal structure and particle sizes were analysed by means of X-Ray diffraction. A solid state reaction of alkali carbonate, calcium carbonate and niobium oxide in an appropriate weight ratio together with an excess of alkali carbonate

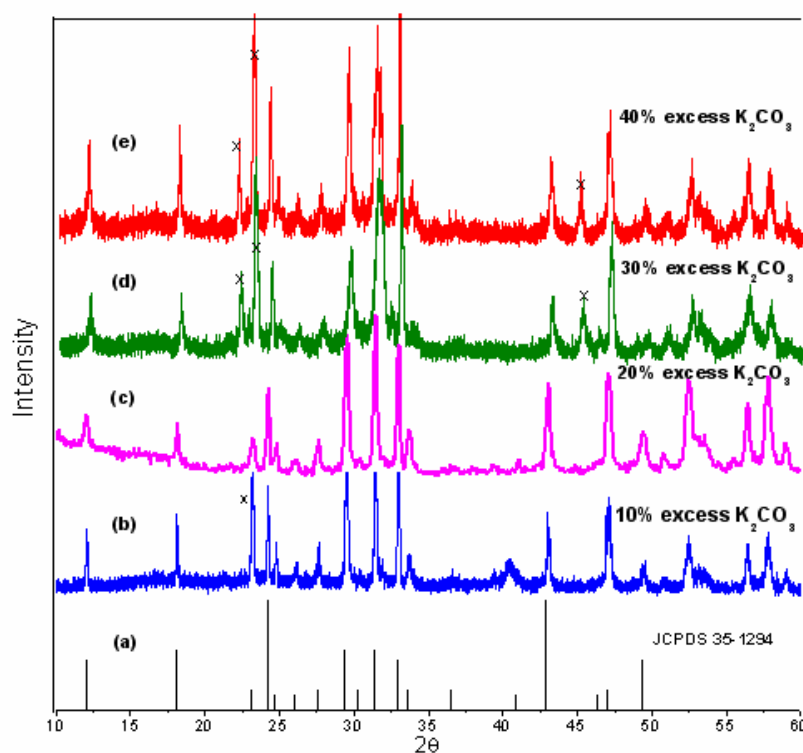


Figure 5.37: X-ray diffraction pattern of layered perovskite  $KCa_2Nb_3O_{10}$  prepared with excess wt. percentage of  $K_2CO_3$  powder (a) JCPDS 04-802, (b) 10%, (c) 20%, (d) 30%, and (e) 40%. (x indicates the presence of impurity or/ second phase).

synthesised the layered perovskite  $[AA'_2M_3O_{10}]$  ( $A = H, Na, K, Rb, Cs$ ;  $A' = Ca$ ;  $M = Nb$ ) at  $1200\text{ }^\circ\text{C}$  in two step sintering for 24 h each. The pure phase formation of corresponding layered perovskite compounds were analysed by powder XRD. Figure 5.36 shows the XRD patterns of D-J phase layered perovskite compounds,

$\text{CsCa}_2\text{Nb}_3\text{O}_{10}$ ,  $\text{RbCa}_2\text{Nb}_3\text{O}_{10}$ , and  $\text{KCa}_2\text{Nb}_3\text{O}_{10}$ . These reflections are consistent with the results for the corresponding niobate compounds [10,11]. All the reflection peaks were well indexed with JCPDS card (35–1294) [12] and assigned to a tetragonal symmetry with  $p4/mmm$  space group. The parent  $\text{RbCa}_2\text{Nb}_3\text{O}_{10}$  compound was found to be a choice for ion exchange reaction due to its fast reaction rate than in the case of the Cs compound. In view of electrical properties, among the D-J phase layered  $\text{A}[\text{A}_2\text{B}_3\text{O}_{10}]$  compounds potassium was reported to have a higher conductivity at low temperature [13]. Further work was focused on the  $\text{KCa}_2\text{Nb}_3\text{O}_{10}$  compound and the effect of excess alkali carbonate was investigated. Figure 5.37 shows the XRD patterns of the layered perovskite  $\text{KCa}_2\text{Nb}_3\text{O}_{10}$  phase prepared with 10–40% excess of  $\text{K}_2\text{CO}_3$ . The bottom panel shows the diffraction angle of the standard JCPDF card (35–1294). Among the samples, the 20%  $\text{K}_2\text{CO}_3$  excess diffraction pattern closely matched with the standard card. Pellets prepared with 30% and more excess of  $\text{K}_2\text{CO}_3$  show a second phase formation of  $\text{KNbO}_3$  which appeared at the angle  $45.11^\circ$ . The absorption of water from the atmosphere was high with excess potassium compound and the pellet become mechanically unstable.

The ability of the D-J phase  $\text{RbCa}_2\text{Nb}_3\text{O}_{10}$  to undergo ion exchange reactions with sodium and hydrogen was investigated. The reaction condition of Na and H varies in time and temperature. The XRD was examined of the dried powder samples in between the total reaction time. Figure 5.38 shows the XRD patterns of ion exchanged D-J phase compounds. The chemical analysis of the product shows the complete replacement of Rb and the compound ratios were close to stoichiometric. The ability to form pellets from the ion exchanged powder was found to be difficult; a poor mechanical stability and is readily solubility in water was seen. In contrast, solid-state synthesised powders contain no structural water, and those were able to press dense and stable pellets. The electroless deposition of the Pt electrode on D-J phase pellets was achieved by the I-R method as described in chapter 4. The I-R method procedures were applied for a dense ceramic pellet and it was observed that the electrode was inhomogeneous. Moreover, as mentioned before D-J phase materials are not stable in water, whereas the samples required to be in contact with the solution for more than an hour in the case of the I-R method. Therefore, the procedure was modified to form a uniform deposition by the M-I-R method. Figure 5.39 shows the GIXRD patterns of  $\text{KCa}_2\text{Nb}_3\text{O}_{10}$  pellet with and without Pt electrode for comparison. The diffraction peak of porous Pt electrode deposited on

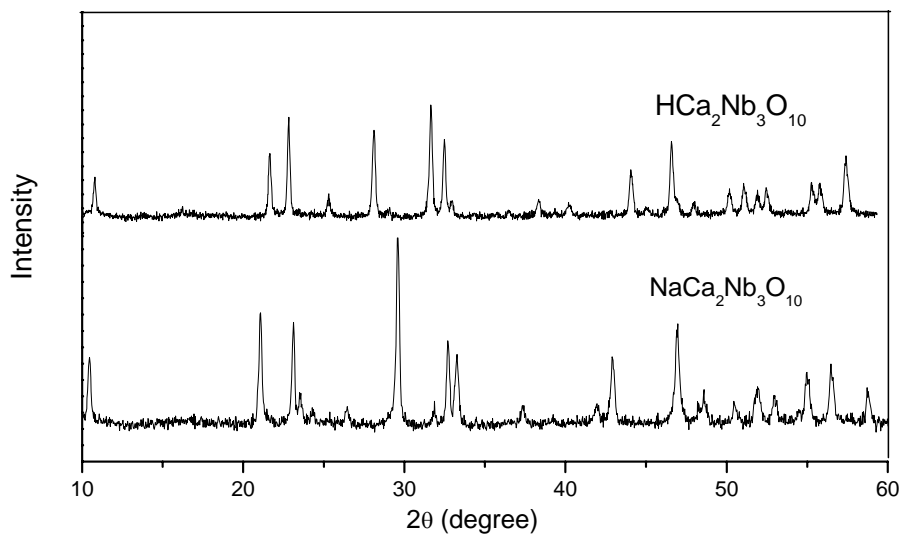


Figure 5.38: XRD patterns of ion exchanged niobates.

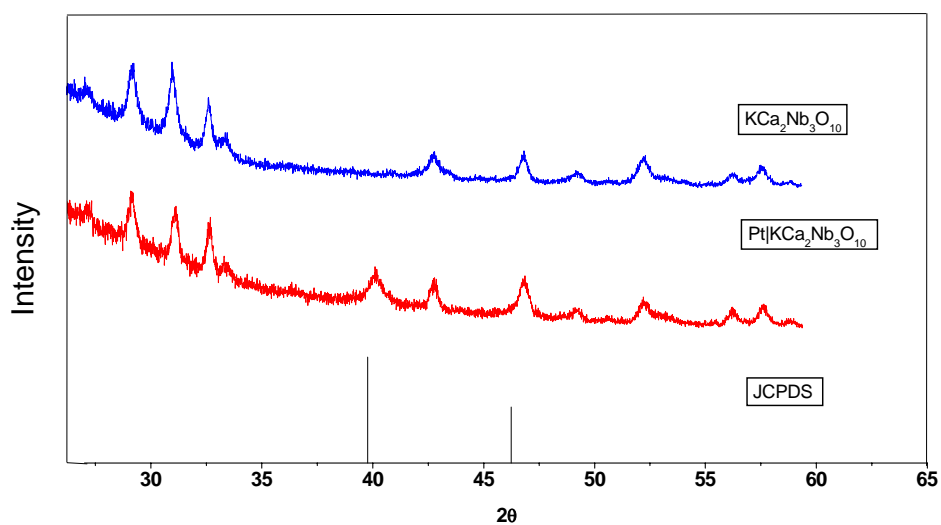


Figure 5.39: GIXRD patterns of niobate pellet with and without chemically deposited Pt electrode.

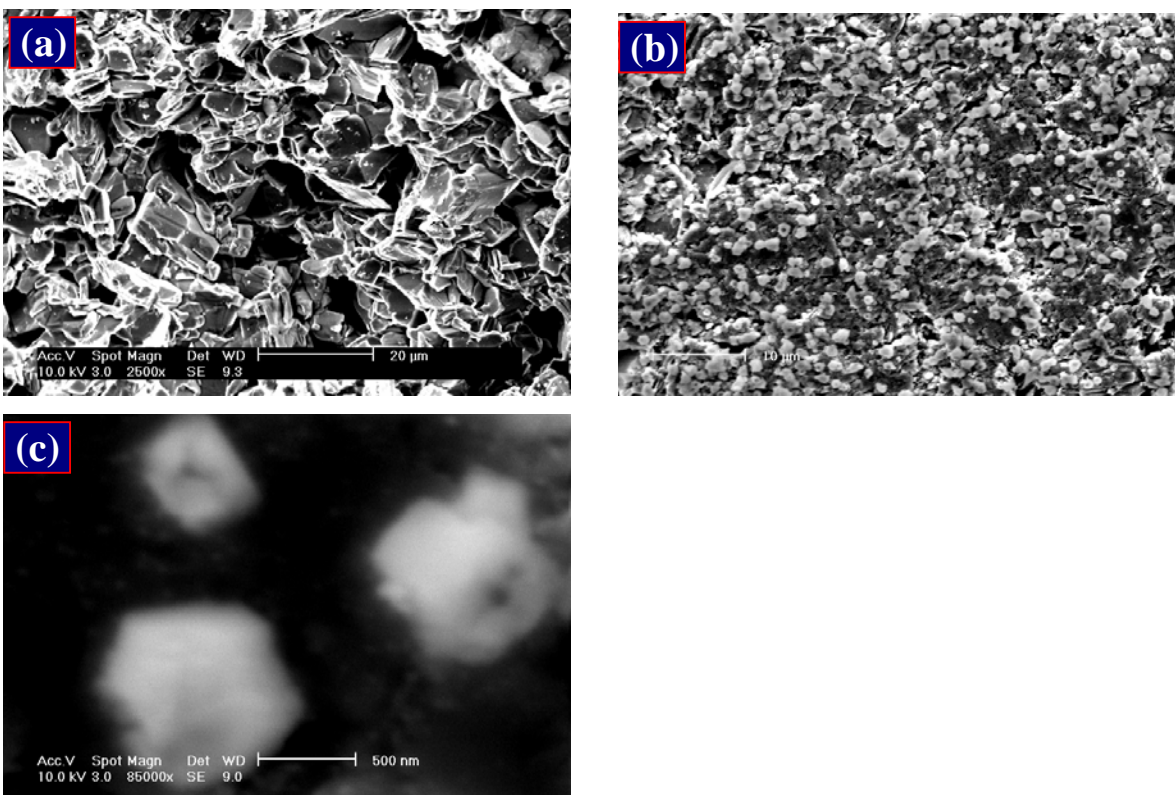


Figure 5.40: SEM photograph of a  $\text{KCa}_2\text{Nb}_3\text{O}_{10}$  pellet sintered at  $1000\text{ }^\circ\text{C}$  (a) fractured surface, (b) Pt particles on polished ceramic surface, and (c) isolated particle at higher magnification.

$\text{KCa}_2\text{Nb}_3\text{O}_{10}$  was observed by GIXRD at an angle of  $39.76^\circ$  which shows the formation of the electrocatalytically active plane (111) on the surface of the solid proton conductor. Electrode formation on ion exchanged samples was not feasible by the method described above.

### 5.2.2 SEM observation on niobates

Layer structured grain morphology of the  $\text{KCa}_2\text{Nb}_3\text{O}_{10}$  sample can be visualised from SEM micrographs on the fracture surface of the compressed pellet as shown in figure 5.40(a). The hydrostatically compressed and sintered pellets ensure that the proton conducting  $\text{KCa}_2\text{Nb}_3\text{O}_{10}$  is highly dense to avoid hydrogen crossover. Thus, electrode depositions were feasible over the layered structured grains at the surface of the pellet. Figures 5.40 (b), (c) show the chemically deposited Pt particles on a polished  $\text{KCa}_2\text{Nb}_3\text{O}_{10}$  surface as prepared by the M-I-R method. The increase in particle size growth was observed by varying the reducing agent concentration. The reductant

concentration of 1 M  $\text{KBH}_4$  was optimised to get a homogeneously and evenly distributed Pt layer around the sample surface as shown in figure 5.40 (b). These porous structured electrodes form Triple Phase Boundary (TPB) junctions which are necessary for good gas sensor performance. The interparticle distance was found to be varying in different parts of the pellet surface. In order to establish good electronic contacts between the Pt particles, a few milligrams of carbon slurry paste were coated along the Pt grains. The grain size of the sample was calculated from X-ray diffraction peaks taken at different grazing incidence angles by using Scherrer's equations. As a result, the grain size was found to be 50, 100, and 500 nm for the samples deposited in 0.1, 0.5, and 1 M  $\text{KBH}_4$ , respectively. The SEM micrographs show good agreement of the calculated size with the observed ones (figure 5.40(c)). The amount of Pt loading on the electrolyte surface was estimated by using cyclic voltammetry and a value of  $1.85 \text{ mg cm}^{-2}$  was obtained for the 1 M  $\text{KBH}_4$  sample.

### 5.2.3 AFM studies on niobate

The polished surface of the  $\text{KCa}_2\text{Nb}_3\text{O}_{10}$  pellet could not be observed with SEM due to the surface charging effect on oxide. The surface roughness of the  $\text{KCa}_2\text{Nb}_3\text{O}_{10}$  was observed with an AFM tip as shown in figure 5.41. The average roughness across the sample surface was estimated to be  $250 \text{ \AA}$  and particle grains were micron thick.

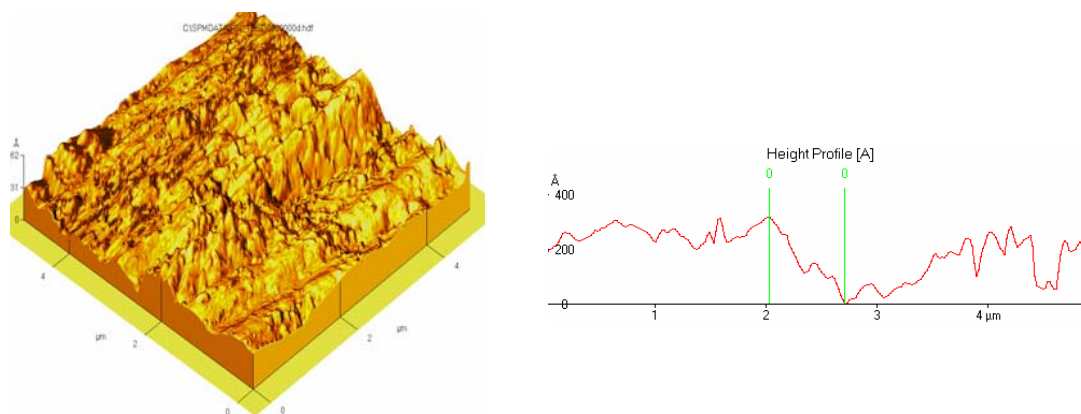


Figure 5.41: AFM image of niobate surface and depth profile.

### 5.2.4 TGA of anhydrous niobate

Thermal analysis (TGA) of  $\text{KCa}_2\text{Nb}_3\text{O}_{10}$  powder samples were carried out at  $2 \text{ }^\circ\text{C}/\text{min}$  heating rate up to  $700 \text{ }^\circ\text{C}$  in air and  $\text{H}_2$  atmospheres. The measurement in air

showed no evidence of weight loss, whereas in hydrogen significant weight losses were observed at 120 °C. The loss of weight is due to the reduction of compound under the reducing gas atmosphere at higher temperatures, it is evident from the colour change in powder after measurement from pale yellow to dark. The structural stability was verified by XRD, and was shown similar patterns for both air and H<sub>2</sub>.

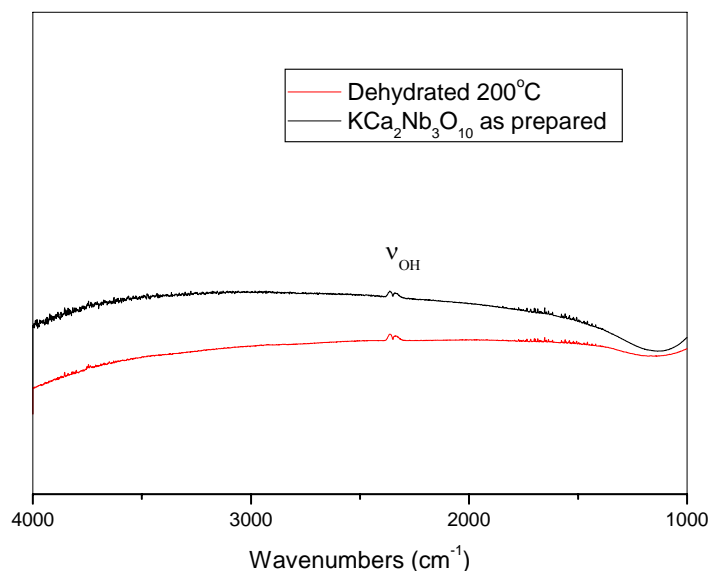


Figure 5.42: FT-IR spectra of anhydrous and dehydrated KCa<sub>2</sub>Nb<sub>3</sub>O<sub>10</sub> powder.

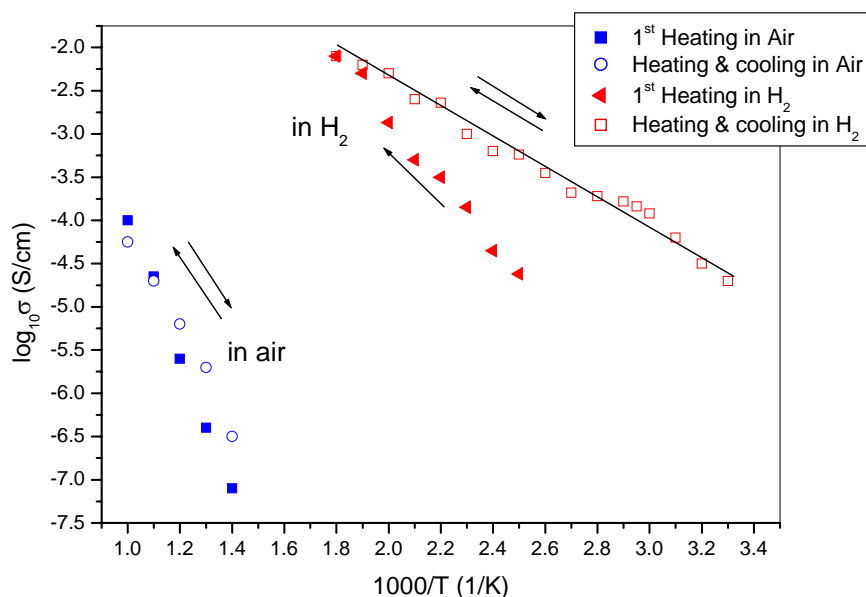


Figure 5.43: Arrhenius plots of proton conductivity of KCa<sub>2</sub>Nb<sub>3</sub>O<sub>10</sub> in air and H<sub>2</sub> containing atmospheres.

### 5.2.5 FTIR spectra of niobates

FTIR absorption spectra of potassium calcium niobate were taken for both the hydrated and dehydrated samples as shown in figure 5.42. They exhibit several bands which were interpreted as stretching vibrations of Nb = O at  $1653\text{ cm}^{-1}$ , and bridging oxygen niobium vibrations within  $2383\text{--}2303\text{ cm}^{-1}$ . The emerging feature is the similarity between the two spectra that contain two main absorption bands.

### 5.2.6 Electrical conductivity of niobates

The electrical properties were examined using the AC impedance method. Series of complex impedance spectra were measured in the temperature range between  $27\text{--}65\text{ }^{\circ}\text{C}$ . Even at room temperature, the sample exhibited a single semicircle in the frequency range from 5 Hz to 13 MHz and no low frequency tail was visible. The equivalent circuit of these spectra was considered as resistance and capacitance in parallel. However, the impedance of the sample obtained in air was high and no semicircle was observed in hydrogen. Figure 5.43 shows the Arrhenius plot obtained from Pt |  $\text{KCa}_2\text{Nb}_3\text{O}_{10}$  | Pt at various temperatures under hydrogen. The electrical conductivity increases sharply in pure hydrogen during the first heating cycle and follows the same line for the subsequent cooling and heating cycles. As a result, the layer structured perovskite  $\text{KCa}_2\text{Nb}_3\text{O}_{10}$  with non-blocking electrodes becomes more ionically conducting in hydrogen atmosphere than in air. Proton conductivity of  $6.3 \times 10^{-5}\text{ Scm}^{-1}$  at  $45\text{ }^{\circ}\text{C}$  was obtained for the layered perovskite of the D-J type  $\text{KCa}_2\text{Nb}_3\text{O}_{10}$  electrolyte. For comparison, the Arrhenius plots of the Rb and Cs niobate compounds are given in figure 5.44 at temperatures  $70\text{--}250\text{ }^{\circ}\text{C}$ . The room temperature conductivity of both compounds were low and even at higher temperatures the potassium niobate exhibit an order of magnitude higher conductivity than the others in the same series.

### 5.2.7 Sensing characteristic of solid oxide ceramic/perovskite based system (niobates)

The sensor property depends on the particle size of the electrode and temperature at which the device was operated. The electrocatalytic Pt electrode was synthesised by three different methods, namely, high temperature curable paste, sputtering, and M-I-R method. The former two methods were found to result in more dense and larger particle sizes than the third one. Table 5.6 show the general characteristic observed in case of the three methods and the sensing current at 4 %  $\text{H}_2$  concentration. Among the other methods, M-I-R shows smaller particles and less current, but more stable

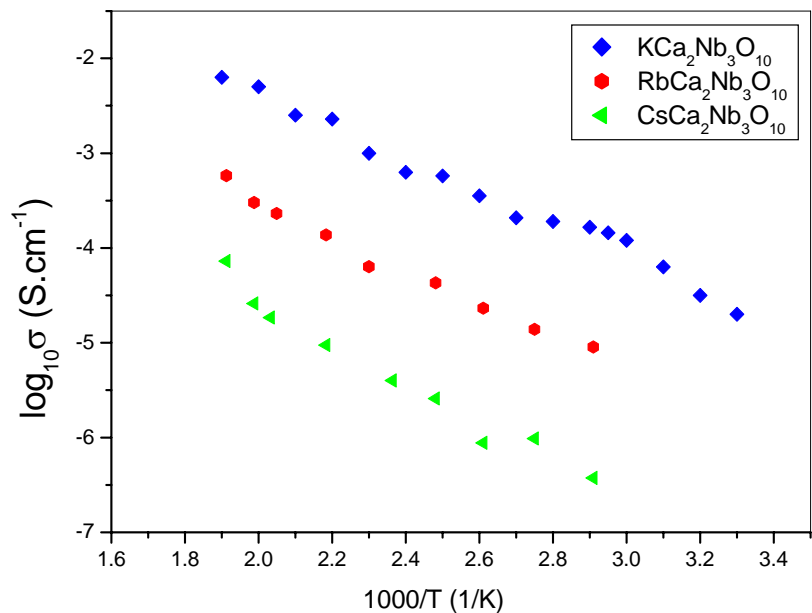


Figure 5.44: Arrhenius comparison plots of D-J phase niobates.

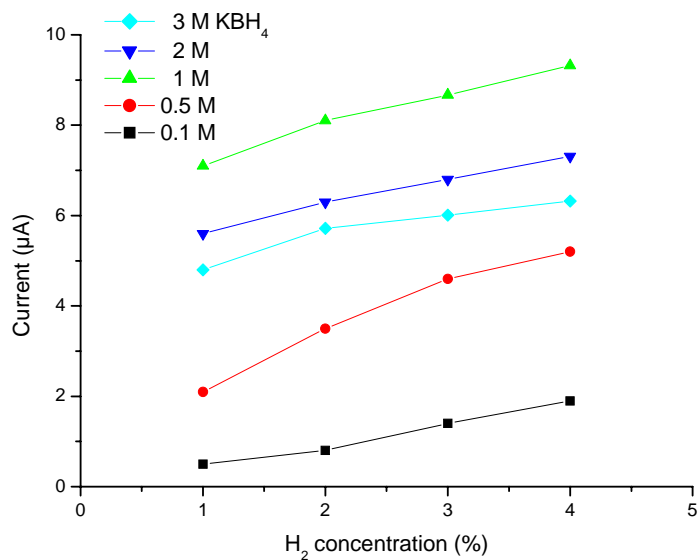


Figure 5.45: Effect of reductant concentrations in sensor response.



films were obtained, whereas sputtered and pasted films peeled off after a long exposure to ambient humid atmosphere. The measurements on hydrogen were performed at or below 4%. Pt electrodes prepared from various concentrations of reductant and measured with hydrogen from 1–4% are shown in figure 5.45. At higher reductant concentration, there was an increase in the size and density of Pt particles. Moreover, further growth of Pt was not shown to have a large improvement in the current because the number of TPB region reduced.

Figure 5.46 shows the typical step response of a  $\text{KCa}_2\text{Nb}_3\text{O}_{10}$  ceramic sensor at different hydrogen concentrations. In this experiment, the hydrogen concentration was initially set at 1%. The concentration was increased by a factor of one in each step until a final concentration of 8% was reached after seven upward steps. Each cycle consisted of 60 s  $\text{H}_2$  exposure and a 120 s carrier gas purge. The sensor exhibited distinguishable response and recovery in each concentration. Figure 5.47 shows the calibration plot over a wide range of  $\text{H}_2$  concentrations. At hydrogen concentration up to 5 % a linear response current was observed and the same in low ppm range (50–1000 ppm). Figure 5.48 shows the response time ( $t_{90}$ ) versus  $\text{H}_2$  concentration in the range 1–8% measured at a temperature of 45 °C. At 4 %  $\text{H}_2$ , the response time for 90% of the saturation current of 9.32  $\mu\text{A}$  was achieved within 5 s and the recovery time was 12 s, including the time for exchanging the atmosphere in the measurement chamber. The observed response of the sensor is rather fast for  $\text{H}_2$  compared with the polymer electrolyte sensor described in section 5.1.9.6. Figure 5.49 shows the response of a sensor that was subjected to a cyclic exposure of hydrogen concentration at 1% and 50 ppm. Each cycle consisted of a 60 s hydrogen mixture followed by 90 s of carrier gas purge. Good stability on hydrogen sensing was observed over a wide range of concentrations.

Figure 5.50 shows a number of sensor responses, each point was obtained from steady-state current values  $I$ , which is plotted versus the  $\text{H}_2$  partial pressure measured at operating temperatures between 25 and 65 °C. The plots show a linear increase in current with increasing  $\text{H}_2$  concentration up to 5%, followed by saturation at higher  $\text{H}_2$  partial pressure. The curves also show that the detection sensitivity increases at higher temperatures. For all cases, the current  $I$  shows a similar trend of increment, but with distinct sensitivity and saturation limits depending on the device operating temperature. The reproducible response was observed for several constant exposures from 1 to 8 %  $\text{H}_2$  and therefore the present sensor exhibits a stable performance.

### 5.3 Ceramic based hydrogen sensors: Tantalates

#### 5.3.1 XRD structure characterisation of tantalates

The XRD patterns of synthesised D-J phase tantalates are shown in figure 5.51. The parent compounds of layered perovskite synthesised by solid-state high temperature reaction, Cs-type and Rb-type tantalates show nearly the same patterns in good agreement with previous works [14]. The ion exchanged H-type tantalate shows a pattern with weaker peaks than Cs and Rb types, implying that perovskite layers were partially delaminated into single layers. It was observed that the formation of

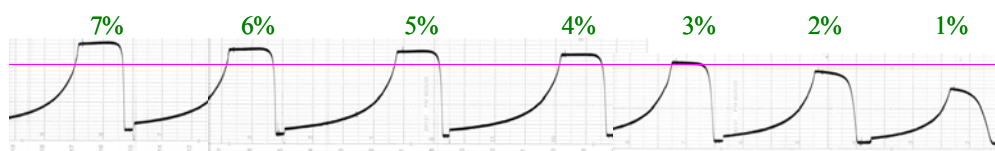


Figure 5.46: Step response behaviour of the chemically reduced Pt |  $\text{KCa}_2\text{Nb}_3\text{O}_{10}$  | Pt sensor element with an area of  $2 \text{ cm}^2$  in 1- 7% hydrogen gas concentration at  $45 \text{ }^\circ\text{C}$ .

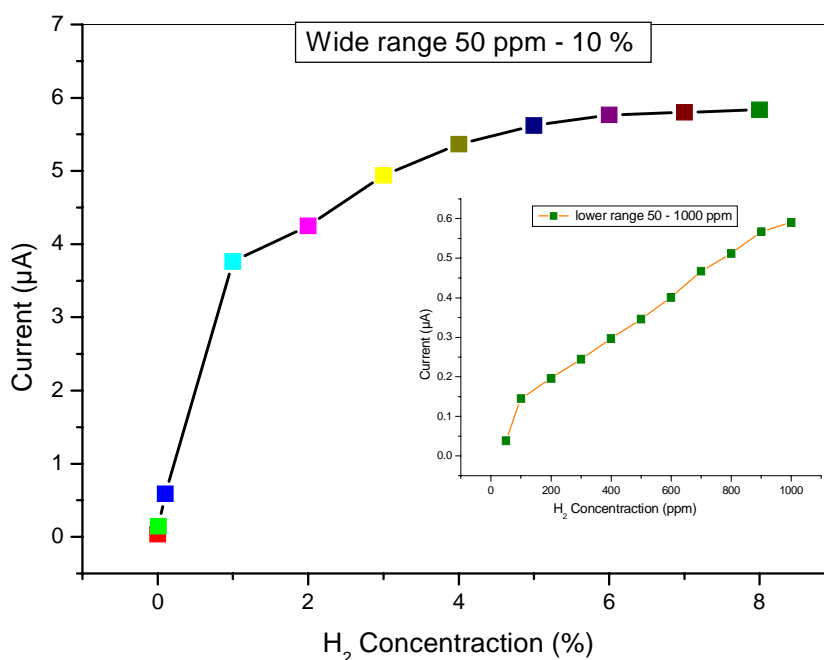
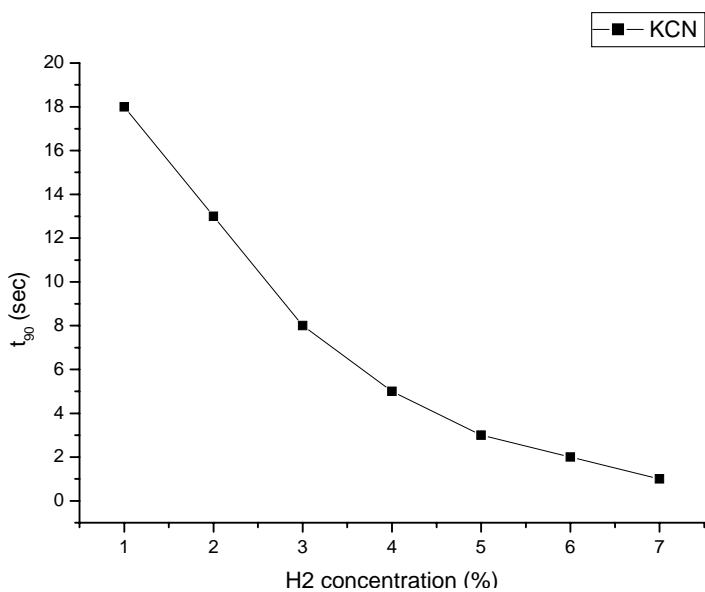
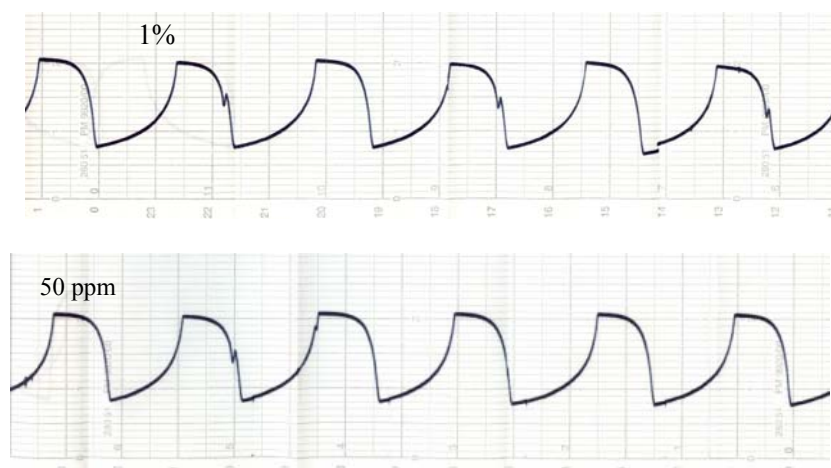


Figure 5.47: A wide range of  $\text{H}_2$  concentration detection with D-J phase  $\text{KCa}_2\text{Nb}_3\text{O}_{10}$  based sensor and a (inlet) low ppm concentration level calibration.

Table 5.6: Properties of electrode deposition methods on ceramic electrolyte.

Method	Porosity	Particle size	Pt loading	Sensitivity
Slurry/paste	Porous	5-10 $\mu$	$\sim 10\text{mg}/\text{cm}^2$	$\sim$ High
Pt sputter	Dense	1-2 $\mu$	$\sim 3\text{mg}/\text{cm}^2$	$\sim$ High
Pt (MIR)	Highly porous	500-100nm	-	5.46 $\mu\text{A}$

Figure 5.48: Response time vs. hydrogen concentration (1-7%) for chemically deposited Pt on  $\text{KCa}_2\text{Nb}_3\text{O}_{10}$  pellet.Figure 5.49: Typical cyclic response of 1% and 50 ppm of H<sub>2</sub> with niobate based sensor.

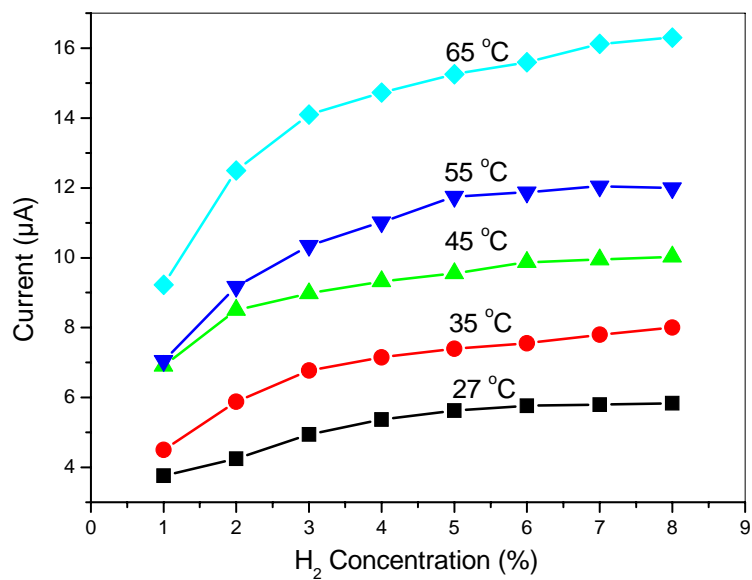


Figure 5.50: Effect of temperature in sensing H<sub>2</sub>.

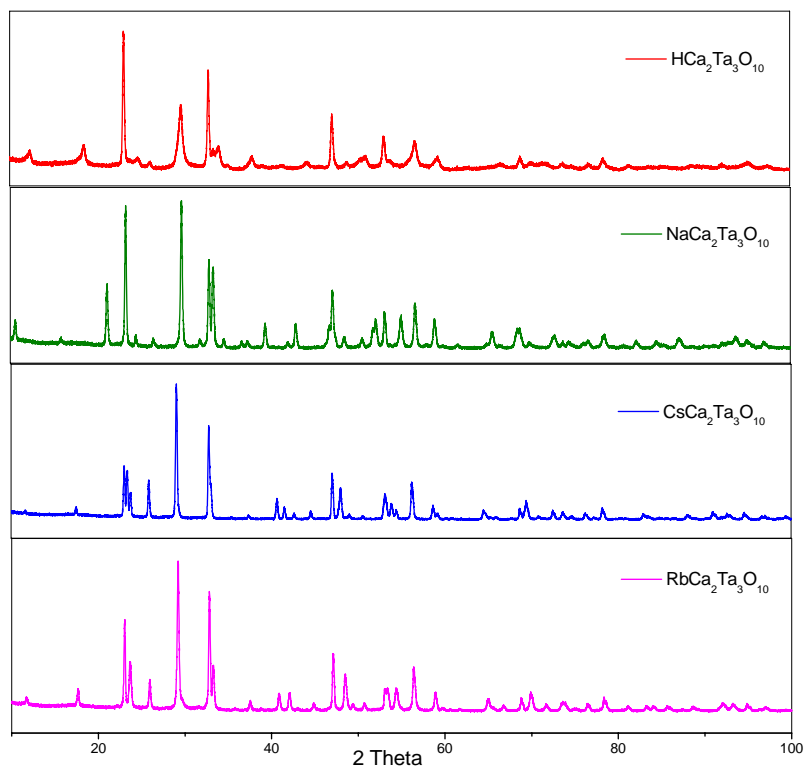


Figure 5.51: XRD patterns of the both solid state synthesised and ion exchanged tantalite powders.

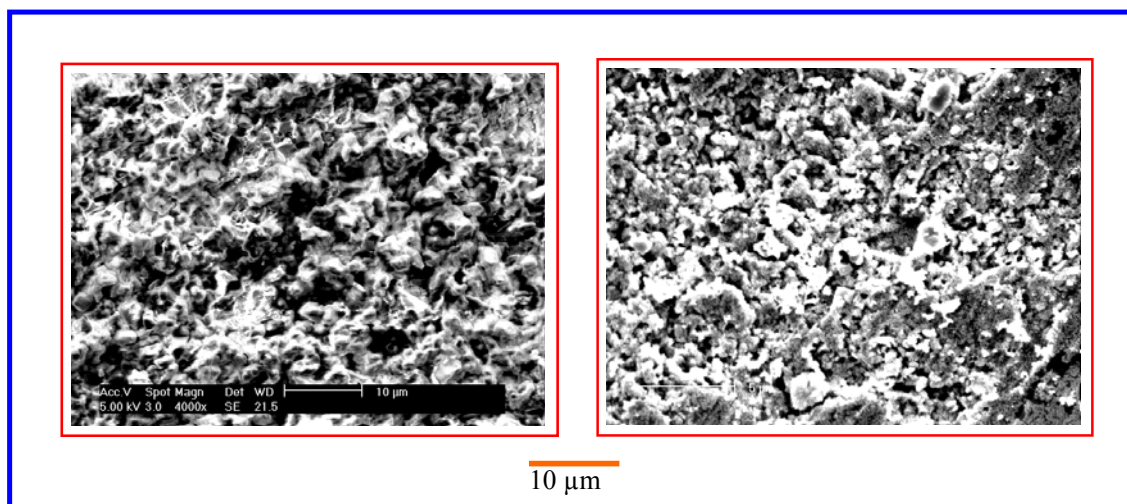


Figure 5.52: SEM photographs of  $\text{HCa}_2\text{Ta}_3\text{O}_{10}$  pellet (a) without Pt and (b) with Pt electrode.

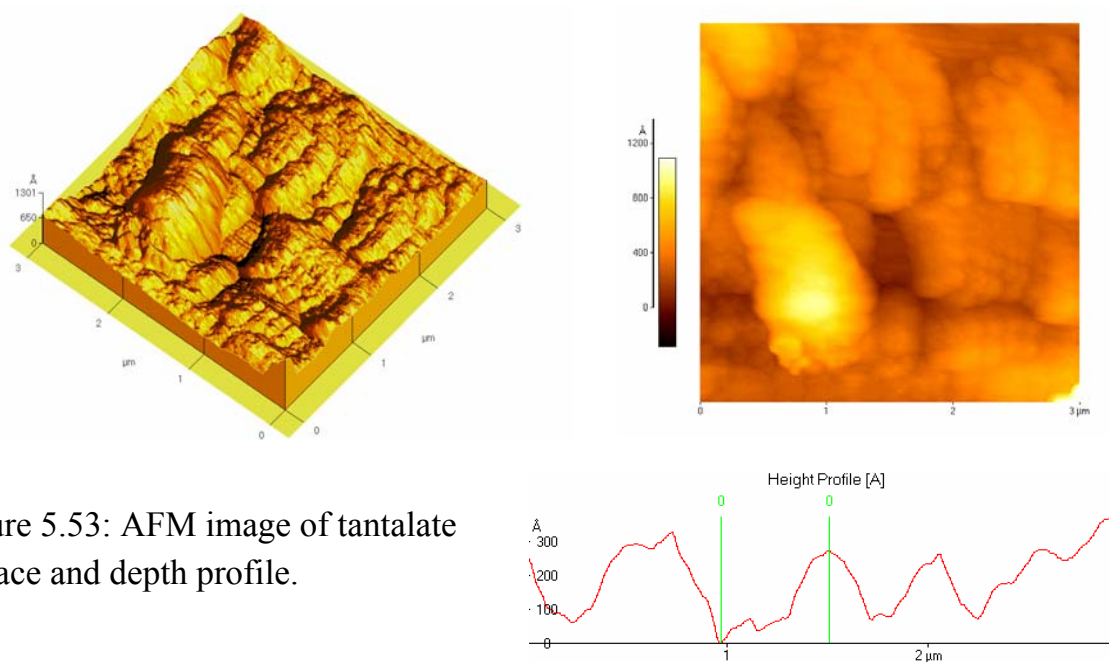


Figure 5.53: AFM image of tantalate surface and depth profile.

H<sub>2</sub>Ca<sub>2</sub>Ta<sub>3</sub>O<sub>10</sub> phase starts after 7 days at room temperature and after carefully washing with water for several times there were no additional phases in the sample. The reflection peak (105) of Na-type shifted toward the smaller angle than that of parent types, corresponding to the expansion of layers from (Rb-type) to (Na-type) due to the increase in size of an intercalated cation. This sodium compound was strongly hygroscopic upon exposure to the atmosphere. The water molecules in the hydrated sodium compound has promoted the intercalation, leading to a large expansion in the interlayer distance.

### *5.3.2 SEM observation on tantalates*

The microstructure of H-type tantalate pellet was investigated by SEM. Figure 5.52 (a) shows a polished surface of H<sub>2</sub>Ca<sub>2</sub>Ta<sub>3</sub>O<sub>10</sub> ion exchanged sample. The compressed pellet surface show that the large distant layer structures were collapsed and inhomogeneous grain sizes occurred. Figure 5.52b shows the chemically reduced Pt surface on H-type tantalate pellet. Due to the deformation in the layer arrangements on H-type tantalate pellet, the nucleation site for Pt growth was observed predominately at the interlayer gap. The deformed layer provided a less and non-uniform site for the formation and growth of Pt particle as shown in figure 5.52. The resulted Pt particles were non uniform and variation in sizes, hence the interparticle distances were differ to establish a proper electronic contact to lead a electrochemical reaction. In order to clarify the stability of the compressed pellet at higher temperature, however no evidence of further changes in layered structures were observed after high temperature electrical measurements.

### *5.3.3 AFM studies on tantalate*

The polished surface of the H-type tantalate could not be observed with SEM due to the surface charging effect on oxide. The surface roughness of the H<sub>2</sub>Ca<sub>2</sub>Ta<sub>3</sub>O<sub>10</sub> was observed in AFM tip show in figure 5.53. The average roughness across sample surface was estimated as 300 Å and cluster of particle grains were less than one micron thick. In contrast with niobates, the particles tend to form clusters and the surface morphology changes when it exposed to moisture.

### *5.3.4 TGA of anhydrous tantalates*

The obtained products were strongly hygroscopic upon exposure to the atmosphere. The TGA curve of anhydrous NaCa<sub>2</sub>Ta<sub>3</sub>O<sub>10</sub> powder samples was obtained under 100% hydrogen atmosphere. The total weight loss up to 190 °C correspond to the 4

wt% of H<sub>2</sub>O molecules. As shown in the TGA plot, the dehydration process takes places several steps of weight loss indicating the presence of structural H<sub>2</sub>O molecules.

### 5.3.5 FTIR spectra of tantalates

Figure 5.54 shows the FTIR spectra of hydrated (anhydrous) and dehydrated samples of D-J phase tantalates prepared from solid-state reaction at high temperatures. Two strong absorption peaks at around 1500 cm<sup>-1</sup> and 3500 cm<sup>-1</sup> were observed, which commonly appear in perovskite proton conductors [15]. There are no significant changes in the absorption peaks in both hydrate and dehydrated phases, implying that the uptake of water onto the structure did not occur. Hydration behaviour of interlayer water was studied after the water treatment on ion exchanged tantalates as shown in figure 5.55. As-prepared Na phase with hydrated interlayer exhibits broad bands due to OH stretching mode ( $\nu_{\text{OH}}$ ) at around 3300 cm<sup>-1</sup> and two sharp bands due to HOH bending mode ( $\delta_{\text{HOH}}$ ) at 1700 and 1650 cm<sup>-1</sup> these bands were minimized after dehydration at 200 °C. A peak appears at 1400 cm<sup>-1</sup> which may be due to H<sub>2</sub>O impurity originating from atmospheric moisture, whereas, H-type compound treated with water shows little evidence of interlayer stretching ( $\nu_{\text{OH}}$ ) or bending modes ( $\delta_{\text{HOH}}$ ).

### 5.3.6 Electrical conductivity of tantalates

Figure 5.56 shows Arrhenius plots of the electrical conductivity of tantalates prepared by solid state and ion exchange reactions. Since the ion-exchanged tantalates are anhydrous, the ability to form a pellet were difficult. Particularly, in the case of Na-type compound it was not possible to measure the electrical conductivity. In contrast, H-type tantalate allowed to make pellets at higher pressures. The electrical conductivities were measured in a Kiel cell arrangement as



Figure 5.56 presents the temperature dependence of the total conductivity in the temperature range from 27°C to 250°C of CsCa<sub>2</sub>Ta<sub>3</sub>O<sub>10</sub>, RbCa<sub>2</sub>Ta<sub>3</sub>O<sub>10</sub> and HCa<sub>2</sub>Ta<sub>3</sub>O<sub>10</sub> samples measured at 4% hydrogen concentration. Among the three successful tantalate compounds H- type shows a higher conductivity than Rb and Cs type. For example, the conductivity of H-type show more than two orders of

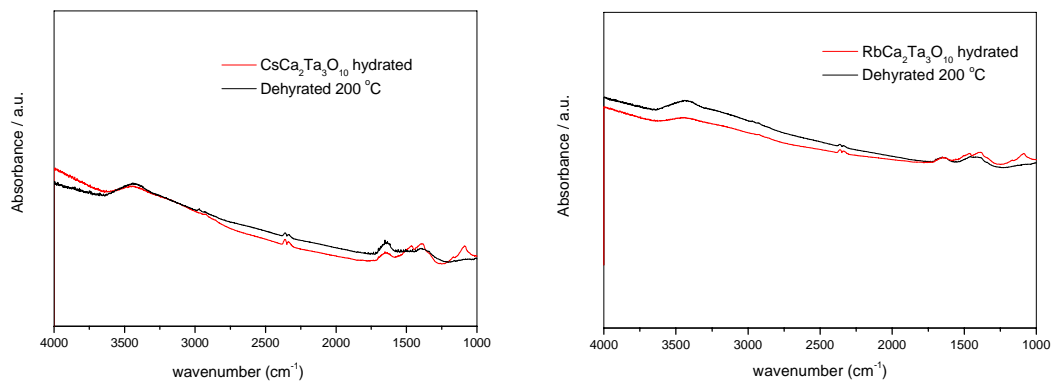


Figure 5.54: FT-IR spectra of solid state sintered anhydrous and dehydrated tantalates powders.

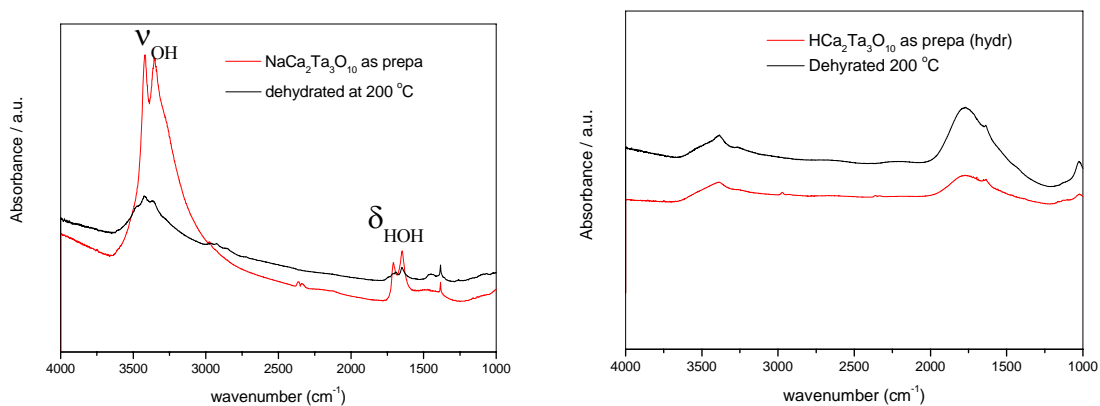


Figure 5.55: FT-IR spectra of ion exchanged by soft chemistry anhydrous and dehydrated tantalates powders.



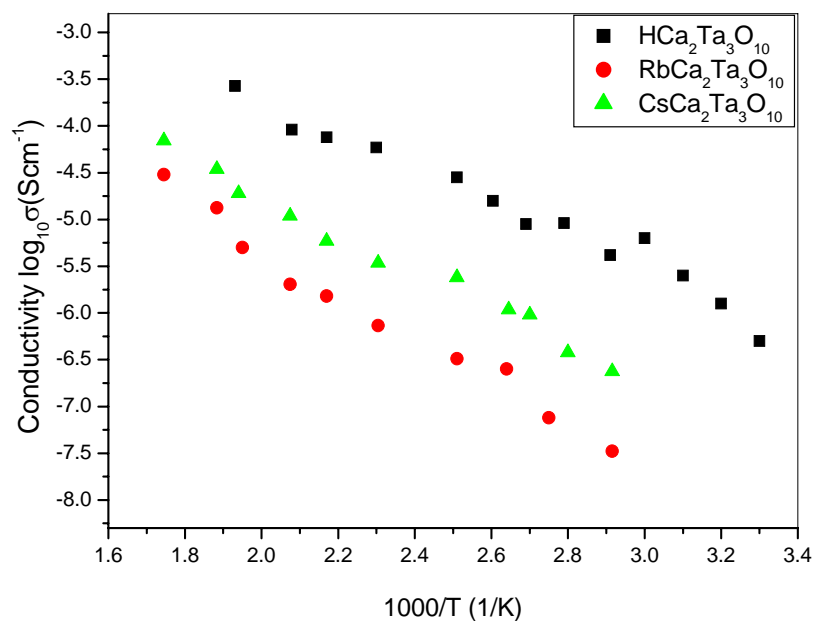


Figure 5.56: Arrhenius plots of three types of D-J phase tantalates.

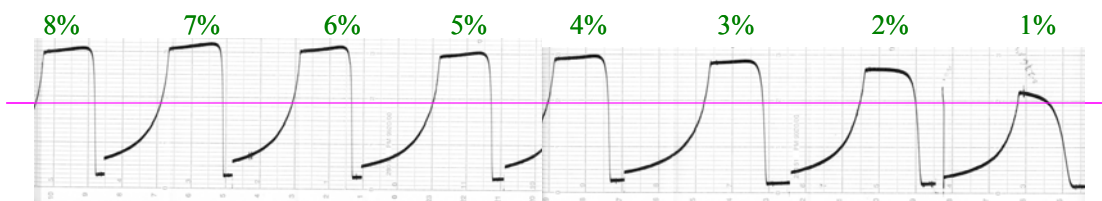


Figure 5.57: Hydrogen gas response behaviour of the chemically deposited Pt on  $\text{HCa}_2\text{Ta}_3\text{O}_{10}$  pellet. The sensor was operated at 60 °C in ambient humidity.

magnitude than Cs-type of  $3.1 \times 10^{-7} \text{ Scm}^{-1}$  to  $5.6 \times 10^{-5} \text{ Scm}^{-1}$  at 70 °C. The conductivities were obtained after the first cycle of heating and cooling. At the first heating cycle the conductivity was low as observed in potassium niobate sample. The conductivity at low temperature could not be measured for the Rb and Cs – compound. The hydrogen sensor measurements were carried out using highest conductivity obtained from H-type tantalate compounds at 45 °C.

### 5.3.7 Sensing characteristic of solid oxide ceramic/perovskite based system (tantalates)

The chemically deposited Pt on layered perovskite H-type tantalate was tested under different hydrogen concentrations. In view of structural stability and higher electrical conductivities among the tantalates, H-type was chosen as a potential candidate for H<sub>2</sub> sensors. Figure 5.57 shows the typical step response of 1–8 % hydrogen in HCa<sub>2</sub>Ta<sub>3</sub>O<sub>10</sub>. The sensor was operated at 60 °C in ambient humidity. The H<sub>2</sub> concentration from 1–3% show a reasonable change in current magnitude but above 4 % H<sub>2</sub> the current was not proportional. A similar current signal output with variable H<sub>2</sub> concentration shows the sensitivity limit of the tantalate above 4%. The reproducibility of the sensing signal was obtained in the lower concentration range 1–3 %, at higher level current was reduced upon exposure of the same concentration for several cycles. The H-type tantalate was tested under hydrogen concentration at low ppm ranges, it was observed that a very low current signal in nanoampere range. Moreover the current signal was disturbed due to the noise from the electronic equipments. Humidified hydrogen gas was used to improve the signal. Due to the hygroscopic nature of the pellet, the volume was expanded and began to break the ceramic glue. Thus, it was not able to measure in wide range of concentration. Thus, it was not possible to measure over a wide range of concentrations. The response time for 90% of the saturation current of 8 μA in 3% H<sub>2</sub> was achieved from 15–25 s and the recovery time was more than 30 s, including the time for exchanging the atmosphere in the measurement chamber.

### References to chapter 5

- [1] J. Halim, F.N. Büchi, O. Haas, M. Stamm and G.G. Scherer, *Electrochim. Acta* **39**[8-9], 1303-1307 (1994)
- [2] W. Jaegermann and D. Schmeisser, *Surf. Sci.* **165**, 143-160 (1986)
- [3] M. Kuhn and J.A. Rodriguez, *J. Catal.* **154**, 355-363 (1995)
- [4] *Lange's Handbook of Chemistry*, 13th ed. McGraw-Hill, New York, Chap. 9 (1985)

- 
- [5] Y. Sone, P. Ekdunge and D. Simonsson, *J. Electrochem. Soc.* **143**, 1254-1259 (1996)
- [6] S.C. Yeo and A. Eisenberg, *J. Appl. Polym. Sci.* **21**, 875-879 (1977)
- [7] J.M. Doña Rodríguez, J.A. Herrera Melián and J. Pérez Peña, *J. Chem. Educ.*, **77**, 1195-1197 (2000)
- [8] G.F.P. Mueller, *Zeitschrift fuer Metallkunde* **53**, 449-53 (1962)
- [9] Z. Samec, F. Opekar and G.J.E.F. Crijins, *Electroanalysis* **7**, 1054-1058 (1995)
- [10] V. Thangadurai, P. Schmid-Beurmann and W. Weppner, *J. Solid State Chem.* **158**[2], 279-289 (2001)
- [11] M.J. Geselbracht, R.I. Walton, E. Cowell, F. Millange and D. O'Hare, *Chem. Mater.* **14**[10], 4343-4349 (2002)
- [12] M. Dion, M. Ganne and M. Tournoux, *Mater. Res. Bull.* **16**[11], 1429-1435 (1981)
- [13] V. Thangadurai and W. Weppner, *J. Mater. Chem.* **11**[2], 636-639 (2001)
- [14] M. Machida, T. Mitsuyama, K. Ikeue, S. Matsushima and M. Arai, *J Phy Chem B*, **109**[16], 7801-7806 (2005)
- [15] P.Colombon, *Proton conductors*, Cambridge university press, Cambridge pp367-375 (1992)



---

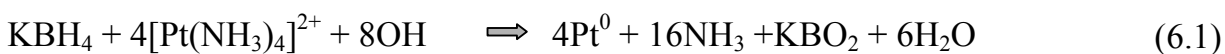
## Chapter 6

### Discussion

#### *6.1 Discussion on polymer based hydrogen sensor*

The particle size estimated from the XRD patterns of Pt film surfaces of two quite different reductant concentrations are well in agreement with optical microscopic observations. The average particle sizes shown in Table 5.2, increase with increasing reductant concentrations. This increase in grain size is believed to be due to higher nucleation growth, when the large amount of reductant is reducing  $[\text{Pt}(\text{NH}_3)_4]^{2+}$  at a faster rate. XRD pattern of both strong and weak reducing agents which show the complete reduction process of metal ions over the Nafion membrane provided with good interfacial contact between the electrode and electrolyte. Lower concentration peaks show larger distortion than in the case of higher concentrations, as well as larger broadening, which is attributed to induced strain between the Pt particles. Smaller particle sizes are expected in the case of broader peaks, in which lower concentrations of  $\text{NaBH}_4$  show larger broadening than  $\text{KBH}_4$  due to the higher reduction rate of the Na compound. Therefore smaller particle sizes are obtained from the Na compound than the K compound, but the formation of large number of TPB is obtained from the K compound sample with its unique porous layer formation. The sensor performance also shows that the K sample is able to detect  $\text{H}_2$  down to ppm level.

The optical micrographs of Pt particles prepared by the T-T method show a decrease in the surface area by the formation of isolated particles even at the higher Pt metal complex concentrations. Moreover, with this method the particles grow bigger and deposit predominantly on top of the previous layer and are not in contact with Nafion. This may be understood from the preparation procedures, that the penetration of both the Pt and reducing agent salt solutions occurs against each other within the membrane structure. The chemistry behind the formation of Pt is considered as follows



Accordingly, a reasonable period of time is required for the metal complex to get exchanged with sulphonic groups within the membrane structure. Upon arrival of the metal salt and reducing agent, the contact sites are simultaneously reduced to Pt metal. Thus, the reduction step is predominant than the metal ion exchange process

within the short period of time. The result is less contact area between Pt and Nafion. On the other hand side, the electrodes have poor contact between the particles which cause high electronic resistance, effective isolation of the deposit and eventually a low surface area.

The unexpected poor electronic conductivity of wet Pt|Nafion MEA is related to as a large micro crack which appears like “dry clay land” structure. Such structures were studied by Shahinpoor et al. [1] for gas sensors and also for the development of artificial muscles [2]. These structures provide only difficulties when the MEAs are operated in fluids, i.e., cyclic voltammogram measurement in 1 M H<sub>2</sub>SO<sub>4</sub> solution. These cracks have no influence on the hydrogen sensing measurements, since the gas diffusion layer of carbon cloth is covering the electrode. This ensures a good electronic junction across the clusters of cracks. It may even occur that in gas sensing such cracks enhance the number of TPB regions. Sensors may not be operated under such extreme wet conditions, e.g. in the case of a large extent to water vapour.

Since the deposition of Pt electrodes occurs by chemical reduction with complex agents, there may be the possibility of the formation of a Pt metal compound, which may affect the electronic structure of the noble metal under humid condition. The possibilities of compound formation are (1) the presence of a sulfonic group in the Nafion structure to form platinum sulphide, (2) the fluoride compound formation from Nafion backbone structure, (3) chloride compound formation from the unreacted metal complex salt, or (4) mere mechanical detachment of the membrane by volume expansion. The uncoated Nafion membrane EDX results show only sulphur, fluorine and carbon peaks, the formation of platinum sulphide and fluoride are high temperature processes and may occur under aggressive conditions such as H<sub>2</sub>S atmospheres [3]. Moreover, since the decomposition of sulphide compound occurs above 800 °C, the recovery of the electrical conductivity of Pt in the dry state at room temperature is not likely. The XPS spectrum of Pt deposited on Nafion after acid treatment shows the pure metal state. Thus, these energy level studies show that the possibility of any compound formation is unlikely. An additional compound formation is reported by Fournier et al. [4] with XPS analysis on a fuel cell Pt electrode prepared by the metal complex salt method at higher temperatures. The formation of microcracks on Pt films may be understood by the volume expansion of the swallowing Nafion membrane. The schematic diagram (figure 6.1) shows the Pt surface structure on Nafion under wet and dry conditions.

As shown in figure 5.8 the membrane under wet condition show substantial amount of volume change which causes strain on the Pt film. Since the electrode

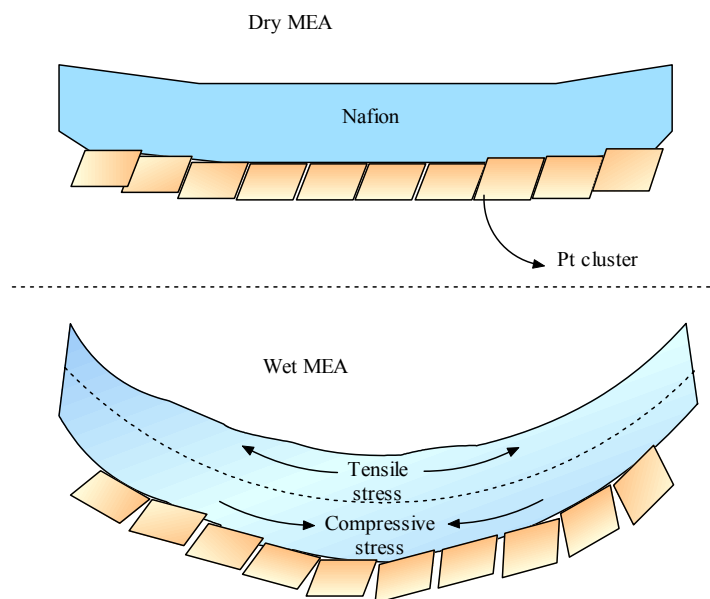


Figure 6.1: The schematic diagram of mechanical model of Pt/Nafion interface under dry and wet conditions.

deposited on the Nafion membrane is restricted in its area, there are two states of forces at volume expansion which act on the bulk of the membrane. The tensile force acts along the subsurface of the membrane while the compressive force acts within the membrane. The metal film surface tends to stretch along the grains as shown in figure 6.1. The shallow shape of micro cracks emphasizes that the film is under tension.

In the cross section image, it was observed that the Pt particle distribution from room temperature prepared surface is more porous and the one prepared at higher temperature extends deeper into the membrane. This may be explained by the formation of Pt nucleation sites shortly after contacting the reductant with the impregnated metal ions within the Nafion membrane by chemical reduction. As the particles increase in size, the growth mechanism of the particles and their clustering is expected to occur predominantly as an electroless reaction. Particles deposited deeply within the membrane do not contact the current collector and do not contribute to the electrochemical reaction. Moreover, the prime requirement for gas sensors i.e., TPB region is lost. To increase the efficiency of production it is necessary to minimize the number of these isolated particles. The dense and thick film formation at the beginning may affect the deposit due to the diffusional limitation of the

reactant through the Nafion. Alternatively, the diffusional process is controlled by the nonequilibrium I-R method developed by Liu et al. [5] as shown by cross sectional TEM images.

The SEM images of the Pt particles deposited onto the Nafion membrane show different crystallite sizes, which is in agreement with the sizes calculated from XRD peak analysis. The images of the surfaces observed for the highest reductant concentration show thick layers of Pt fully covering the electrolyte surface. This coverage is believed to be less suitable for sensor applications, in which the TPB region is of primary importance. The higher the reduction rate, the more strain and particle growth is observed. Lower reductant concentrations show less strain and slow growth rate, resulting in poor interparticle contact. This phenomenon can be understood by considering insufficient reduction time at low reductant concentration to reduce all  $[\text{Pt}(\text{NH}_3)_4]^{2+}$  ions. The SEM investigations confirmed the tendency of decrease in particle size and increase in porosity with increasing reductant concentration.

Figures 5.14 and 5.15 show the dependence of the conductivity of Nafion 117 on humidity and temperature, respectively. The conductivity of this membrane depends strongly on humidity and slightly on temperature in the region of 27 and 50 °C. The proton conductivity in Nafion 117 derived from the AC impedance method was almost consistent with that reported for Nafion 117 [6]. The proton conductivity of Nafion 117 is somewhat higher than that of the other membranes. The proton conductivity of Nafion 112 is a much lower than that of Nafion 117 and 115. It may be inferred that the nominal thickness of each membrane caused the difference in the proton conductivity, as a thicker membrane can retain water in a fully hydrated state for a substantial period of time. The proton conductivity of chemically reduced MEA increases continuously up to  $0.04 \text{ Scm}^{-1}$  at 65 °C. At higher temperatures, although the proton conductivity of chemically reduced MEA is lower than that of Pt/C powder MEA under the same measurement conditions, their conductivity is higher at lower temperatures. Above 65 °C, a drastic change in the proton conductivity in film type MEA is observed because of the high vaporization rate of water from the Nafion membrane under this water-vapour condition. The temperature dependence of conductivity on three different MEAs can be described as follows.

The variation in conductivity may be due to the level of water retention within the Nafion and the rate of vaporisation of water is facilitated through the electrode structures. In the case of film type MEAs, i.e., chemically reduced and sputtered Pt film electrode, the conductivity behaviour is the same at both higher and lower



temperatures. Although the sputtered film electrode show less proton conduction than the chemically reduced film, the trend is the same. The water transport and retention may be rate limited by the sputtered thick films, whereas a substantial amount of TBP regions are observed where the transport is easier and faster in the case of chemically reduced electrodes. This is also proposed in two different models in chapter 3. The loss of water due to vaporisation is rate determined at higher temperatures, and causes the deviation above 65 °C. In the case of bulk Pt powder MEAs, the permeation of water vapour through the gas diffusion layer is the rate limited process at lower temperatures. The same accelerates at higher temperatures as seen by an increase in conductivity. The water content in the membrane significantly affects the proton transport via the Grötthuss hopping mechanism and vehicle mechanism. In this mechanism, the proton which forms an  $\text{H}_3\text{O}^+$  ion, jumps to the neighbouring lonepair electrons of a water molecule. For such a mechanism, the activation energy for proton conductor was about 0.16 to 0.4 eV [7]. The values obtained in this work are generally much smaller. One explanation could be that the measured membrane is fully exposed to the atmosphere. At a higher temperature, the membrane keeps less water, and this decrease in water content causes a lower conductivity.

As noted above, the proton conductivity depends highly on the relative humidity. For a relative humidity of less than 50%, the conductivity decreased drastically. Further, with a RH less than 20%, Nafion 117 behaved like an insulator, indicating the absence of proton migration in Nafion without sufficient hydration. A report [8] on water uptake from the vapour phase calculation indicates that at least two water molecules per sulfonic unit are required for proton conduction.

The selection of electrode materials are made with three different methods of Pt metal deposition. The non-linear response behaviour of sputtered Pt shows that either the sensing electrode or the electrolyte is rate limiting. This behaviour may be due to the slow diffusion of  $\text{H}_2$  into the completely covering platinum film and the next higher concentration is reached comparatively fast. The sensor performance of sputtered Pt film shows a very low magnitude of current output compared to the others. This may be understood by the following: (i) thick films have a lower TPB length, (ii) improper electrode-electrolyte interfaces are established at the electronic junctions, (iii) resistance of the electrolyte may be reduced by dehydration under vacuum environment. The sensor performance observed with GDE electrodes shows a much higher current than the sputtered electrode but a lower one than with the chemically reduced electrodes. The increase in current may be due to the individual Pt particles which are embedded in the carbon matrix providing a large surface area

with a decrease in the formation of electronic junctions at the electrode/electrolyte interface. An extended junction is established by increasing the protonic binder (Nafion solution) loading, which may promote the proton transport (see figure 3.1) but at the same time increases the electrode resistance. The retention of water within the thin layer of the extended junctions may not be long enough to transport the protons.

The sensor response results obtained for the cell configuration with and without GDL show variations in the time and maximum sensitivity current. This indicates that the gas sensors are greatly influenced by the cell construction. Both the configurations show highly reproducible and stable current outputs. The cell with GDL requires to optimise the electrode particle morphology i.e., the size of carbon granules used in GDL may promote/suppress the electrochemical reaction at the TPB regions. This can be understood by the schematic diagram of Pt particle and carbon interface model as shown in figure 6.2.

The optical observations show that the 0.04 M NaBH<sub>4</sub> reductant forms fairly thick particles with less TPB, whereas 0.01 M with smaller particles provides a large number of TPB sites. The smaller size of carbon granules may occupy the interparticle regions and hinder the hydrogen dissociation process. As shown in figure 6.2(a) the hydrogen gas can permeate through the space between Pt and the carbon particles which shows a fast response and higher current, whereas in figure 6.2(b) carbon particles block the TPB regions and the mass transport becomes rate limiting. Mercedes et. al. [9] studied the intercalation of hydrogen in carbon structures, however hydrogen gas may permeate through the carbon particles. It is an additional rate limiting process, which is not preferable for sensor purposes. Whereas the cell configuration with fabric carbon (figure 6.2(c)) provides a substantial amount of gap for H<sub>2</sub> to reach the TPB region and also serves as a current collector by providing an appropriate diffusion transport.

Among the chemically reduced Pt on Nafion with both weak and strong reducing agents the sensor response compared with the sensors prepared by using NaBH<sub>4</sub>, a linear response was observed for hydrogen gas concentrations at the percentage level, whereas in the case of the sensor prepared by using KBH<sub>4</sub>, the linear response was extended down to the ppm level. This behaviour of different types of reducing agent can be explained by the achievement of the high effective electrode surface area via the porous structure. The electrochemical oxidation of hydrogen takes place along the three-phase boundary sites, where the Pt catalyst, solid electrolyte Nafion and H<sub>2</sub> gas come together, which was observed largely in the

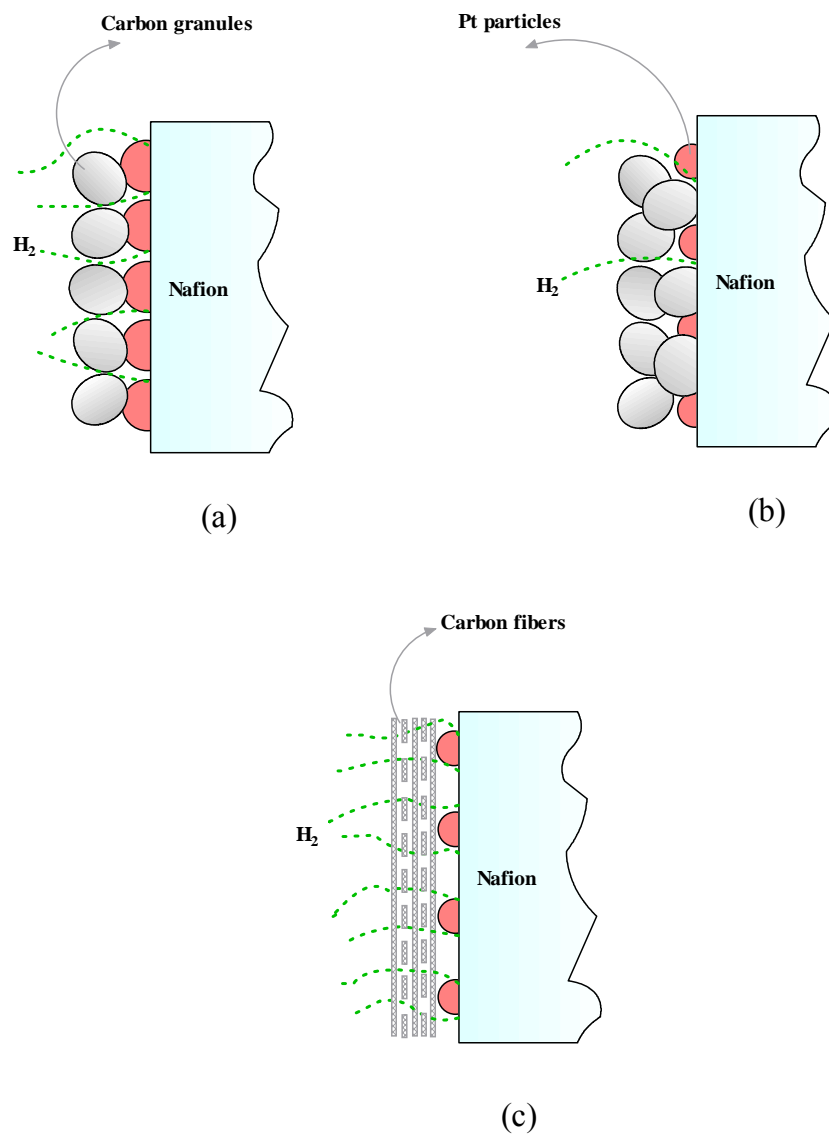


Figure 6.2: The schematic diagram of interface of Pt particle and carbon arranged in (a) orderly, (b) randomly, and (c) aligned fibers.

case of  $\text{KBH}_4$  samples. The porous structure obtained in  $\text{KBH}_4$  samples is a major advantage for very low concentration level detection. The small and uniform pore size structure provides more three-phase boundary sites and shorter diffusion lengths for the electrochemical oxidation to occur. The sensor signal response and recovery time decrease with increasing hydrogen concentration. The amount of the water generation is increased with increasing hydrogen concentration and thus the measuring sensitivity is gradually improved. The response behaviour may be further understood by the microscopic informations of the Pt surface. By assuming the Pt particles are semi-spherical in shape and homogeneous in size, the radius of the particles is equal to the diffusion length  $L$  of the protons, and it may be related to the response time according to:

$$\tau = \frac{L^2}{2D_{\text{H}^+}} \quad (6.2)$$

According to figure 3.8, based on model 1 (bulk diffusion), the response time  $\tau_b$  of proton diffusion through the Pt particle is 5 s by considering that the diffusion coefficient of the protons  $D_{\text{H}^+}$  in Pt is  $10^{-9} \text{ cm}^2/\text{s}$  [10]. In contrast, based on model 2 (surface diffusion),  $D_{\text{H}^+}$  in Nafion at 27 °C is  $10^{-6} \text{ cm}^2/\text{s}$  [11], and thus the response time  $\tau_s$  of proton diffusion along the electrode/membrane interface is 5 ms. According to eq. (3), the calculated  $D_{\text{H}^+}$  in Nafion at 27 °C is  $10^{-7} \text{ cm}^2/\text{s}$  for 1 M  $\text{H}_2\text{SO}_4$  concentration and the proton conductivity in Nafion is  $10^{-2} \text{ S cm}^{-2}$ . There is one order of magnitude difference which may be due to the presence of fluorine groups in the membrane which has not been taken into account. Since the response time  $\tau_2$  is three orders of magnitude faster than what is expected from model 1, it may be assumed that diffusion of hydrogen along the surface of Pt is faster than the diffusion of hydrogen along the Pt electrode/polymer membrane interface. The surface of Pt is always covered with hydrogen gas and the gas may supply a sufficient amount of hydrogen which is consumed at the TPB. Thus the concentration of hydrogen species arriving at the Pt electrode/polymer membrane interface for the charge transfer reaction is related to the surface diffusion rates and surface coverage [12].

The cyclic response behaviour shows that the sensor remains stable over a substantial number of cycles due to the fast and reproducible redox processes at the Pt electrodes.

### 6.2 Discussion on ceramic based hydrogen sensors: Niobates

The schematic figure 6.3 shows the model of gas interaction with the isolated platinum particle on layered perovskite niobate. In a first approach, the particles were assumed to be spherical and uniform in shape. SEM micrographs of Pt particle show

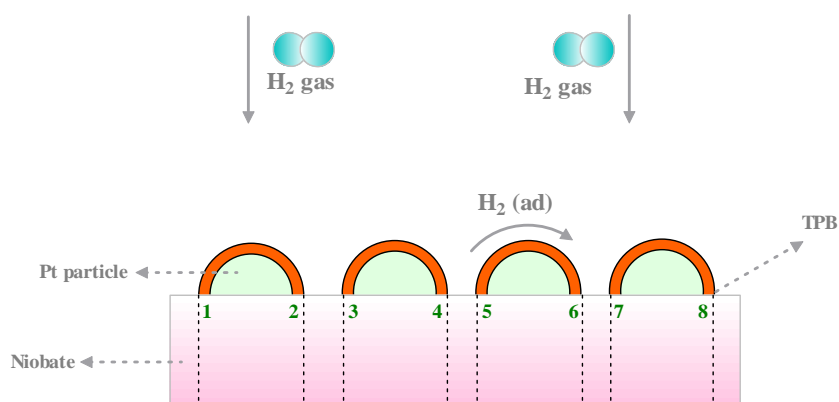


Figure 6.3: The schematic illustration of Pt particles and gas interaction on niobate surface.

nearly spherical shape in top angle view. From the microscopic point of view nearly uniform particle sizes are deposited on the layered perovskite compared to Nafion membrane. Thus, the dissociative adsorption of H<sub>2</sub> molecules at the surface of Pt may occur at the same rate. The rate of charged species diffusion along the surface or bulk path may be the same for all particles. The fractured surface of niobate reveals the layered structures of grain arrangements, the nucleation site for Pt deposition may be preferred on the orientated layers. A large number of TPB regions are established with the oriented Pt growth on layered perovskite niobate. The vibrational spectrum of KCa<sub>2</sub>Nb<sub>3</sub>O<sub>10</sub> show the presence of a small fraction of structural OH groups which may contribute to the ionic conduction.

Proton conductivity in Pt is commonly understood by assuming point defects according to the following defect equations which may read in the case of KCa<sub>2</sub>Nb<sub>3</sub>O<sub>10</sub> under hydrogen atmosphere as follows:



where  $V_o^{**}$ ,  $O_o^x$ ,  $e'$ ,  $h^*$ ,  $H^*$ ,  $OH_o^*$ ,  $H_K^*$ , and  $H_i^*$  represent oxygen vacancy, lattice oxygen, excess electron, hole, proton, proton attached to lattice oxygen, proton at a vacant K site in the lattice, and interstitial proton, respectively. The proton conductivity mechanism in 3D acceptor-doped 3D perovskite oxides due to migration of hydroxyl ions or protons has been described in detail [13]. Formulawise, the  $KCa_2Nb_3O_{10}$  layered perovskite contains neither oxygen vacancies nor structural protons nor water, but behaves simultaneously as electrolyte.

Similar changes in proton conductivity as a function of different ammonia concentrations in layered type perovskite oxides have been described [14]. The difference in conductivity between first heating and further thermal cycles were first observed by Thangadurai et. al with the same group of layered perovskites [15]. A large proton transport at higher concentrations may result during increased polarization, e.g., due to the oxidation process at the cathode side. Subsequently, the formation of a reducing atmosphere changes the oxygen stoichiometry of the perovskite oxide layer at the cathode surface. It is believed that the depletion of lattice oxygen may have caused the non-linear behaviour at higher concentrations, i.e. a contribution from lattice oxygen to the proton conduction mechanism is essential as described by the defect equations (1) and (4). Therefore, it is reasonable that the lattice oxygen is seriously influenced when the oxygen concentration becomes insufficient. For comparison, in terms of the chemically obtained electrode performance, a thin film of Pt electrode was prepared from Pt paste which shows a higher magnitude of the current but requires high temperature curing.

The response time upon changes of the hydrogen partial pressure in the gas depends strongly on the size of the platinum particles on the surface of the layered perovskite solid electrolyte and accordingly on the size of the common interface. The faster response time observed in layered perovskite compared to the polymer membrane sensor may be due to the following several possible reasons (i) the exchange and ionization of hydrogen established the redox equilibrium or thermodynamic equilibrium, (ii) the presence of isolated, smaller particles established a TPB region, to promote the redox process continuously, (iii) the smaller particle size provides larger surface area, thus the surface hydrogen activity establish by the equilibrium with the gas is significantly faster than the bulk diffusion of hydrogen, (vi) large interparticle distance of small isolated particle establishes a large interface between the platinum electrode and the solid electrolyte, thus the electronic equilibrium achieves a higher or identical voltage drop across the interface.

### 6.3 Discussion on ceramic based hydrogen sensors: Tantalates

The response behaviour of the tantalates differs from that of the niobates. The conductivity of tantalates was lower compared to the niobates. It is also observed that in the case of compounds containing the same alkaline earth ion, the K-compound exhibit a higher conductivity compared to the Rb and Cs compounds. The response time and recovery time was very slow compared with that of the niobate. From the microscopic point of view, the Pt particles deposited on tantalates are not same as in

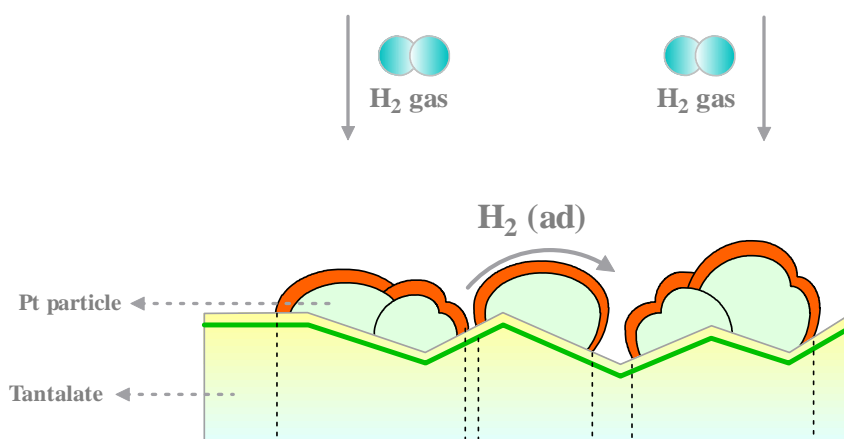


Figure 6.4: The schematic illustration of Pt particles and gas interaction on tantalate surface.

the case of the niobate compounds. The schematic figure 6.4 shows the model of gas interaction with the isolated platinum particle on a layered perovskite oxide. The Pt deposition on layered perovskites is highly influenced by the substrate structure. From the electron micrograph point of view the substrate surface shows the collapsed tantalate layers, the preferred nucleation sites for the Pt deposition are less compared to that in the case of the orderly oriented niobate. The numbers of TPB regions established are less compared to that of the niobate due to the randomly orientated layers. Even though the rough surface provides more surface area, the thicker, non-spherical Pt particles cover most of the rough layered surfaces. The ionic conductivity of  $\text{HCa}_2\text{Ta}_3\text{O}_{10}$  of  $10^{-5} \text{ Scm}^{-1}$  is large enough to promote the reasonably fast transport process. The possible reasons for the delay in response which are, (i) the deformed layer structure may not stabilize the thermodynamic equilibrium interface between Pt particle and the perovskite oxide (ii) the exchange and ionization of hydrogen is not occurring according to thermodynamic equilibrium or is delayed, not establishing the redox equilibrium, (iii) the large Pt surface regions may suppress the fast

transportation of charged species. The presence of  $\text{OH}^-$  ions is evident from the vibrational spectrum. There is no further change in current observed above 4 % of  $\text{H}_2$  concentration, this may be due to the voltage drop across the electrolyte. According to the equilibrium potential distribution described in chapter (3), the chemical potential of  $\text{OH}^-$  at the cathode side is much higher than that at the anode side. At higher  $\text{H}_2$  concentration the electrochemical potential of  $\text{OH}^-$  may be decreased due to the large number of proton formation at the anode. Eventually the voltage drop occurring in the cell shows that there is no change in current upon increase in the  $\text{H}_2$  concentration above 4 %. Thus, hydroxide ion conducting electrolytes may not be useful as solid ionic conductors to detect higher concentrations. Highly selective, sensitive, more stable and reproducible hydrogen sensor are only possible with the predominantly proton conducting solid electrolytes.

### ***References to chapter 6***

- [1] K.J. Kim, M. Shahinpoor and A. Razani, Proceedings of SPIE-The International Society for Optical Engineering, 3987(Electroactive Polymer Actuators and Devices (EAPAD)), pp 311-320 (2000)
- [2] M. Shahinpoor and K.J. Kim, *Smart Mat. Struct.* **9**[4], 543-551 (2000)
- [3] P. He, M. Liu, J.L. Luo, A.R. Sanger and K.T. Chuang, *J. Electrochem. Soc.* **149**, A808-A814 (2002)
- [4] J. Fournier, G. Faubert, J.Y. Tilquin, R. Cote, D. Guay and J.P. Dodelet, *J. Electrochem. Soc.* **144**[1], 145-154 (1997)
- [5] R. Liu, W.H. Her and P.S. Fedkiw, *J. Electrochem. Soc.* **139**[1], 15-23 (1992)
- [6] T.A Zawodzinski, M. Neeman, L.O. Sillerud, and S. Gottesfeld, *J. Phys. Chem.* **95**[15], 6040-6044 (1991)
- [7] J. Halim, F.N. Buchi, O. Haas, M. Stamm and G.G. Scherer, *Electrochim. Acta* **39**, 1303 (1994)
- [8] J.T. Hinatsu, M. Mizuhata, and H. Takenaka, *J. Electrochem. Soc.* **141**, 1493-1498 (1994)
- [9] M. Calbi, T. Mercedes, C. Flavio and W. Milton, *J. Low Temp. Phys.* **126**[1/2], 179-186 (2002)
- [10] A.N. Frumkin, Hydrogen overvoltage and adsorption phenomena Part II. In Delahay P, Tobias CW (ed) *Advances in electrochemistry and electrochemical engineering*, vol 3. Wiley-Interscience, New York, pp 287-391 (1963)
- [11] S.J. Paddison, R. Paul and T.A. Zawodzinski, *J. Electrochem. Soc.* **147**, 617-626 (2000)



- [12] C.Z. Zheng, C.K. Yeung, M.M.T. Loy and X. Xiao, *Phys Rev B: Condens Matter* **70**, 205402-1 (2004)
- [13] N. Bonanos, *Solid State Ionics* **145**, 265–274 (2001)
- [14] V. Thangadurai and W. Weppner, *Ionics* **7**[1 & 2], 22-31 (2001)
- [15] V. Thangadurai and W. Weppner, *J. Mater. Chem.***11**, 636–639 (2001)



---

## Chapter 7

### **Practical application: Measurement of Hydrogen in Biomass fuel generator**

A diffusion type limiting current hydrogen sensor has been developed based on the solid polymer electrolyte. In the previous chapter, the potential materials and methods for the operation of H<sub>2</sub> sensor were discussed. Based on those parameters an attempt was carried out to test an H<sub>2</sub> sensor under biomass reactor conditions. In the following, the sequential approaches are described which were made to operate the sensor under the specific conditions and the device was engineered to best suit the practical applications.

#### *6.1 Bio mass fuel production*

Non-thermal production of pure hydrogen from the fermentation of thermophilic bacteria under the bioprocess is projected by “HYVOLUTION” [[www.biohydrogen.nl/hyvolution](http://www.biohydrogen.nl/hyvolution)]. In thermophilic fermentations, glucose converts to, on the average, 3 moles of hydrogen and 2 moles of acetate as the main by-product. Acetate is a prime substrate for photoheterotrophic bacteria. The possible gas evolutions in the biomass reactor are: Hydrogen (10-80%), Carbon dioxide (10-20%), Hydrogen sulphide (1-5%) and fractions of organic compounds. These composition ratios vary from the different biological source. The performances of the sensing cell were measured under saturated water vapour condition at 80 °C. The approaches were based on extending the detection limit of the sensor system presented in section 5.1.9 and to prevent the carbon dioxide poisonings.

#### *6.2 Sensing Element (SE)*

In all investigated devices identical sensing elements (*SE*) assemblies were employed i.e., the chemically reduced gas diffusion electrodes were sandwiched between protonated Nafion 117 membrane and the gas (the experimental details are described in section 4.1).

#### *6.3 Approach 1: Diffusion hole amperometric type*

The major practical importance of passing a current through a solid proton conductor based galvanic cells lies in the chance to control or influence the kinetics and therefore the galvanic cell reaction. An approach to shift the upper detection limit of hydrogen concentration to 80% was carried out by using a tiny diffusion hole. In

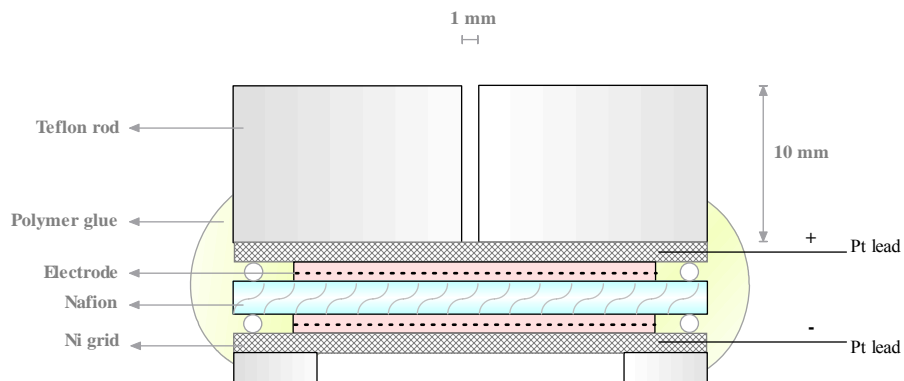


Figure 7.1: Structure of the cell construction C-1.

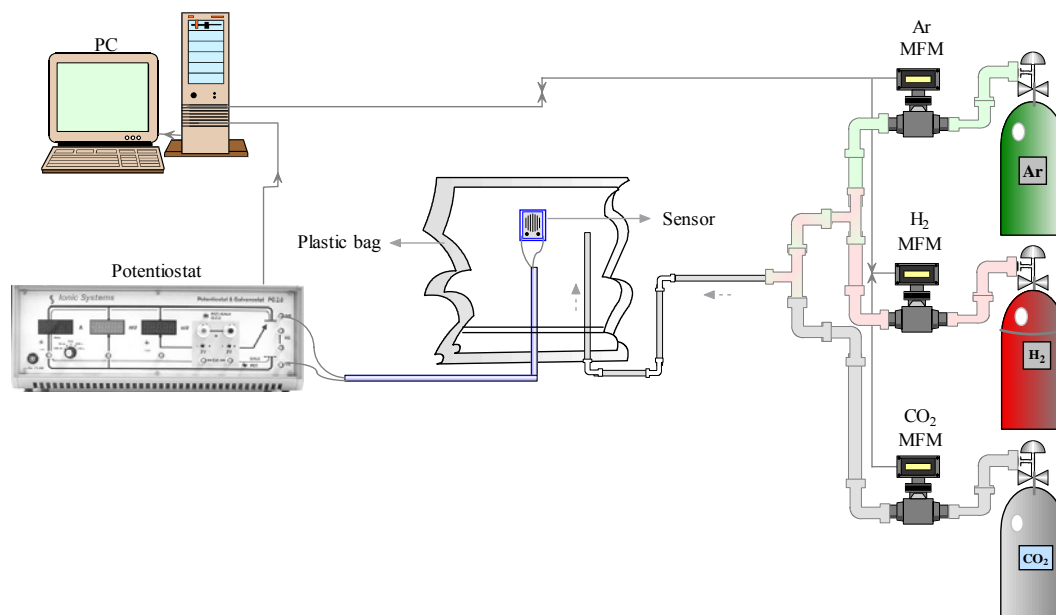


Figure 7.2: Pictorial representation of the experimental setup for investigations under H<sub>2</sub> atmospheres using plastic bag.

diffusion hole type amperometric sensors the proton conductor is encapsulated by a diffusion barrier pellet.

Application of a voltage to the electrolyte decreases the activity of the species in the gas between the diffusion barrier and the electrolyte. As soon as the partial pressure of hydrogen is negligibly small within this gap as compared to the outer side, the current will no longer increase with the applied voltage. A sheet of Teflon provided with a diffusion hole of 1 mm in diameter was mounted on SE (referred as cell construction C-1). A cross sectional view of the complete cell construction is shown in figure 7.1. The rate determining pinhole diameter was chosen by employing equation 2.1 and it was estimated that a limiting current of 43 mA occurs through, 10 mm long pinhole of 1 mm in diameter. The assembled sensor cell C-1 was covered with a polypropylene plastic bag provided with gas inlet and outlet and the measurements were carried out at room temperature as shown in figure 7.2.

The results obtained from the polarization measurement are shown in figure 7.3. The calibrated sensor limiting current was found to be 8.2  $\mu\text{A}$  at 400 mV potential. The current values obtained are very low at 100%  $\text{H}_2$  concentration and moreover, the observed current was not saturated over a period of running time of 2 hours. It was found that the polypropylene plastic bag permeates  $\text{H}_2$  and exchanges with the ambient gas (air).

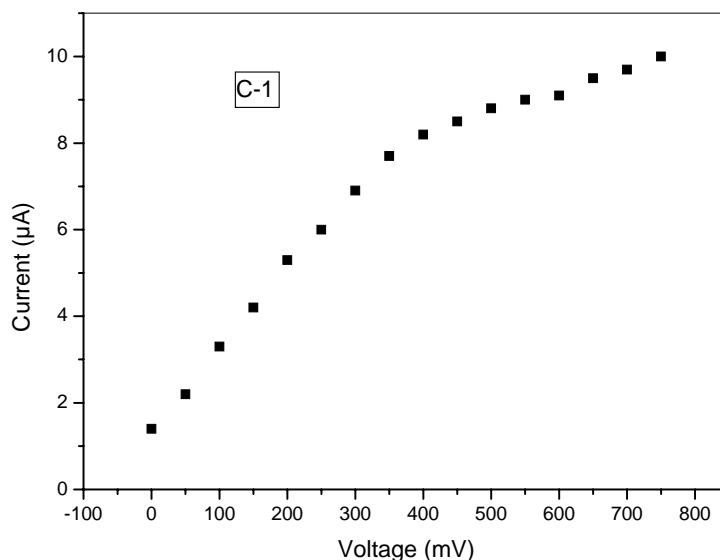


Figure 7.3: I-V characteristics of C-1.

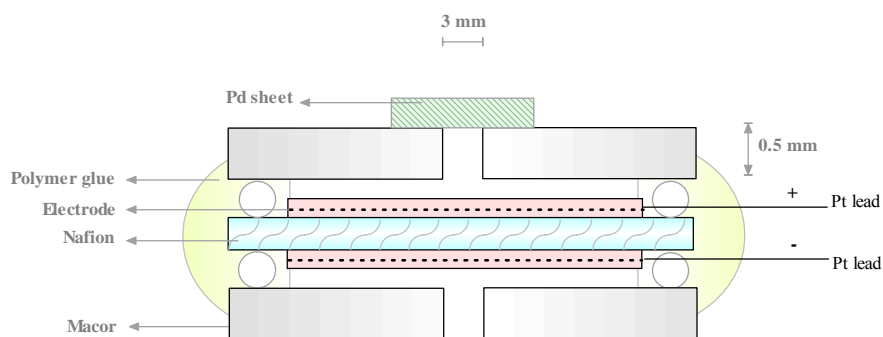


Figure 7.4: Structure of the cell construction C-2.

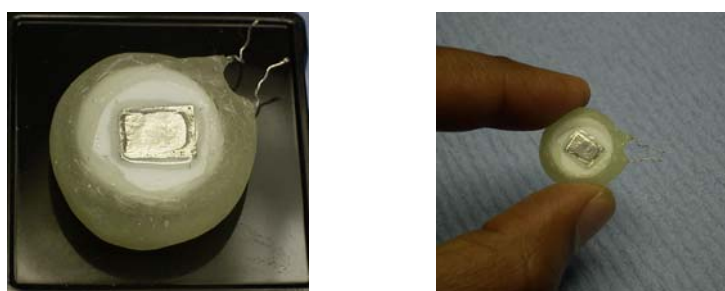


Figure 7.5: Photographs of C-2.

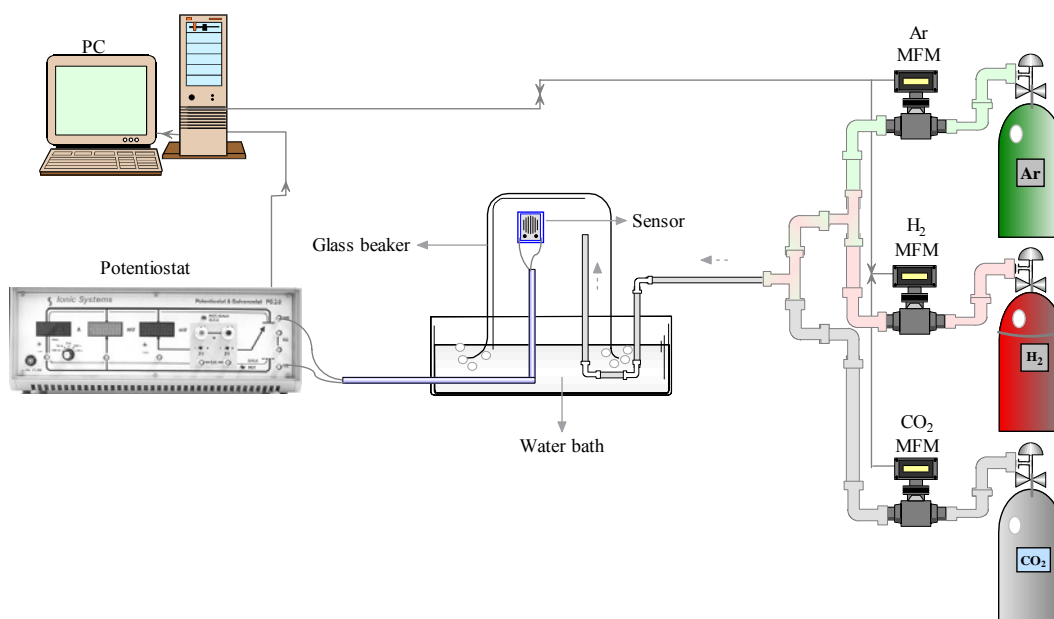


Figure 7.6: Pictorial representation of the experimental setup for investigations under  $H_2$  atmospheres using glass beaker.

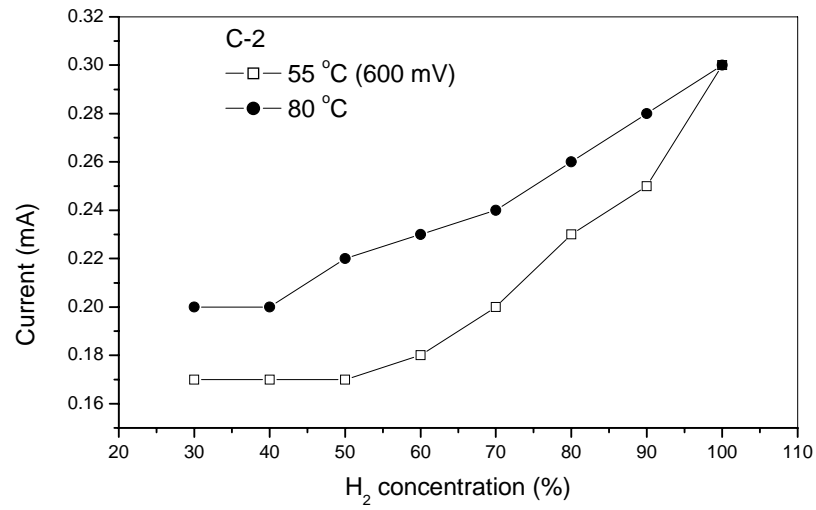


Figure 7.7: The effect of temperatures on sensing H<sub>2</sub> with sensor C-2.

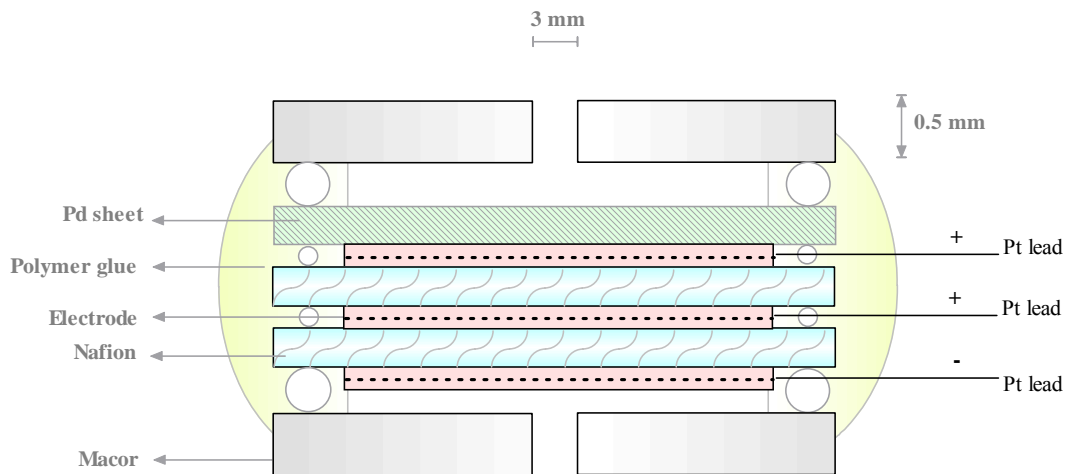


Figure 7.8: Structure of the cell construction C-3.

#### 6.4 Approach 2: Diffusion control by Pd sheet

With respect to selectivity, it is very useful to use a hydrogen permeable metallic membrane that limits the access of the gas to the proton conductor. A palladium sheet of 0.025 mm in thickness was used as diffusion barrier. In this cell construction C-2, the Teflon sheet was replaced by Macor<sup>®</sup> ceramic material of circular 1.5 cm dia pellet provided with a diffusion hole of 3 mm in diameter and 0.5 mm in length. A Pd sheet of 3x5 mm was placed in front of the diffusion hole and sealed on top of the ceramic pellet as shown in figure 7.4. The photographs of cell C-2 with Pd sheet shown in figure 7.5.

The plastic bag was replaced with a glass beaker to avoid H<sub>2</sub> permeation as shown in figure 7.6. In order to measure the temperature effect of the sensor, a glass container provided with a water bath and bubbling the gas through a frit and the outer surface was covered with a heating band. The effect of measuring temperature was

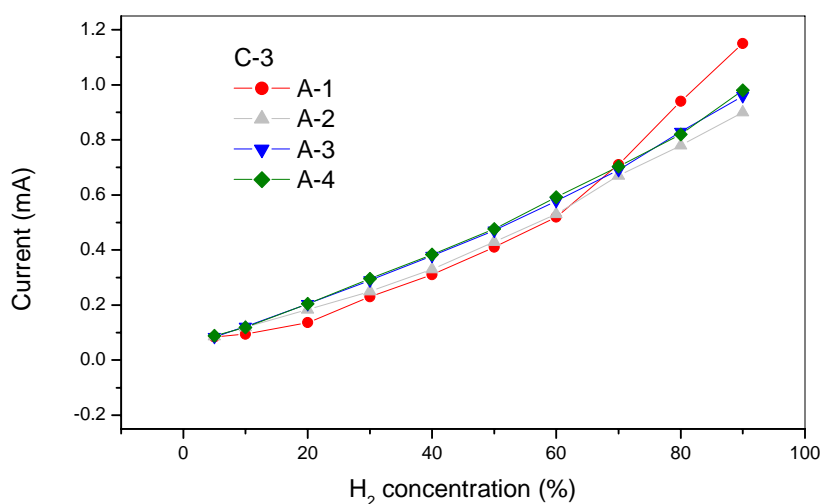


Figure 7.9: Reproducibility of the detected sensor current of C-3 with a wide range of H<sub>2</sub> concentrations.

studied at 55 and 80 °C with H<sub>2</sub> concentrations of 30-100% using cell C-2 shown in figure 7.7. The current values were high when the sensor was measured at high H<sub>2</sub> concentration, expecting an increase in protonic conduction with temperature and humidity. The observed current values were unstable due to the presence of air trap within the diffusion hole area while assembling the cell. The Pt sheet was placed directly on top of the electrode (referred as C-3). In order to prevent the electrode poisoning from direct contact with CO<sub>2</sub> gas, a sacrificial electrode arrangement was applied. The two sets of MEA were attached in series and sandwiched between the Pd sheet and Macor<sup>®</sup> layer as shown in figure 7.8.



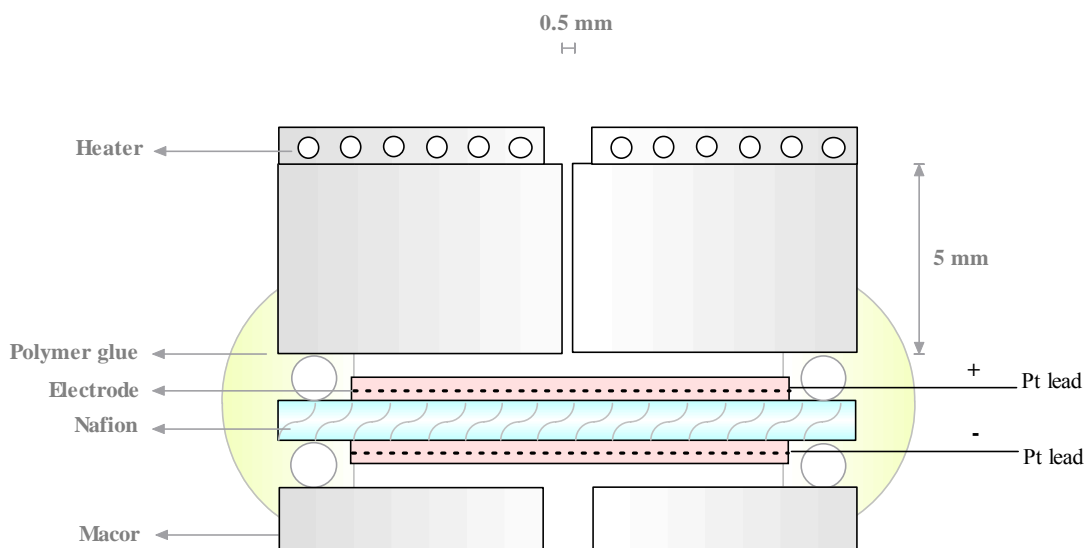


Figure 7.10: Structure of the cell construction C-4.



Figure 7.11: Photographs of top and side view of sensor C-4 with the heating element on top.

The sensor linear response behaviour of the C-3 device at four different times (named A-1 to A-4) is shown in figure 7.9. The linear current increases with  $H_2$  concentration for several cycles of sequential exposure of gas concentrations. After 24 h it was found that the cell starts to break apart, due to the pressure development in the sandwiched membrane compartment. Cell C-3 construction was not considered further.

### 6.5 Approach 3: Entrapment of cross sensitive gas

The cell construction (C-3) as described above section was modified by reducing the diffusion hole diameter to 0.5mm at a length of 5 mm and eliminating the Pd barrier sheet (referred as C-4) shown in figure 7.10. The photographs of cell C-4 with heating element show in figure 7.11. The  $H_2$  and  $CO_2$  gas mixtures were purged over

CO<sub>2</sub> traps, such as silica gel granules, barium hydroxide solution and liquid nitrogen cooling traps. The experimental arrangement with the trapping unit is shown in figure 7.12. The moisture absorption behaviour of silica granules was used to trap the large CO<sub>2</sub> molecules. It was observed that over a period of absorption (a few minutes) the surface of the gel turns to saturate with the gas species. Next, barium hydroxide solution column was used to precipitate into the barium carbonate, it was

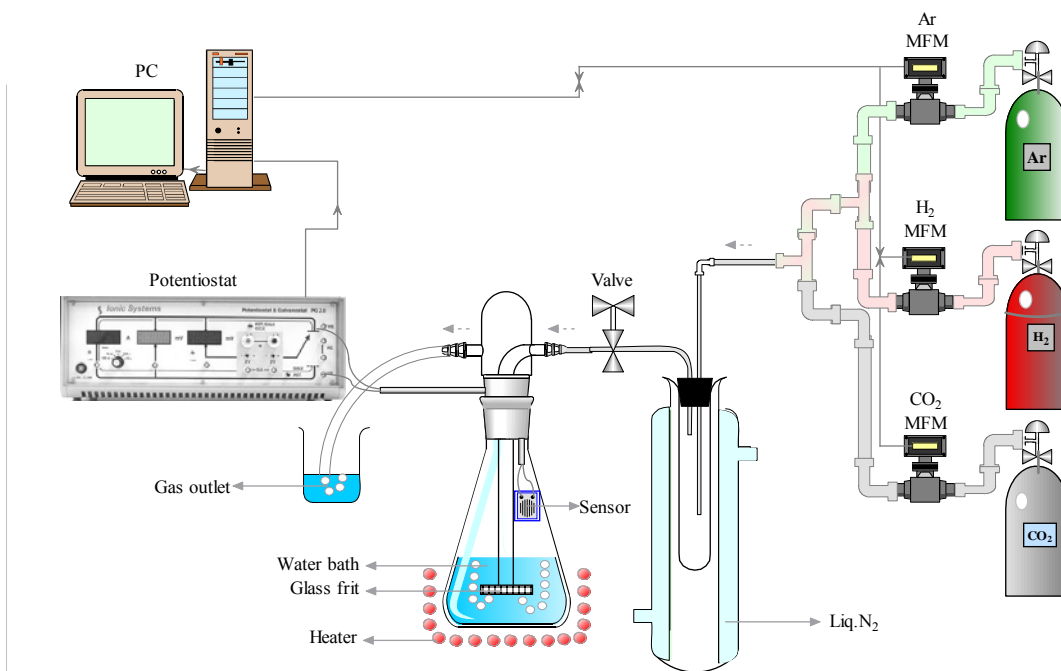


Figure 7.12: Pictorial representation of the experimental setup for investigations under H<sub>2</sub> atmospheres using LN<sub>2</sub> coolant.

found that the precipitation occurred at the beginning and the rate of precipitation was slower than the gas flow rate. Finally an attempt to freeze CO<sub>2</sub> molecules was carried out by using a liquid nitrogen (LN<sub>2</sub>) trap along the gas mixture line. Upon the introduction of LN<sub>2</sub> in to dewar, rapidly a low pressure was developed in the gas line. A “check valve” was installed to prevent the water back suction from the measuring chamber.

The cell was mounted in a closed glass container as shown in figure 7.12. The gas flow was passed through the LN<sub>2</sub> trap unit, the dewar was filled with liquid before the measurement. Due to its fast volatilisation, the liquid was added frequently.

The response behaviour of the C-4 sensor element with 5-25 % H<sub>2</sub> concentration was observed. The sequential step increase in H<sub>2</sub> concentration up to 10 % shows a nearly linear behaviour and the repeated cyclic performance is shown in figure 7.13. The response of C-4 cell was observed with 10% CO<sub>2</sub> in 40 % H<sub>2</sub> as shown in figure 7.14 and linear response of C-4 shown in figure 7.15. A reproducible response with 40 and 50 % H<sub>2</sub> concentration was observed in the presence of 10 % CO<sub>2</sub> as show in figure 7.16.

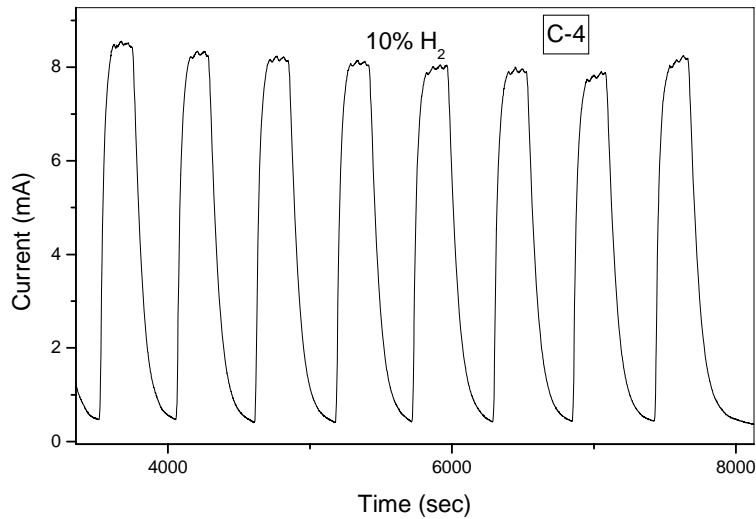


Figure 7.13: Continuous response curves in sensing 10 % H<sub>2</sub> using sensor C-4.

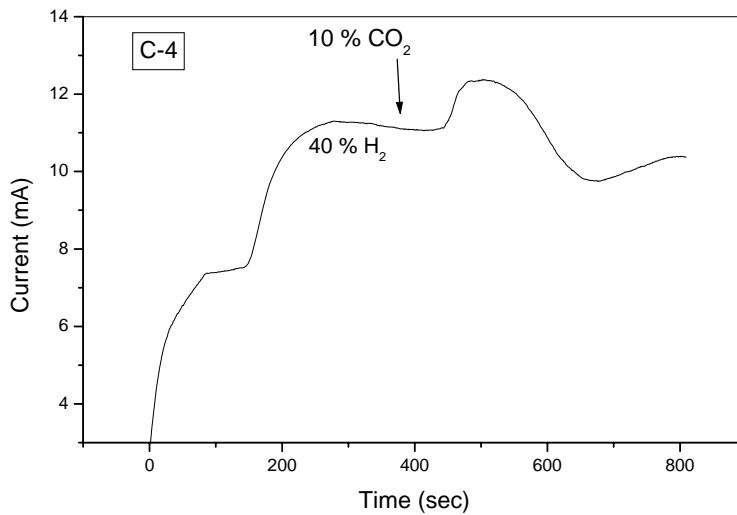


Figure 7.14: Hydrogen gas (40%) response behaviour of sensor C-4 with 10 % CO<sub>2</sub>.

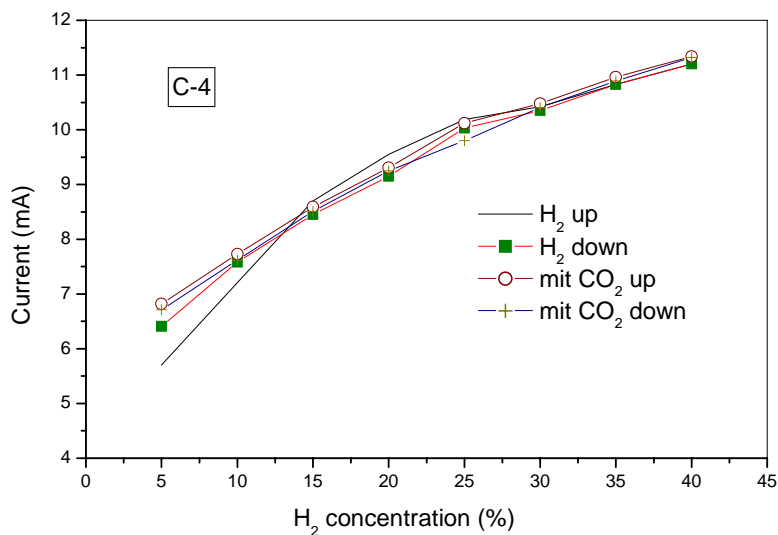


Figure 7.15: Detected steady state current of C-4 in 5-40 % H<sub>2</sub> concentration range with and without CO<sub>2</sub> in both upward and downward measurement.

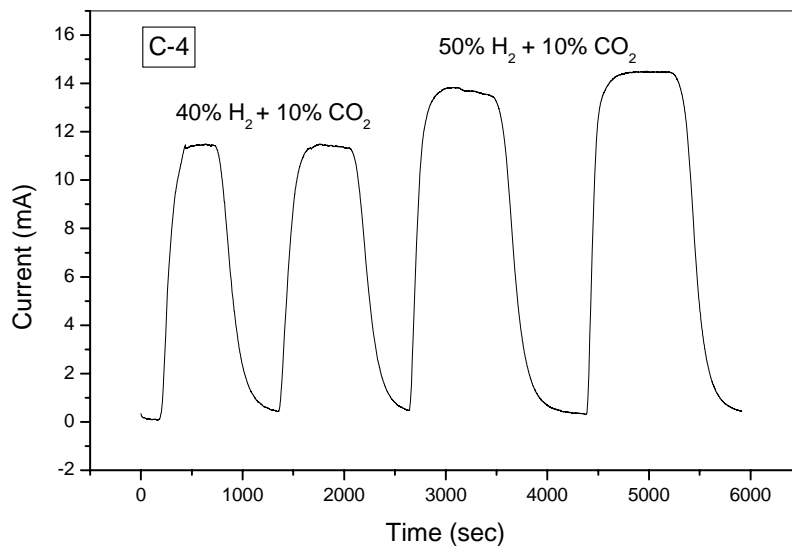


Figure 7.16: Reproducibility of sensor C-4 in the presence of CO<sub>2</sub>.

---

## Chapter 8

### Summary and outlook

The present work deals with the structural and, electrochemical investigations and possible practical application of polymer and ceramic proton conductor based sensors for hydrogen detection.

Gas sensing hydrogen electrodes were optimised by employing three different methods. Thick, inhomogeneous and non-uniformly sputtered films, rate limitation by mass transport, large binder resistance and low water retention capacity of gas diffusion electrode (GDE) electrodes were not suitable at ambient conditions. Among the other two methods chemically reduced Pt on Nafion membrane by the impregnation-reduction (I-R) method provided a good interfacial contact between the electrode and electrolyte. The chemically impregnated metal salt ions  $[\text{Pt}(\text{NH}_3)_4]^{2+}$  were completely reduced with two different types of reductants. In the narrow range of reductant concentration for 0.006 to 0.1 M  $[\text{MBH}_4]$  (M =Na, K), significant surface morphological changes were observed with optical and scanning electron microscopes. AFM studies have shown the same results as SEM i.e., a good adherence of Pt particles on Nafion, both chemically and mechanically. Nanometer sized particles in the range from 16 to 262 nm were observed both from XRD pattern and microscopic studies. The average diameter of particles was found to be increasing with increased reductant concentrations. Highly porous structured and fine particle sized surfaces with a large number of triple phase boundary (TPB) sites were obtained at 0.01M and 0.04 M concentrations of weak and strong reductant, respectively. A model of volume expansion on wet conditioned membrane electrode assembly (MEA) was proposed to explain the crack formation under the compressive and tensile stress.

Photoelectron studies have shown the pure metal state formation in chemically reduced Pt electrodes. When compared with GDE, the amount of Pt loading by the I-R method has a significant advantage to be controlled by the amount of reductant concentration. At low Pt loading of 0.065 mg, the higher electrocatalytic surface area of 0.096 cm<sup>2</sup> was optimised with less Pt loading by chemically reduced Pt at 0.01 M  $\text{Pt}(\text{NH}_3)_4\text{Cl}_2$  and 0.01 M  $\text{KBH}_4$  composition.

The ionic conductivity of the MEA was studied by the AC impedance method as a function of temperature and relative humidity. The MEA of chemically reduced electrodes

shows higher values than the other two methods. At ambient temperature, the highest conductivity of  $0.02 \text{ Scm}^{-1}$  was obtained. The conductivity has further increased to  $0.04 \text{ Scm}^{-1}$  with temperature up to  $65 \text{ }^\circ\text{C}$ .

The chemically reduced sensing electrode from  $\text{NaBH}_4$  reductant was found to be a suitable for sensors. The performance of the short circuit amperometric  $\text{H}_2$  sensor was investigated by employing the Pt | Nafion (0.01 M  $\text{Pt}(\text{NH}_3)_4\text{Cl}_2$  and 0.04 M  $\text{NaBH}_4$ ) element with carbon fibre cloth for different concentration steps of  $\text{H}_2$  in  $\text{N}_2$  at room temperature. A linear relationship between the current and the  $\text{H}_2$  concentration was observed for both forward and reverse direction of changes at the concentration of hydrogen gas from 1 to 10%. The average maximum sensitivity was observed to be  $0.01 \mu\text{A cm}^{-2}\text{ppm}^{-1}$ ,  $0.007 \mu\text{A cm}^{-2}\text{ppm}^{-1}$  and  $0.008 \mu\text{A cm}^{-2}\text{ppm}^{-1}$  in the hydrogen partial pressure range from 1-2, 3-7 and 8-10%, respectively. The response time ( $t_{90}$ ) to achieve a change of 90% was typically less than 5-15 s.

For leak detection purposes, the sensing electrode prepared by using  $\text{KBH}_4$  reductant was suitable for low ppm level  $\text{H}_2$  detection. At room temperature, the hydrogen sensing characteristics of the sensor element Pt | Nafion MEA (0.01 M  $\text{Pt}(\text{NH}_3)_4\text{Cl}_2$  and 0.01 M  $\text{KBH}_4$ ) was investigated in the 10 to 50 ppm  $\text{H}_2$  concentration range. Linear output current responses were observed for different samples over the given hydrogen concentration range. A average maximum sensitivity of the sensor  $0.0046 \mu\text{A cm}^{-2}\text{ppm}^{-1}$  was obtained. The response time ( $t_{90}$ ) was typically less than 10-30 s. For several cycles, identical maximum output currents were observed changing the hydrogen concentration within 1 min from 0 to 50 ppm. The same sets of MEA were performed in the 100–1000 ppm range. A maximum sensitivity of  $0.0026 \mu\text{A cm}^{-2}\text{ppm}^{-1}$  and response time of 5–25 s was obtained. All measurements were made at ambient temperature and relative humidity no specific less water maintenance.

A ceramic based sensor system was developed to detect  $\text{H}_2$  at high working temperature conditions. An extension of short circuit amperometric method operating over a wide range of concentration employing layered type perovskite oxides was made. A series of alkali rare earth Dion-Jacobson (D-J) phase layered perovskite compounds was synthesised by both solid state and soft chemical ion exchange reactions. Phase pure materials of layered perovskites were obtained with 20% excess of alkali carbonate. The electrocatalytic Pt particles were deposited with *in-situ* chemical reduction of  $[\text{Pt}(\text{NH}_3)_4]^{2+}$  ion by a modified I-R method. The possibility of electroless deposition on layered perovskite D-J phase materials was demonstrated.

A large number of distinct TPB sites and particle sizes of 50–500 nm were observed by the optical microscope. The reductant concentration of 1 M  $\text{KBH}_4$  was optimised to obtain  $1.85 \text{ mg cm}^{-2}$  Pt loading on a niobate sample. The presence of HOH and OH groups was found from the vibrational spectrum. The property of proton conduction in  $\text{KCa}_2\text{Nb}_3\text{O}_{10}$  was measured in  $\text{H}_2$  containing atmospheres. Proton conductivity of  $6.3 \times 10^{-5} \text{ Scm}^{-1}$  at  $45^\circ\text{C}$  was obtained with this compound. In general, niobate compounds show higher ionic conductivities than tantalates. The electrical conductivity of  $2.5 \times 10^{-6} \text{ Scm}^{-1}$  at  $45^\circ\text{C}$  was obtained with  $\text{HCa}_2\text{Ta}_3\text{O}_{10}$ . The sensing performance of proton conducting niobate  $\text{KCa}_2\text{Nb}_3\text{O}_{10}$  was proven from 50 ppm to 8 %  $\text{H}_2$  concentration at  $45^\circ\text{C}$ . The maximum sensitive current of  $9.32 \mu\text{A}$  was achieved within 5 s and recovery time was 12 s. The sensing currents were reproducible for more than 100 cycles of identical gas concentration. The tantalate  $\text{HCa}_2\text{Ta}_3\text{O}_{10}$  of higher electrical conductivity shows a maximum sensitive current of  $8 \mu\text{A}$  at 3%  $\text{H}_2$  with a response time of 15–25 s and recovery time of less than 30 s.

Interface models have been proposed for both polymer and ceramic based ionic conducting systems. The thermodynamic equilibrium potential distribution of the interface between  $\text{H}^+$  and  $\text{OH}^-$  ion conducting media and semi-spherical Pt particles are considered in terms of the chemical potential, electrostatic potential and electrochemical potential. The proton diffusion mechanism at the Pt particle was considered in two models, i.e., surface and bulk diffusion. The dissociated  $\text{H}_2$  molecule species transport along the surface was faster than the bulk diffusion process. The calculated response time ( $\tau_s = 5 \text{ ms}$ ) was consistent with the observed response.

For practical applications, the polymer based hydrogen sensor with various stages of modifications was demonstrated. The optimised cell construction was made with a 0.5 mm diameter diffusion hole at the anode side which was also connected with a heating element. The catalytic electrode poisoning of  $\text{CO}_2$  gas mixture along with  $\text{H}_2$  was eliminated with an  $\text{LN}_2$  trap unit. The  $\text{H}_2$  gas detection of up to 80 % was able to detect in  $\text{H}_2$  presence of 10-20 %  $\text{CO}_2$  gas. The successful measurement of  $\text{H}_2$  gas concentration promises a potential device for bio mass reaction application.

The successfully employed chemical reduction method on polymers as demonstrated for small area has to be extended to large surfaces. The evaluation of cross sensitivity to other gases of developed polymer based sensor needs to be further performed, especially for hydrogen concentrations. The thickness of the Pt loading layer should be reduced for cost reasons.

The particle size and morphology of Pt at the electrolyte interface has a noteworthy influence on the performance of the hydrogen gas sensor. Further optimization of the chemical reduction process on layered perovskite proton conductor should be performed to form a uniform, homogeneous and selective deposition by varying concentrations of the metal salt and reductants, time and temperature of impregnation-reduction. The proton conduction mechanism of D-J phases should undergo further investigations. Long term stability of the ceramic system is mandatory at various working temperatures. Since the solid oxides are considered to be easier in to handle the case of large scale productions, structurally and chemically stable solid oxide layered perovskite based hydrogen sensors should be further investigated for practical applications.



---

## Partial publications

### Publications in scientific journals

1. **M. Sakthivel**, and W. Weppner, Characterization and sensing property studies of the Pt | Nafion electrode prepared by the chemical reduction method. *Ionics* (2005), 11(3 & 4), 177-183.
2. **M. Sakthivel**, and W. Weppner, Chemical sensors and technologies for sustainable hydrogen economy, Recent Research Developments in Chemical Engineering (2005), 6 85-129- Invited.
3. **M. Sakthivel**, and W. Weppner, Development of a hydrogen sensor based on solid polymer electrolyte membranes. *Sensors and Actuators, B: Chemical* (2006), B113(2), 998-1004.
4. **M. Sakthivel**, and W. Weppner, Response behavior of a hydrogen sensor based on ionic conducting polymer-metal interfaces prepared by the chemical reduction method. *Sensors* (2006), 6(4), 284-297.
5. **M. Sakthivel**, and W. Weppner, Electrode kinetics of amperometric hydrogen sensors for low ppm level hydrogen detection, *J Solid State Electrochem.* (In press) 2006.
6. **M. Sakthivel**, and W. Weppner, Application of layered perovskite type proton conducting  $\text{KCa}_2\text{Nb}_3\text{O}_{10}$  in  $\text{H}_2$  sensors: Pt particle size and temperature dependence, *Sensors and Actuators, B: Chemical* (Submitted).
7. **M. Sakthivel**, and W. Weppner, Microstructural studies on chemically deposited electrode on D-J phase niobate and tantalate compounds, (In preparation).
8. **M. Sakthivel**, and W. Weppner, A novel solid-state  $\text{H}_2$  sensor for biomass fuel generator, (Manuscript).
9. **M. Sakthivel**, and W. Weppner, Hydrogen sensing based on proton and electron transport across and along polymer electrolyte / platinum electrode interfaces, *J. Phys. D: Appl. Phys.*, (Manuscript).

### Oral presentations

1. **M. Sakthivel** and W. Weppner, A solid state hydrogen sensor based on polymer electrolyte membranes, Euro Conference on Solid-State Ionics- Transport properties, University of Patras, Greece, 14-18th September 2004.
2. **M. Sakthivel** and W. Weppner, Ionic conducting polymer-metal interfaces in hydrogen detection. 3rd International Symposium on Sensor Science (IS 2005), Juelich, Germany, July 18-21. 2005.

### Poster presentations

1. **M. Sakthivel** and W. Weppner, Ionic conducting polymer-metal nano particle interfaces for gas sensor applications, 2nd International Workshop on Polymer/Metal Nanocomposites, GKSS Research Centre, Geesthacht, Germany, September 26-27, 2005).
2. **M. Sakthivel** and W. Weppner, A novel amperometric sensor and portable device for detection of hydrogen at the ppm level, International Conference on Electrochemical Sensors, Mátrafüred, Hungary. November 13–18, 2005. (Best Poster Award)
3. **M. Sakthivel** and W. Weppner, Layered perovskite oxide for H<sub>2</sub> sensing, The 11th International Meeting on Chemical Sensors (IMSC11), University of Brescia – Italy, 16th-19th July 2006.

### Participation in conference

1. Hemdsärmelkolloquium, Institut für Anorganische Chemie der Christian-Albrechts- Universität zu Kiel, 16-18 March 2006.

---

## Curriculum vitae

Name	Mariappan Sakthivel
Place of residence	Bremer straÙe 23, Kiel, Germany
Born	3 <sup>rd</sup> June 1975 in Erode
Nationality	Indian
Parents	S. Mariappan and M. Sundarakannu
1992-1995	B.Sc. (Physics) at the Erode Arts College, Bharathiar University, Coimbatore, India
1995-1997	M.Sc. (Materials Sciences) at the P.S.G. College of Technology, Bharathiar University, Coimbatore, India
1997-1998	Software Programmer at the Infogenesis Solutions, Erode, India
1998-2000	M.Tech. (Materials Engineering) at the National Institute of Technology Karnataka, Mangalore University, Surathkal, India
2000-2001	Scientific research assistance at the SPIC Science Foundation, Chennai, India
Nov 2001 - 2006	Scientific collaborator at the Technical Faculty of the Christian Albrechts-Universität zu Kiel, Germany (Chair of Prof. Dr. W. Weppner)





